Durham E-Theses

Electroluminescence in epitaxial thin film zns and znse

Jones, A. P. C.

How to cite:

Jones, A. P. C. (1987) *Electroluminescence in epitaxial thin film zns and znse*, Durham theses, Durham University. Available at Durham E-Theses Online: http://etheses.dur.ac.uk/6783/

Use policy

The full-text may be used and/or reproduced, and given to third parties in any format or medium, without prior permission or charge, for personal research or study, educational, or not-for-profit purposes provided that:

- a full bibliographic reference is made to the original source
- a link is made to the metadata record in Durham E-Theses
- the full-text is not changed in any way

The full-text must not be sold in any format or medium without the formal permission of the copyright holders.

Please consult the full Durham E-Theses policy for further details.

Academic Support Office, Durham University, University Office, Old Elvet, Durham DH1 3HP
e-mail: e-theses.admin@dur.ac.uk Tel: +44 0191 334 6107
http://etheses.dur.ac.uk

ELECTROLUMINESCENCE IN EPITAXIAL
THIN FILM ZnS AND ZnSe

by

A. P. C. Jones, B.Sc.

The copyright of this thesis rests with the author.
No quotation from it should be published without
his prior written consent and information derived
from it should be acknowledged.

A Thesis Submitted for the
Degree of Doctor of Philosophy
in the University of Durham

July 1987

17 FEB 1988

ABSTRACT

The application of the metalorganic chemical vapour deposition technique to the production of II–VI compound semiconductor electroluminescent devices is discussed. Both low field MIS minority carrier injection devices and high field impact excitation structures are considered, and comparisons are drawn with more commercially orientated electroluminescent displays.

The epitaxial growth of ZnS and ZnSe onto (100) orientated GaAs substrates, using the reactions between dimethyl zinc and the hydrides H_2S and H_2Se, is described. Details are given of a novel epitaxial MIS device processing technology, in which a ZnS I–layer also acts as an etch–stop, thus enabling chemical removal of the GaAs substrate. Metal electrodes deposited directly onto the ZnS and ZnSe allow the electrical and electroluminescent characteristics of these epitaxial II–VI compound layers to be investigated in the absence of any influence from the substrate material. X–ray diffraction and reflection high energy electron diffraction confirm that the structures are epitaxial and of excellent crystallinity. It is demonstrated in an electron beam induced current study that conduction in the epitaxial MIS devices is highly uniform, and this is manifested in a uniform spatial distribution of electroluminescence.

A description is given of high field impact excitation electroluminescent devices, in which the ZnS layer is doped with manganese during MOCVD growth. The spatial distribution of EL in these devices is shown to be non–uniform, and thus indicative of filamentary conduction in the ZnS:Mn, in accordance with a recently proposed dielectric breakdown model of instability. It is demonstrated that the transient characteristics of the epitaxial structures correlate with those of commercial polycrystalline devices, and are also consistent with the predictions of a dynamic model of instability. As a result of filamentary conduction, both epitaxial and polycrystalline devices are prone to degradation through localised dielectric breakdown. These breakdown events generally result in a gradual erosion of the active electrode area, although, under certain operating conditions, mobile filaments can cause rapid destruction of epitaxial structures. The columnar microstructure of sputtered devices appears to prevent such filament mobility, and it is concluded that, although filamentary conduction is a result of the carrier injection mechanism and is independent of the crystallinity, the associated damage is strongly influenced by the microstructure of the device.

DECLARATION

I declare that the work reported in this thesis, unless otherwise stated, was carried out by the candidate, that it has not previously been submitted for any degree and that it is not currently being submitted for any other degree.

A. P. C. Jones
Candidate

ACKNOWLEDGEMENTS

I wish to take this opportunity to thank the many people who have helped in the production of this thesis. I am grateful to my supervisors Prof. J. Woods and Dr. A.W. Brinkman for their assistance and guidance, and to Dr. G. Russell for his enthusiastic help and encouragement. I would like to thank Dr. R.E. Jones for the use of his computer model of DCEL. I am also indebted to the technical staff of the department, whose expertise made much of the experimental work possible.

I am grateful to my industrial supervisors Dr. B. Cockayne and Dr. P.J. Wright of the Royal Signals and Radar Establishment for useful discussions and the provision of MOCVD growth facilities. I have also benefitted from discussions with Dr. J. Kirton at RSRE. The provision of an SERC CASE award in collaboration with RSRE is gratefully acknowledged.

On a more personal note I wish to express my gratitude to my father for his support and encouragement throughout my university career. Finally, special thanks go to my wife Carole for her support and kindness during our time in Durham.

CONTENTS

1 INTRODUCTION 1

2 ELECTROLUMINESCENCE IN II–VI COMPOUNDS 3

2.1 Crystallographic and electronic band structure 3

2.2 Luminescent properties of II–VI compounds 4
2.2.1 Excitation 4
2.2.2 Exciton luminescence 4
2.2.3 Donor–acceptor pair emission 5
2.2.4 Deep centre luminescence 7
2.2.5 Inner shell transitions 9
2.2.6 Phonon assisted optical transitions 10
2.2.7 Non–radiative transitions 10

2.3 Electrical properties and minority carrier injection 11
2.3.1 Electrical properties of ZnS and ZnSe 11
2.3.2 The Schottky barrier 13
2.3.3 The metal insulator semiconductor diode 14
2.3.4 The p–n junction 15

2.4 Hot electron impact electroluminescence 15
2.4.1 Hot electron generation and impact excitation 16
2.4.2 Electroluminescent panel displays 17

3 ELECTROLUMINESCENCE IN BULK ZnSe 19

3.1 Introduction 19

3.2 Device fabrication 21
3.2.1 Source purification and crystal growth 21
3.2.2 Impurity extraction and doping 21
3.2.3 Electrical contacts 22

3.3 Optical measurements 22

3.3.1 Direct current electroluminescence 22

3.3.2 Time–resolved electroluminescence 23

3.4 Electrical characterisation 24

3.4.1 Photoelectric response 24

3.4.2 Capacitance–voltage characteristics 25

3.4.3 Current–voltage characteristics 26

3.5 Summary 27

4 MOCVD GROWTH AND CHARACTERISATION OF EPITAXIAL ZnS/ZnSe STRUCTURES 29

4.1 Introduction 29

4.2 MOCVD growth 31

4.2.1 Growth apparatus

4.2.2 Source and substrate materials 31

4.2.3 Growth of structures for device applications 32

4.3 Structural assessment 32

4.3.1 X–ray diffraction 32

4.3.2 Surface morphology 33

4.3.3 RHEED investigations 34

4.3.4 Cross sectional TEM studies 34

4.4 Electrical assessment 36

5 EPITAXIAL THIN FILM ZnS/ZnSe INJECTION DEVICES 37

5.1 Introduction 37

5.2 Metal–semiconductor devices 37

5.3 Fabrication of metal–insulator–semiconductor devices 38
5.3.1 Epitaxial MIS devices 38
5.3.2 MIS structures incorporating III–V compound buffer layers 39
5.3.3 Thin film MIS devices with polycrystalline I-layers 40
5.3.4 Structural assessment 41
5.3.5 Surface chemical analysis 42

5.4 Electrical characterisation 43
5.4.1 Current–voltage characteristics 43
5.4.2 Capacitance–voltage characteristics 44
5.4.3 Electron beam induced current 44

5.5 Optical characterisation 46
5.5.1 Transmittance 46
5.5.2 Electroluminescent spectrum 46
5.5.3 Spatial distribution of electroluminescence 47

5.6 Summary 47

6 DC ELECTROLUMINESCENCE IN EPITAXIAL THIN FILM ZnS:Mn/ZnSe STRUCTURES 49

6.1 Introduction 49

6.2 Device fabrication 50
6.2.1 Current DCTFEL device geometries 50
6.2.2 MOCVD growth and epitaxial DCTFEL device fabrication 51

6.3 Device characterisation 52
6.3.1 The dielectric breakdown theory of DCEL 52
6.3.2 Experimental current–voltage characteristics 54
6.3.3 Electroluminescent spectrum 55
6.3.4 Spatial distribution of electroluminescence 55

6.4 Time dependent behaviour of DCEL devices 56
6.4.1 The time dependent model of DCEL 57
6.4.2 Experimental electrical and luminescent transient behaviour 58

6.5 Device maintenance 61

6.5.1 Operational device lifetime 62

6.5.2 Localised destructive breakdown 62

6.5.3 Current filament mobility 63

6.6 Summary 64

7 SUMMARY AND CONCLUSIONS 65

REFERENCES 68

CHAPTER ONE

INTRODUCTION

Visible light emitting devices are of current importance in a variety of display and signalling applications, forming an essential link in the interface between electronic instruments and human users. The fundamental process relevant to many of these devices is electroluminescence, which may be defined as the non-thermal generation of light resulting from the application of an electric field to a material. The effect was first observed in 1907 using a point contact on SiC[1], but it was not until the basic principles of carrier injection were established in the 1950s that the light emission could be attributed to minority carrier injection and recombination. Today the most efficient light emitting diodes (LED) available are based on the III–V compounds and their ternary alloys, where high efficiencies can be achieved as a result of the very efficient injection of minority carriers in forward biased p–n junctions. Operation in the visible region of the spectrum is possible using ternary compounds such as $GaAs_{1-x}P_x$ near the direct–indirect energy gap cross over composition of the alloy. Yellow and green light emission have been achieved in commercial devices, but only in indirect energy gap compounds such as GaP, which are inherently inefficient phosphors.

An obvious step in the path towards efficient light emitting devices capable of operating over the entire visible spectrum, is the production of p–n junctions in the direct wide gap II–VI compounds. Early research work on the optical properties of crystalline solids indicated that these compounds were likely to be very efficient phosphors, and should therefore provide the most suitable materials for near band gap electroluminescence. Initial progress was encouraging and some control over electrical properties was achieved through doping with appropriate electrically active impurities, in an analogous manner to that used for electronic devices based on the semiconductors Ge and Si. However, it was found that the wide band gap semiconductors presented great difficulties in materials preparation, and by the 1960s it appeared that the amphoteric doping required for the production of p–n homojunctions was not possible with the available technology.

Despite the commercial success of the III–V devices, the extremely high luminescence efficiency of the wide direct gap II–VI compounds over the entire visible spectrum continued to provide a strong incentive for the development of alternative II–VI device structures. Low field minority carrier injection luminescence was obtained in II–VI compounds using both heterojunction and Schottky barrier devices, but without any real breakthrough towards an efficient LED emitting in the blue. II–VI compounds were also employed in an alternative type of device which did not require minority carrier

[1] H. J. Round, Elect. Wld. **19** 309 (1907).

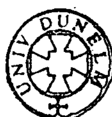

injection. Such electroluminescence was first observed by Destriau[2] in a cathodoluminescent ZnS phosphor, which was held as a dispersion in oil between the parallel plates of a capacitor. Green electroluminescence was observed during excitation with a high alternating voltage. The effect has been attributed to impact excitation of luminescence centres in the ZnS host lattice by charge carriers accelerated in the high electric fields. The oil filled capacitor has since been refined to a solid state device, and several variants are commercially available for display applications.

The comparatively recent application of low temperature growth techniques, such as molecular beam epitaxy and metalorganic chemical vapour deposition (MOCVD) to the II–VI compounds, has provided a new stimulus for research. These techniques circumvent the problems of melt growth at high temperatures, and allow greater control over the impurity and defect concentrations. Although the feasibility of using MOCVD for the growth of II–VI compounds was first demonstrated in 1968[3] no further work in this field was reported until 1978, and the use of MOCVD material for device applications has only recently attracted interest.

In this thesis the application of MOCVD grown ZnS and ZnSe to both low field minority carrier injection and high field hot electron impact devices is discussed. Following this brief introduction, the theoretical basis of the investigation is considered in chapter 2. Bulk grown single crystal devices, which provided a base for further study, are discussed in chapter 3. The MOCVD growth of ZnS and ZnSe is described in chapter 4, and the application of this material to devices is discussed in chapter 5, where details of the device processing technology developed in order to more fully exploit the MOCVD material are given. Low field minority carrier injection luminescence and high field impact luminescence devices based on this technology are described in chapters 5 and 6 respectively. Chapter 7 concludes the thesis with a summary and discussion of the present work, and some suggestions for further research.

[2] G. Destriau, J. Chim. Phys. 33 587 (1936).

[3] H. M. Manasevit and W. I. Simpson, J. Electrochem. Soc. 118 644 (1968).

CHAPTER TWO

ELECTROLUMINESCENCE IN II–VI COMPOUNDS

2.1 Crystallographic and electronic band structure

The fundamental electrical and optical properties of the II–VI compounds are due to their tetrahedral bonding and valency. All the binary II–VI compound semiconductors are composed of equimolar proportions of a group VIb element (Zn,Cd,Hg) and a group IIb element (O,S,Se,Te), and (with the exception of CdO) can crystallise in either the zincblende (fcc) or wurtzite (hexagonal) structure. The following discussion will be restricted to the zincblende material which was used in the present study.

The zincblende structure is composed of two interpenetrating face–centred cubic lattices which are displaced by $\frac{1}{4}$ of the cube diagonal in the unit cell, as shown in figure 2.1. Figure 2.2 shows the Brillouin zone for the reciprocal lattice, which is taken to be a truncated octahedron. The detailed band structures of ZnS and ZnSe, which are shown in figure 2.3, were first derived using empirical local pseudopotential calculations [1]. More recently, a non–local pseudopotential calculation has been made, taking into account spin–orbit coupling [2]. As with the other II–VI compounds, the minimum energy difference between the conduction and valence bands occurs at $k = 0$ in the energy–momentum relationship, that is, the materials have a direct band gap. Some of the important electronic properties of the II–VI compounds are summarised in figure 2.4. As with other compound semiconductor families, the band gaps of the II–VI compounds increase with decreasing atomic number.

An important consequence of the direct band gap is that crystal momentum conservation requirements do not inhibit efficient band to band radiative recombination. The range of band gaps available implies that, in principle, electroluminescence (EL) could be obtained over the entire visible spectrum, extending into the ultraviolet. Furthermore, it is possible to tailor the band gap to a specific requirement by using ternary compounds such as $Zn_xCd_{1-x}S$. Most of the II–VI ternaries exhibit a monotonic variation in band gap with composition, the exceptions being CdS_xTe_{1-x} and ZnS_xTe_{1-x} which have a band gap minimum at intermediate compositions. In general, the band gap of the ternary has a quadratic dependence on composition, which is fitted by an empirically determined bowing parameter:

$$E_g^{ABC}(x) = xE_g^{AC} + (1-x)E_g^{BC} - x(1-x)b \qquad (2.1)$$

where E_g^{AC} and E_g^{BC} are the energy gaps of compounds AC and BC respectively, E_g^{ABC} is the energy gap of the ternary, x defines the composition of compound $A_xB_{1-x}C$, and b is the bowing parameter.

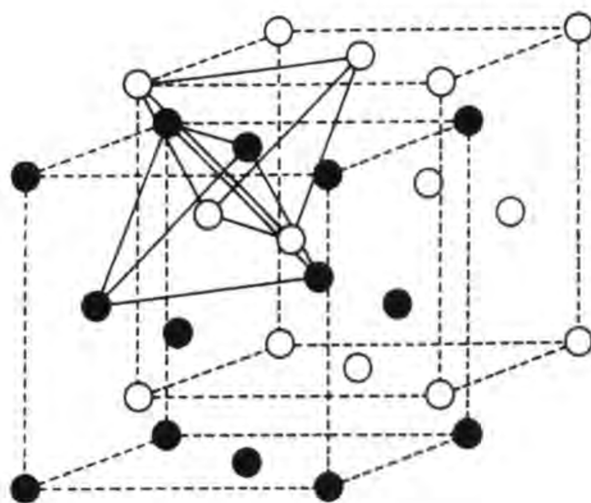

Figure 2.1 The zincblende structure.

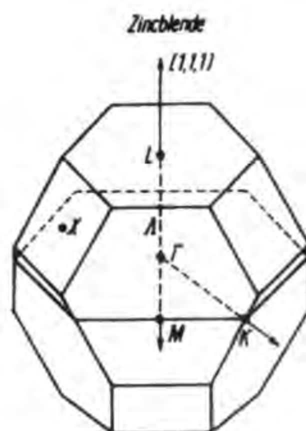

Figure 2.2 Brillouin zone of the zincblende lattice.

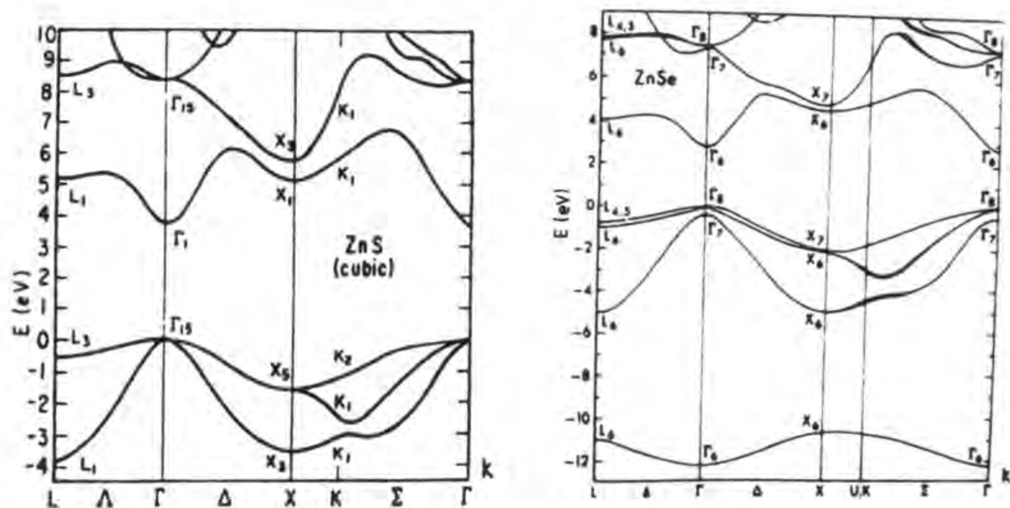

Figure 2.3 Band structure of ZnS and ZnSe (ref. 1,2).

By varying the composition of the II–VI ternary compounds, the lattice constant can be adjusted to any value between that of either of the constituent compounds. This is of practical application in epitaxial growth, where it is possible to grow ternary layers which are lattice matched to heteroepitaxial substrates. For example, by adjusting the composition of the ternary ZnS_xSe_{1-x}, lattice–matched material may be grown on GaAs, GaP, Si and Ge [3].

2.2 Luminescent properties of II–VI compounds

The II–VI compounds first assumed commercial importance in their application as phosphors for cathode ray tubes. Indeed, they were the first semiconducting materials to be used on a large scale, and even today their production volume is comparable with that of silicon [4]. The first applications of II–VI phosphors exploited the direct band gaps and various recombination processes, although the mechanisms were not understood at the time. In this section the physical basis of luminescence is introduced. For further information the reader is referred to the many review articles available, see for example [4,5].

2.2.1 Excitation

When a pure semiconductor is excited by radiation with energy greater than the band gap, or by minority carrier injection, free electrons and holes are created in the conduction and valence bands. Interband recombination can occur if a conduction electron recombines with a valence hole, producing a photon of energy E_g. However, direct band to band recombination of electrons and holes is unlikely due to the ionic nature of the II–VI compounds, and most of the holes are captured by defect centres. The hole capture mechanisms are illustrated in figure 2.5, and include:

(a) binding to electrons to form an exciton,

(b) capture by charged defect levels,

(c) binding to an isoelectronic defect, forming a positively charged defect.

2.2.2 Exciton luminescence

An exciton consists of a free electron bound to a free hole by mutual coulombic attraction, where the electron and hole orbit a common centre of mass in a hydrogen like orbital. A free exciton is able to move through the host lattice until it decays radiatively (lifetime $\approx 10^{-9}$s) or becomes trapped at an impurity or defect site. The ionisation (binding) energy E_x^{free} for the free exciton is given by the Rydberg formula in an analogous manner to that for free electron states in the hydrogen atom model:

Important optical parameters of II–VI compounds (W, wurtzite; ZB, zincblende).

	Fundamental gap E_g (eV)		dE_g/dT 10^{-4} eV K^{-1}	Effective mass		Dielectric constant		Refractive index* 1.4 μm		Refractive index* 10.6 μm		Absorption coefficient (cm^{-1}) 10.6 μm
	4 K	300 K		m_n^*	m_p^*	ε_0	ε_∞	n_0	n_e	n_0	n_e	
	3.91 W		8.5 W	0.28	1.4 ∥	8.6	5.2	2.285,	2.288	2.33		
ZnS	3.84 ZB	3.66 ZB	4.6 ZB	(0.27–0.28)	0.49 ⊥	(8.1–8.6)	(5.13–5.2)	2.28 ZB				
			6.0									
				0.24	0.59 ∥	8.65	4.0	1.984	2.001			
ZnO	3.44 W	3.2 W	9.5 W		0.59 ⊥							
				(0.24–0.26)		(8.12–8.65)	(3.7–4.0)					
			8		0.75	9.2	5.8	2.31		2.392		0.005
ZnSe	2.83 ZB	2.67 ZB	4	0.17				2.43				
			7.2		(0.6–0.75)	(8.1–9.2)	(5.8–6.2)					
ZnTe	2.39 ZB	2.25 ZB	5.0	0.11	0.6	9.3	6.9	2.74		2.7		0.008
			5.5		(0.6–0.7)	(9.2–10.1)	(6.9–8.3)					
CdS	2.58 W	2.42 W	5.2	0.2	5.0 ∥	8.6	5.26	2.304	2.321	2.226	2.239	0.01
					0.7 ⊥							
				(0.17–0.205)	(0.7–0.8)	(8.6–9.3)	(5.2–5.26)					
CdSe	1.84 W	1.73 W	4.6	0.13	2.5 ∥	9.4	6.2	2.500	2.38	2.430	2.448	0.001
					0.45 ⊥							
				0.12–0.15)		(9.4–10)	(6.1–7.02)					
CdTe	1.6 ZB	1.58	2.3	0.11	0.35	10.9	7.2	2.75		2.64		0.002
			5.0									
		1.44	5.6	(0.096–0.11)		(10.2–10.9)	(7.1–7.21)					

* $n_0 - E \perp c$, $n_e - E \parallel c$

Figure 2.4 Electronic properties of II–VI compounds (ref. 4 p. 41).

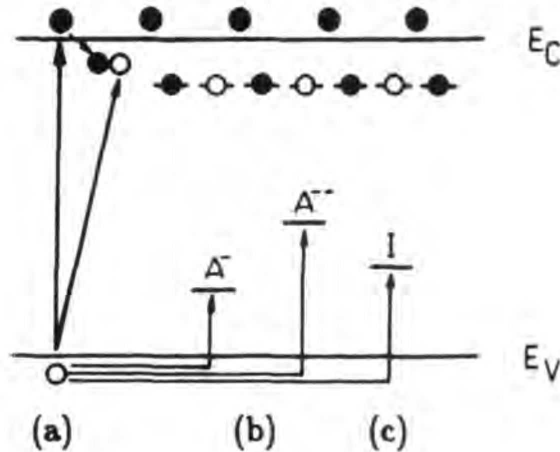

Figure 2.5 Capture of minority carriers by (a) electrons, (b) acceptors, (c) isoelectronic centres.

$$E_x^{free} = \frac{-m_r^* e^4}{2h^2\epsilon^2}\frac{1}{N^2} \qquad N = 1, 2, \ldots \tag{2.2}$$

where e is the electronic charge, h the Planck constant, ϵ the dielectric constant and:

$$\frac{1}{m_r^*} = \frac{1}{m_e^*} + \frac{1}{m_h^*} \tag{2.3}$$

m_r^* is the so-called reduced effective mass of the exciton, where m_e^* and m_h^* are the effective electron and hole masses respectively. The exciton energy E_x is measured relative to the conduction band edge. When the free exciton recombines, a photon is emitted with energy:

$$h\nu = E_g - E_x^{free} \tag{2.4}$$

Bound exciton complexes are formed when excitons bind to either ionised or neutral donors or acceptors. Bound exciton emission was first observed in CdS [6], and the nature of the defect was identified by studying the Zeeman effect (magnetic field splitting) in the exciton emission lines [7]. When a bound exciton recombines, a photon is emitted with energy:

$$h\nu = E_g - E_x^{free} - E_{BX} \tag{2.5}$$

where E_{BX} is the binding energy of the exciton to the defect. The highest experimentally observed value for the binding of excitons to shallow donors or acceptors in the II–VI compounds is approximately 20 meV [4]. Thus the bound exciton emission is stongly dependent on temperature, and at room temperature bound excitons tend to leave their centres before an optical transition can occur.

2.2.3 Donor–acceptor pair emission

ZnS and ZnSe are inherently n-type semiconductors (section 2.3.1), but due to compensation effects will contain a high concentration of acceptor type centres. Free electrons and holes may be captured by the donors and acceptors, and at low temperatures (which inhibit thermal ionisation) the only significant relaxation process is electron–hole recombination. For sufficiently distant pairs, the transition energy for a donor acceptor pair (DAP) separated by distance r is well represented by [8,9]:

$$E(r) = E_g - (E_D + E_A) + \frac{e^2}{\epsilon_0 r} \tag{2.6}$$

where E_D and E_A are the energy depths of the isolated donor and acceptor respectively, and ϵ_0 is the static dielectric constant.

The probability of the transition occuring is given by:

$$W(r) = W_0 exp\left(\frac{-2r}{r_B}\right) \tag{2.7}$$

where W_0 is a constant, and r_B is the Bohr radius of the shallower state.

Individual DAP transitions were first recorded and identified in GaP [10], where complicated arrays of emission lines could be accounted for in detail as transitions between randomly distributed donor and acceptor defects. Observation of DAP lines in the direct gap II–VI compounds required very much higher levels of excitation in order to saturate transitions between distant pairs. Figure 2.6 shows the pair line structure from ZnSe under intense excitation by an argon–ion laser [11]. Assignment of the emission bands to specific pairs was made on the assumption that the relative intensities of the lines were proportional to the statistical probability of a particular pair recombining, assuming a random distribution of impurities. The intensity pattern was calculated for the zincblende lattice with the type–I configuration, in which donor or acceptor occupy the same type of lattice site. A similar calculation for the type–II configuration, in which donor and acceptor are on opposite types of lattice sites, was inconsistent with the experimental observations.

In experimental studies the individual DAP lines are often not resolved, however two features of the bands allow them to be identified as DAP emission. These are the shifts in wavelength of the emission peak as a function of (I) excitation intensity and (II) luminescent decay time, which are observed in accordance with equations 2.6 and 2.7. If the intensity of excitation is increased under steady state conditions, the high energy tail of the unresolved DAP emission broadens due to saturation of transitions at relatively remote pairs, and the emission band appears to shift to shorter wavelengths [11]. Under dynamic conditions, where the emission spectrum is recorded at fixed time intervals after an excitation pulse, an unresolved DAP emission band appears to shift to longer wavelengths at greater delay times after excitation. This is because near neighbours recombine most rapidly (equation 2.7), and the more distant pairs recombine with the emission of lower energy radiation (equation 2.6). A study of the kinetics of radiative recombinations at randomly distributed donors and acceptors has enabled theoretical derivation of DAP decay spectra which are in excellent agreement with experimental observations in GaP [12]. More recently, similar effects have been studied in ZnSe [13].

Time resolved spectral measurements also allow two different series of bands in the edge emission (close to the absorption edge) of II–VI compounds to be identified. These are the high energy series (HES) which dominates the spectrum at higher temperatures, and the low energy series (LES) observed preferentially at liquid helium temperature. The LES emissions exhibit a shift in peak wavelength with both excitation intensity and decay time. Neither effect is observed in the HES series, and this observation can

be accounted for by the free to bound recombination of an electron in the conduction band with a hole trapped at an acceptor [14], in accordance with the model originally proposed for edge emission [15] shown in figure 2.7. The HES transitions are observed in most of the II–VI compounds since the binding energy of the acceptor is greater than that of the donor, and the donor centre ionises before the acceptor as the temperature is increased. Finally, it should be noted that within the HES and LES, further sub-divisions arise due to the energy levels associated with different impurities. Figure 2.8 shows energy levels for Li and Na doped ZnSe where, in addition to the three LES transitions P_0, Q_0 and R_0, further emission bands will arise from the free to bound transitions associated with these acceptors. The bound to bound transition can be observed at high temperatures under sufficiently high intensity excitation, which allows occupancy of the shallow donor and acceptor states. Thus DAP electroluminescence may be obtained in the band edge region at room temperature [16,17].

2.2.4 Deep centre luminescence

When the wide gap II–VI compounds are doped with group Ib acceptor impurities (activators) and group VIIb or IIIb donor impurities (coactivators), deep centres are created in the band gap. These can give rise to various types of broad band luminescence, associated with electronic transitions from the conduction band to an acceptor, or a donor to the valence band, as well as the DAP recombination discussed previously. The transition models illustrated in figure 2.9, are known as the (a) Schön–Klasens, (b) Lambe–Klick and (c) Prener–Williams models respectively. The nature of the centres and associated luminescence transitions have been the subject of extensive investigation using time resolved luminescence [18], and polarisation studies [19] in which preferential luminescence in certain crystal axes is related to anisotropy in the formation of DAP associations (due to anisotropy in the dielectric constant). More recently, optically detected magnetic resonance studies [20] have allowed direct correlation of emission bands with specific defect centres.

Some examples of the most well known deep centre luminescence bands are:

(1) Copper green luminescence in ZnS

Copper green luminescence is observed in ZnS doped with copper and a shallow donor such as aluminium. The luminescence exhibits a shift in the emission spectrum with both excitation intensity and decay time [18]. Figure 2.10 shows the time resolved emission spectrum of ZnS:Cu,Al under pulsed excitation with a UV flash light. The spectrum gradually shifts in the lower energy direction since the decay rate is greater at higher photon energies, and this indicates that the decay process is due to direct radiative recombination at DAPs with large separations, rather than the thermal release of trapped carriers. The decay rate is well represented by the power law $I \propto t^{-n}$,

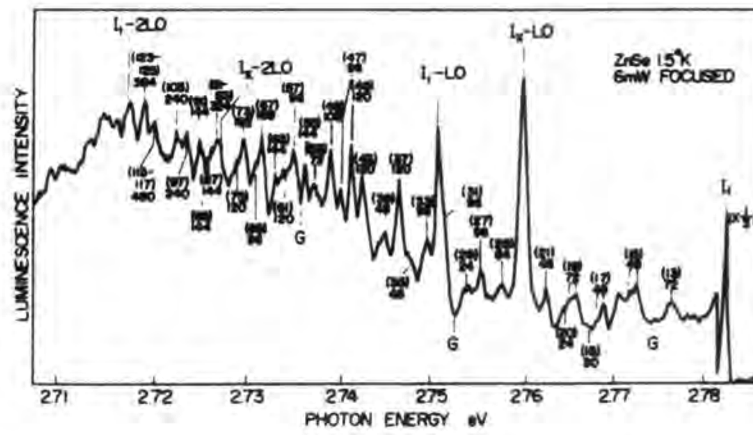

Figure 2.6 Pair line structure in the edge emission of ZnSe (ref. 11).

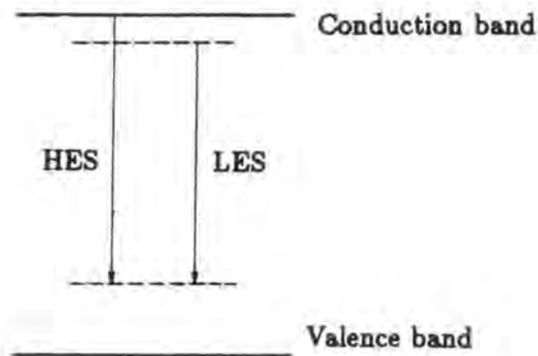

Figure 2.7 Energy level scheme for the HES and LES.

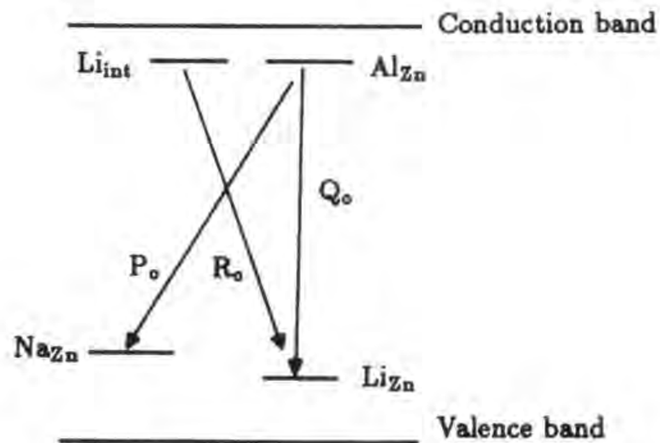

Figure 2.8 Donor acceptor pair transitions associated with Li and Na doping.

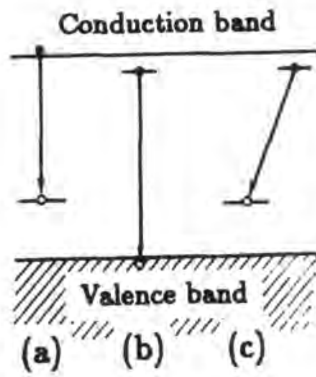

Figure 2.9 Energy models for luminescent emission in II–VI compounds.

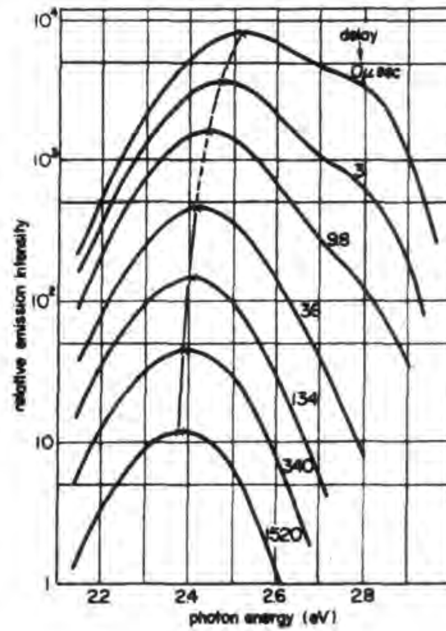

Figure 2.10 Time resolved emission spectra for the Cu–green emission in ZnS (ref. 18).

derived theoretically on the basis of equation 2.7, where n was predicted to be smaller for the low energy side of the peak [12]. Thus copper green luminescence in ZnS is well represented by the DAP model.

(2) Self activated luminescence

The self activated (SA) luminescence band is observed in II–VI materials doped with donor type impurities (coactivators), which then exhibit broad band luminescence in the absence of intentionally added acceptor states (activators). Conventionally the SA emission is attributed to DAP transitions involving shallow donors and A-centres (acceptors) consisting of a zinc vacancy in association with either a chlorine (donor) ion on a nearest sulphur site, or an aluminium (donor) ion on a nearest zinc site [21] (but see section 2.3.1). Thus the SA luminescence band shows a wavelength shift with luminescence decay time (figure 2.11a) and excitation intensity (figure 2.11b) as expected for DAP emission [18]. This conclusion was also confirmed by polarisation measurements for ZnS:Al [22].

(3) Copper green luminescence in ZnSe

The presence of copper in ZnSe results in a strong green luminescence [23]. However, although this was investigated by many authors, the chemical nature of the centre responsible for the emission has only recently been identified by optically detected magnetic resonance (ODMR) studies. In ODMR, changes in the spin distribution of the emitting centre are produced by absorption of microwaves in a magnetic field. Since recombination is subject to spin selection rules, the intensity of luminescence emission increases at fields corresponding to microwave induced resonance transitions [20]. Figure 2.12 shows the emission spectrum and ODMR signal for donor and acceptor centres in ZnSe. The donor resonance follows the same spectral dependence as the emission intensity, showing that donor electrons are associated with both emission bands. However, the copper resonance is only associated with the green emission band at 530 nm, and thus it can be concluded that the copper green emission in ZnSe is due to DAP recombination [24].

The deep centre transitions allow efficient luminescence in the II–VI compounds at room temperature, since $E_A \gg kT$ and the acceptor is not ionised. However, the use of deep centres for visible luminescence is limited to wide band gap semiconductors, because the energy of the emitted photons is significantly lower than the band gap energy.

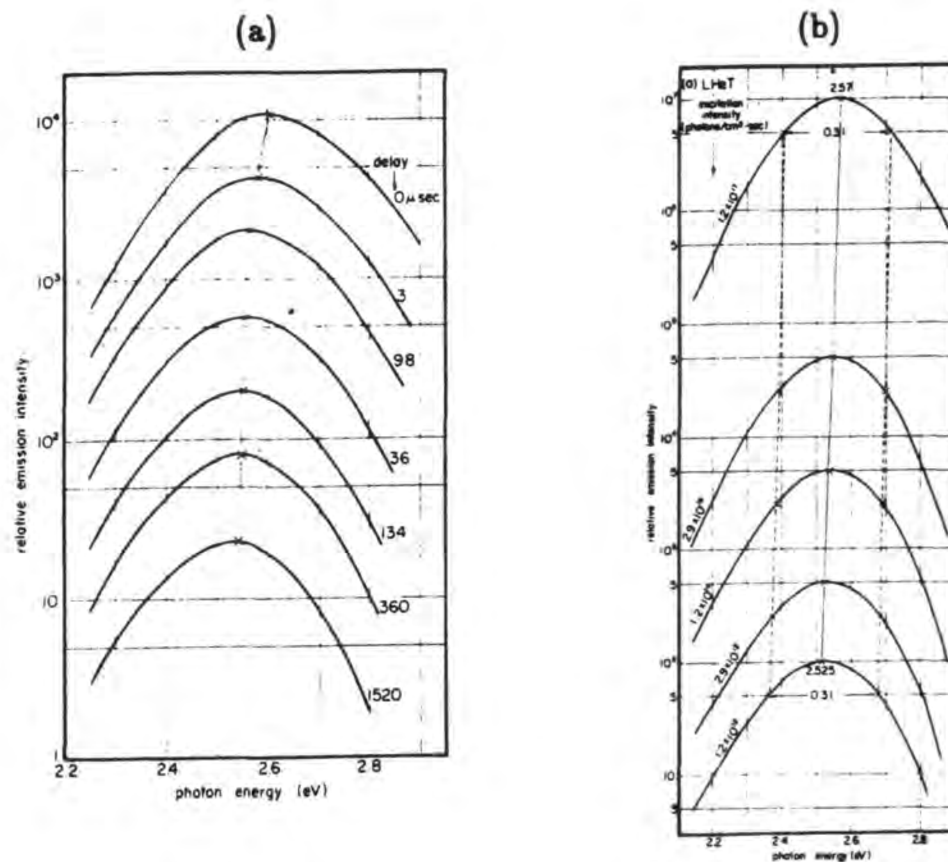

Figure 2.11 Self activated luminescence in ZnS:Cl (a) time resolved emission spectra, (b) emission spectra under various excitation intensities (ref. 18).

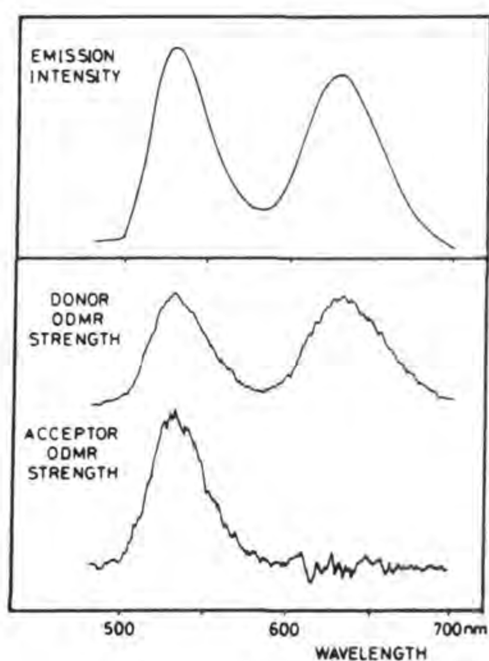

Figure 2.12 Luminescence emission and ODMR signal from a ZnSe:Cu crystal (ref. 24).

2.2.5 Inner shell transitions

The luminescence transitions described so far require electron hole recombination at a suitable defect centre. However, some luminescent centres are able to undergo internal radiative transitions without direct electron–hole recombination. The transition metals and the rare earth elements have this property due to unfilled $3d$, $4f$ and $5d$ orbitals in the former, and unfilled $4f$ orbitals in the second case. The transition element manganese gives rise to luminescence in many wide gap materials, but here interest will be focussed on emission due to Mn in ZnS and ZnSe. Electron paramagnetic resonance studies have shown that Mn substitutes on the metal site as Mn^{2+} in the ZnS and ZnSe lattices [25]. Free Mn atoms have the electron configuration [26]:

$$1s^2 2s^2 2p^6 3s^2 3p^6 (3d^5) 4s^2$$

where the $3d$ shell has started to fill after the $4s$ shell. In ZnS, the Mn $4s$ electrons take part in bonding in the same way as those in zinc, but instead of the inert $3d^{10}$ configuration of zinc there is a half filled $3d^5$ orbital. The crystalline field of the host lattice splits the free ion level associated with this unfilled shell to give a complex energy level scheme. Absorption and emission measurements suggest that at high Mn concentrations (1%) Mn–Mn pairs are formed, which further split the energy levels of the Mn^{2+} single ions [27,28,29]. Figure 2.13 shows the energy levels of the Mn^{2+} single ion and Mn–Mn ions in pair centres. It is not yet agreed where the ground level of this scheme should lie relative to the valence band edge of the host material [26]. Optical transitions between these d states are forbidden in the isolated divalent Mn^{2+} ion, however the host lattice crystal field, and exchange with neighbouring ions, gives the d–orbitals some p–like characteristics for which optical transitions are allowed. The transition ${}^4T_1 \rightarrow {}^6A_1$ gives rise to yellow luminescence in ZnS (photon energy 2.12 eV at room temperature), and the same transition occurs in both the cubic and hexagonal phases of ZnS, and in different host lattices such as ZnSe and ZnS_xSe_{1-x} [30]. This is because the transitions involve well shielded inner orbitals. The radiative lifetime of the transition is approximately 2 ms for dilute Mn concentrations in ZnS [28], the long lifetime being due to the forbidden nature of the d–d shell transition. The lifetime is reduced at higher Mn concentrations since the Mn–Mn pair transition has a smaller decay time than that of single ions.

Several luminescence excitation processes involving manganese centres are possible [26]:

(1) energy transfer to the manganese ion from a remote recombination event,

(2) electron hole recombination at the manganese centre,

(3) direct impact ionisation.

The Mn ion has no appreciable cross section for minority carrier capture, and the forbidden nature of the *d–d* transition implies that it is only weakly optically excitable, so the first two excitation processes are relatively unlikely. Fortunately however, the probability of impact excitation by hot electrons in the II–VI compounds is high, and this results in a high electroluminescence efficiency for Mn doped ZnS and ZnSe. The practical realisation of hot electron electroluminescence will be discussed in section 2.4.

2.2.6 Phonon assisted optical transitions

During the early investigations of band edge luminescence, it was noted that emission bands appeared as sets of lines with separations corresponding to the energy of longitudinal optical mode lattice vibrations in ZnS, CdS and ZnO [31]. The zincblende structure has two atoms per unit cell, and there are six branches in its vibrational spectrum [31]. The branches of the phonon spectrum are divided into transverse or longitudinal modes depending on whether the polarisation is transverse to, or along the wave vector. There are further subdivisions depending on whether the two atoms of the cell vibrate in phase (low frequency) or out of phase (high frequency) with each other, the two modes being termed acoustical and optical vibrations respectively [32]. Due to longitudinal optical (LO) phonon coupling, a single electronic transition is accompanied by a series of discrete replica lines equally spaced by the phonon energy $\hbar\omega_{LO}$. Acoustic phonon interaction with the electronic transition and each LO–phonon replica gives rise to acoustic phonon satellites, resulting in a Gaussian shaped band for each line [19]. The influence of phonon interactions on the electronic emission bands is shown in figure 2.14. Similar effects occur for other electronic transitions (excitonic, DAP) and in general the energy $h\nu$ of the emitted photons is given by:

$$h\nu = h\nu^{electronic} - n(\hbar\omega_{LO}) \qquad n = 1, 2, 3 \ldots \tag{2.8}$$

2.2.7 Non–radiative transitions

Non–radiative recombination is an undesirable process in electroluminescent devices, however there are several mechanisms through which excited carriers can lose their energy without photon emission, and these operate in direct competition to the radiative processes. One of the main competitors is Auger recombination, in which a second electron absorbs the energy given up by the first. There is an Auger mechanism corresponding to each of the radiative single electron processes, as shown in figure 2.15 [33]. The energy transferred to the second electron is dissipated as heat as it returns to the band bottom. Another non–radiative energy loss process is multi phonon emission. Figure 2.16 shows the configuration coordinate diagram for an electron in both the ground state (lower curve) and in the excited state (upper curve). If thermal excitation increases the energy of the electron to the point where the curves cross at r_c, then it

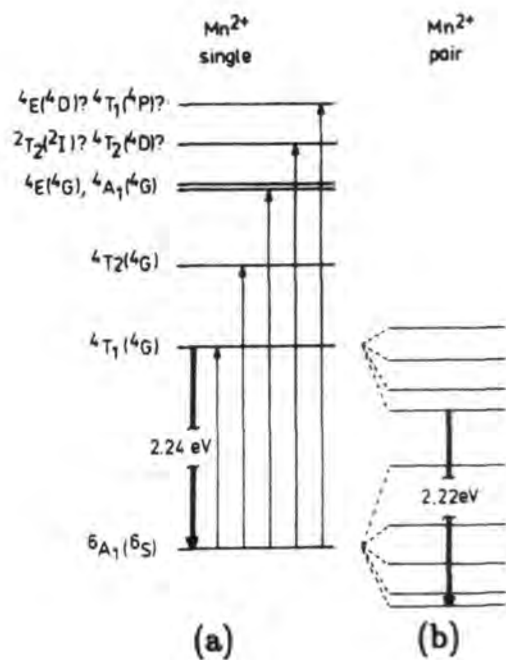

Figure 2.13 Energy levels of (a) Mn^{2+} single ions and (b) Mn^{2+} pairs (ref. 4 p. 114).

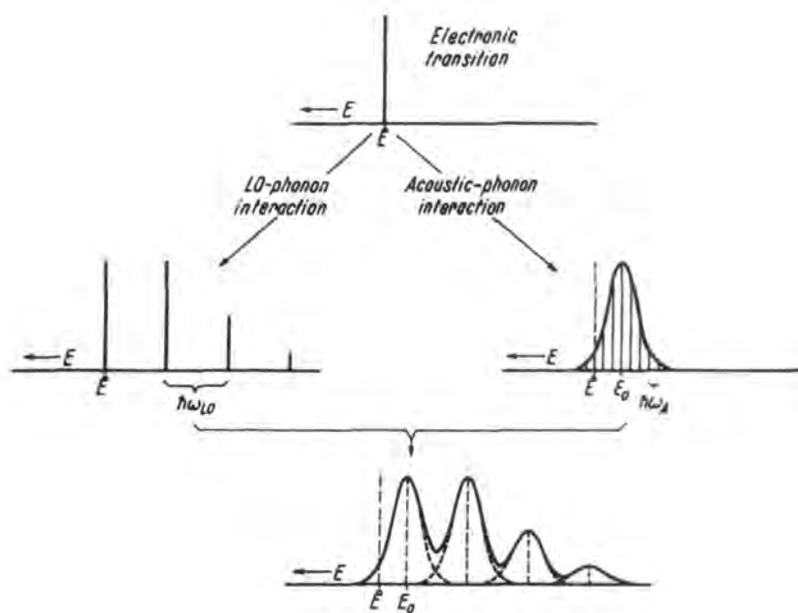

Figure 2.14 Influence of electron–phonon interaction on luminescence emission energy and band shape (ref. 19).

can return (non radiatively) to the energy minimum in the ground state at r_0, and energy is dissipated by the generation of phonons in the crystal lattice. Multi-phonon emission becomes more likely at higher temperatures since the electron must overcome the energy barrier E_a [34]. In addition to the true non-radiative processes, certain transition metals exhibit a "killer" action on visible luminescence by down conversion to the infra red region of the spectrum. The mechanism is analogous to that described for the Mn^{2+} ion in section 2.2.5. Finally, it should be noted that many of the desirable radiative transitions become less efficient at relatively high temperatures (room temperature) due to ionisation of the radiative centres before recombination can occur.

The various recombination mechanisms which have been discussed in this section are summarised in figure 2.17. We now go on to consider electrical excitation of the luminescence by minority carrier injection and hot electron impact.

2.3 Electrical properties and minority carrier injection

2.3.1 Electrical properties of ZnS and ZnSe

The potential of the II–VI compounds in EL device applications has not been realised due to the difficulty of amphoteric doping. Of the wide band gap II–VI compounds only ZnTe ($E_g \sim 2.3$ eV) can be made p–type, while the rest can be made n–type only. This difficulty is associated with [35]:

(1) compensation effects,
(2) low uncompensated solubility of dopants,
(3) high ionisation energies of the donor and acceptor states.

As a result, ZnS and ZnSe have only been available in n–type form, and it has proved impossible to create the reliable p–n homojunctions required for minority carrier injection. At an early stage of the research into the electrical properties of n–type ZnSe, it was reported that the resistivity could be reduced from $\sim 10^{10}$ to $\sim 1\ \Omega$ cm by annealing at $\sim 900\ ^\circ$C in molten zinc [36,37]. Radioactive tracer techniques revealed that the reduction in resistivity was due to the extraction of deep acceptor impurities from the ZnSe, and this conclusion was confirmed by detailed studies of the electrical properties of ZnSe doped with different shallow donors [38]. The effect of acceptor states on the resistivity was analysed statistically [39], and these calculations showed that a small fraction of deep levels was sufficient to reduce the net carrier concentration by several orders of magnitude. The problem of compensation is not only important in the production of lower resistivity n–type material, but is also central to the production of p–type ZnSe and ZnS.

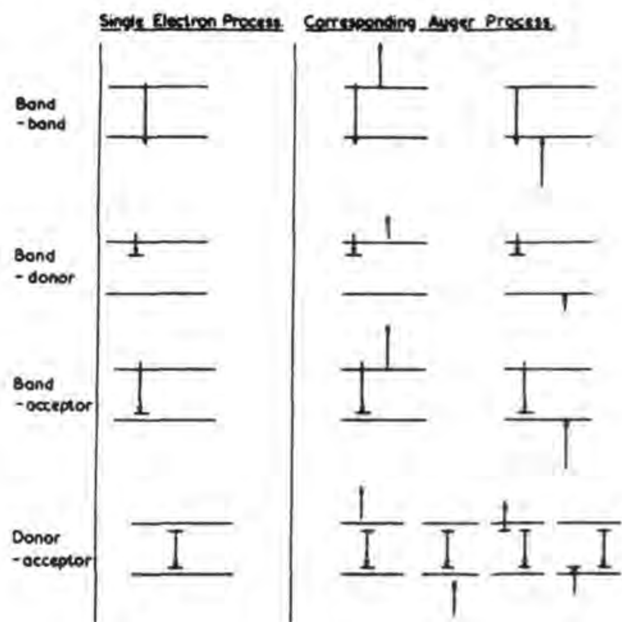

Figure 2.15 Correspondence between single electron and Auger processes (ref. 32,33).

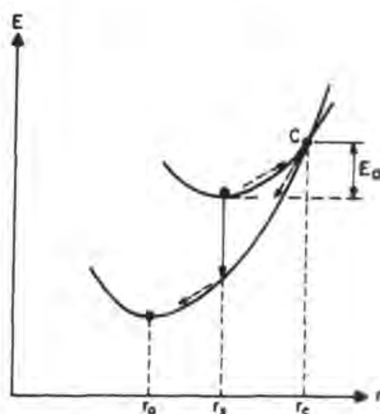

Figure 2.16 Configuration diagram showing radiative transition (solid arrow) and non-radiative transition via point c (ref. 34).

Emission mechanisms in II–VI compounds (emission energies given in first column).

No phonon emission at $h\nu$	Recombination mechanism at low temperature		Room temperature emission			
			Assumptions		Efficiency	
E_g	(band–band)				Negligible	
$E_g - E_X$	Free exciton		$E_X \approx kT$		Low	
$E_g - E_X - E_{BX}$	Excitons bound to	Donors (neutral, ionized)	$E_{BX} \ll kT$		Negligible	
		Acceptors (neutral)				
		Isoelectronic defects	$E_{BX} \gg kT$		High	
$E_g - (E_d + E_a) + \frac{e^2}{\varepsilon R}$	Donor–acceptor pair emission of	Shallow donor + shallow acceptor	$E_a \gg E_d (\approx kT)$		Low	
			d–a emission	Free electron–bound hole emission		
		Shallow donor + deep acceptor	$E_a \gg E_d$ and $E_a \gg kT$		High	
			d–a emission	Free electron–bound hole emission		
$E_i - E_k$[a]	Inner shell transitions	d–d (transitión metals) f–f (rare earth elements)	See low temperature emission	Weak coupling to conduction and valence band	Photolum. Low	Electrolum. High

[a] E_i, E_k – Energy of core levels (open shells).

Figure 2.17 Summary of the luminescence emission mechanisms in II–VI compounds (ref. 4 p. 116).

A number of empirical studies have been undertaken, with the intention of producing lower resistivity n–type material. Higher n–type conductivity obtained by annealing ZnSe in a Ga/Zn solution was thought to be associated with more efficient extraction of copper [40]. A similar finding was reported for ZnS, where it was found that the lowest resistivity could be obtained by heating the ZnS at 1000 °C in a molten mixture of Zn+1%Ga+$\frac{1}{2}$%Al [41]. A model was proposed to explain these observations, which took into account the fact that all the samples investigated were contaminated with copper [42]. It was proposed that in ZnS:Ga,Al three types of complex, namely (Ga^{+}_{Zn}–Al^{3+}_{Zn}), (Cu^{+}_{Zn}–Ga^{3+}_{Zn}) and (Cu^{+}_{Zn}–Al^{3+}_{Zn}) are formed, in which each of the ions in the pair are substituted at adjacent Zn^{2+} sites. These ion pairs are isoelectronic with the lattice since their overall charge balances that of two Zn^{2+} ions. The annealing treatment was found to suppress the self activated luminescence band in ZnSe (which is associated with acceptors formed by compensation) and excitonic emission, typical of much purer material, was obtained. It was suggested that the (Cu^{+}_{Zn}–Ga^{3+}_{Zn}) pair effectively gettered the residual copper, by forming a complex which was electrically neutral with respect to the lattice.

Although great progress has been made in producing n–type conductivity, good p–type conductivity in ZnS and ZnSe has not been achieved. Until recently it was thought that the difficulty in obtaining conductivity type conversion was due to some "intrinsic" properties of these materials. The so–called "self compensation" was attributed to the formation of acceptor type centres consisting of doubly ionised metal vacancies in association with a donor ion on a nearest metal site [43]. However, recent studies using high quality materials and more precise spectroscopic techniques, have stimulated new interest in the problem of obtaining bi–polar conductivity in the II–VI compounds [44]. The recent results indicate the importance of extrinsic impurities in the compensation mechanism. For example, Li substituted on a Zn site (Li_{Zn}) is known to form a relatively shallow (114 meV) acceptor in ZnSe [45]. At a concentration of $N_A \sim 10^{17}$ cm^{-3}, and without excessive compensation, this would give a room temperature carrier concentration of $p \sim 4 \times 10^{15}$ cm^{-3}, and for a hole mobility of $\mu \sim 10$ cm^2/V the resistivity would be $\rho \sim 200\ \Omega$ cm [46]. However, doping with Li in bulk ZnSe gives material with $p \sim 3 \times 10^9$ cm^{-3} and $\rho \sim 10^8\ \Omega$ cm. [47]. The compensation mechanism proposed involves the formation of Li interstitial sites (Li_I) which act as donor centres. Evidence for the existence of Li_I was found in electric field drifting experiments [46], and DAP luminescence studies have revealed a transition involving Li_I donors and Li_{Zn} acceptors [13]. It was suggested that quenching ZnSe:Li from high temperatures may produce good p–type conductivity by reducing the concentration of Li_I, although the drifting experiments imply that the conductivity would not be stable under an applied bias [46].

There have also been several attempts to incorporate group V elements as acceptors. Nitrogen forms a shallow acceptor in LPE [48] and MOCVD [49] grown material, with an estimated acceptor ionisation value of $E_A^N \sim 100$ meV [51]. Doping with phosphorous yields an acceptor with an ionisation energy $E_A^P \sim 19$ meV [52]. Unfortunately only high resistivity p–type ZnSe has been produced by nitrogen or phosphorous doping, and the cause for this remains unclear. Several claims of p–type conduction have been made, in both thin film material (eg $p = 5 \times 10^{17}$ cm^{-3}, $\mu_p = 2.5$ cm^2/Vs [53]) and bulk single crystals (eg $p = 3 \times 10^{15}$ cm^{-3}, $\mu_p = 20$ cm^2/Vs [54]). However, the p–type material was highly resistive, and it is difficult to make an unambiguous distinction between acceptor doped p–type layers and inversion layers formed at the metal semiconductor contact. For this reason it is necessary to consider alternatives to the p–n homojunction for minority carrier injection in ZnS and ZnSe.

2.3.2 The Schottky barrier

The Schottky barrier offers a means of injecting minority carriers into unipolar semiconductor materials, and this section gives an outline of the theory relevant to electroluminescent devices. Further information is available in a number of comprehensive reviews (see for example [55]).

When a metal and semiconductor, which are electrically neutral, are brought into contact (here we assume that the metal work function ϕ_m is greater than the semiconductor electron affinity χ_s), electrons flow from the semiconductor to the metal until the Fermi levels are aligned. The build up of negative charge in the metal is balanced by an equal and opposite charge in the semiconductor as conduction electrons recede from the surface. Since the semiconductor donor concentration is very much lower than the electron concentration in the metal, the depleted region of uncompensated donors extends for an appreciable distance into the semiconductor. Figure 2.18a shows the energy level diagram for the ideal case (no interface states) of a metal in contact with an n–type semiconductor. The barrier height is given by the Schottky–Mott relation [56,57]:

$$\phi_{bn} = \phi_m - \chi_s \tag{2.9}$$

The energy barrier for electrons leaving the semiconductor is the diffusion potential V_d. Under forward bias the band bending is reduced, and minority carriers (section 3.1) are injected into the semiconductor (figure 2.18b). Unfortunately, majority carriers are extracted more easily from the semiconductor, resulting in a very low minority carrier injection efficiency γ:

$$\gamma = \frac{J_p}{J_p + J_n} \tag{2.10}$$

where J_p and J_n are the hole and electron current densities respectively. Expressions for γ can be derived by analysis of the hole current components [58] and it has been shown that:

$$\gamma \propto exp\left[-\left(\frac{E_g - e\phi}{kT}\right)\right] \tag{2.11}$$

Thus γ is independent of any applied voltage. Calculations for the Au/ZnSe system ($E_g = 2.7$ eV, $\phi = 1.7$ eV) show that the theoretical injection efficiency is equal to 10^{-17}, which is too low to be of interest for a practical device. Consistent with this result, "ideal" Schottky contacts on ZnSe, Zn(S,Se) and ZnS, where there is no detectable interfacial layer, do not exhibit any electroluminescence under forward bias [59,60]. Under certain circumstances, a thin layer of insulating material between the metal and semiconductor can block the majority carriers and thus increase the minority carrier injection efficiency.

2.3.3 The metal insulator semiconductor diode

The energy band diagrams for the metal insulator semiconductor (MIS) structure at equilibrium and under forward bias are shown in figures 2.19a and 2.19b respectively. The metal Fermi level is now free to move with respect to the semiconductor band structure. Under forward bias a significant fraction of the applied voltage is dropped across the insulating layer, and the Fermi level of the metal is displaced towards the semiconductor valence band. Thus the minority carrier injection ratio can be enhanced, and this results in an increase in electroluminescent efficiency over that which can be achieved with MS contacts [61]. The optimum I–layer thickness is a compromise between two conflicting requirements: it should be thin enough to allow efficient tunnelling, but thick enough to maintain an adequate voltage drop in order to drive the tunnelling process. In an experimental and theoretical analysis of the MIS structure, the optimum I–layer thickness was found to be 30 Å for the Au/SiO_2 system in which a minority carrier injection ratio of 20% was reported [62]. A further enhancement in γ is possible by selection of an insulator with a low work function (for n–type semiconductors). Figure 2.19c shows how a "semi–permeable membrane" can be formed, where the tunnelling barrier for holes is reduced relative to that for electrons [63].

Light emission from forward biased ZnS and ZnSe diodes, in which minority carriers are injected through an MIS contact, has been observed by many authors (for a review see [64]). Enhancement of γ and hence electroluminescent efficiency was observed with increasing I–layer thickness. The quantum efficiency of the diodes was found to increase by a factor of roughly 10^4 with an insulator thickness of up to 50 nm [65], with little subsequent change up to 400 nm [66]. In this case the I–layer is too thick for tunnelling to occur, and an alternative injection mechanism based on Auger energy transfer has been proposed [67]. This model will be discussed more fully in section 3.1.

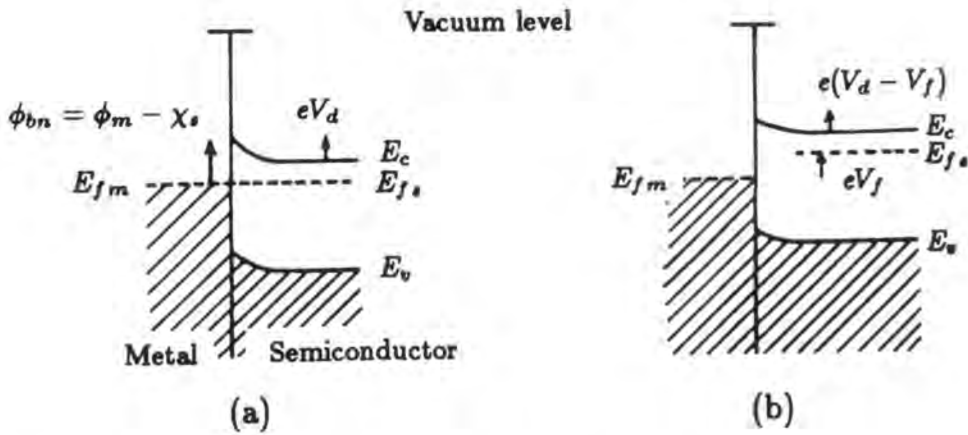

Figure 2.18 Energy diagrams for a metal to n–type semiconductor contact under (a) equilibrium and (b) forward bias.

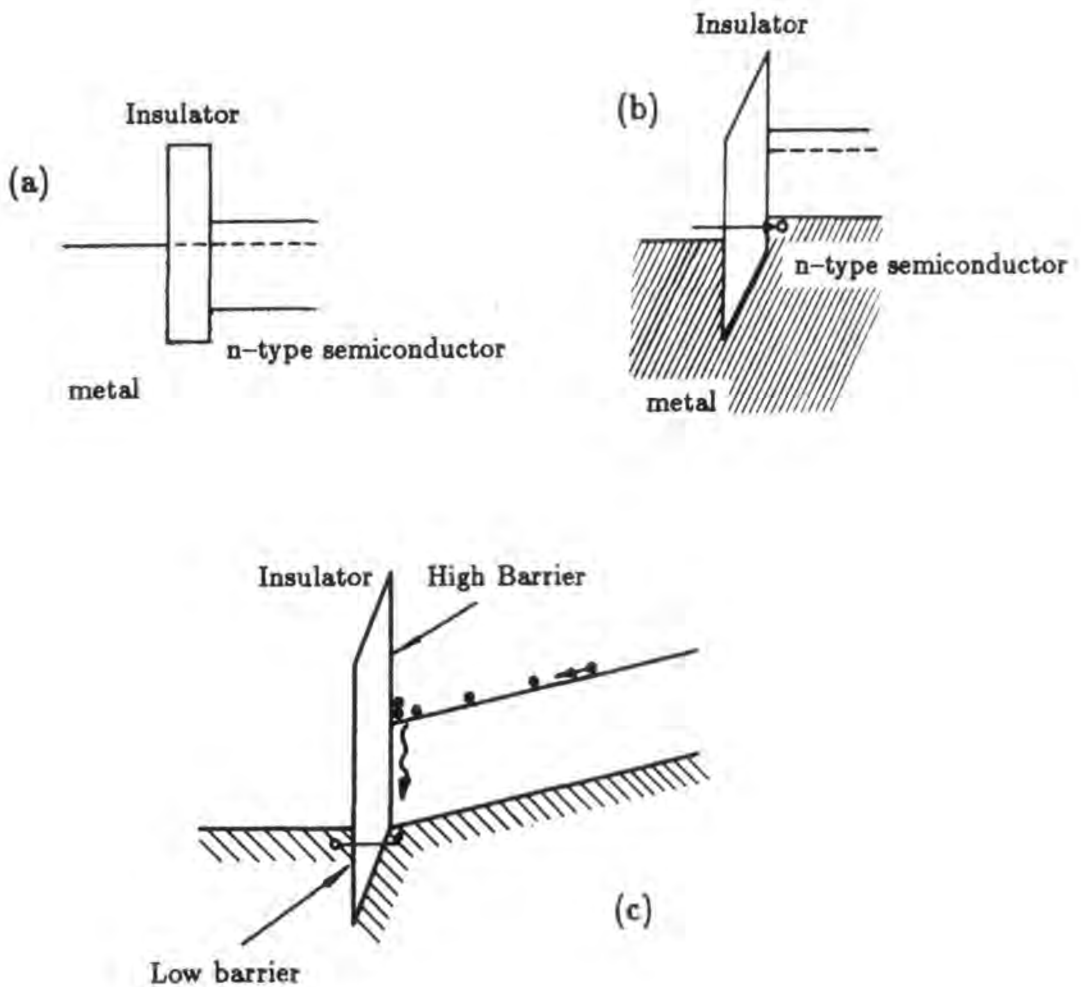

Figure 2.19 Energy diagrams for a metal insulator n–semiconductor (MIS) contact under (a) equilibrium and (b) forward bias, (c) partial suppression of majority carrier extraction (ref. 63).

2.3.4 The p–n junction

Although it has not so far been possible to produce p–n homojunctions in the II–VI compounds, alternative p–n heterojunction structures have been investigated and proposed. The p–n junction remains an attractive proposition since a high minority carrier injection ratio, coupled with the high luminescent efficiency of the II–VI compounds, would yield a very efficient light emitting diode (LED). It has been calculated that a current of 1 mA mm^{-2} passing through a p–n junction in a II–VI compound emitting in the green, would have a surface brightness comparable to that of a tungsten lamp operating at 3000 K [64]. The energy level diagram for the p–n junction at equilibrium is shown in figure 2.20a. Under forward bias, the potential barrier is lowered by the applied voltage (V) as shown in figure 2.20b and a current will flow. The diffusion current J_d represents the injection of minority carriers according to the Shockley equation:

$$J_d = e\left[\left(\frac{D_n n_p}{L_n} + \frac{D_p p_n}{L_p}\right)\right]\left[exp\left(\frac{eV}{kT}\right) - 1\right] \tag{2.12}$$

where D_n and D_p are the carrier diffusion coefficients, n_p and p_n are the equilibrium minority carrier concentrations, and L_n and L_p are the carrier diffusion lengths. There are several possible loss mechanisms which cause deviations from equation 2.12 [68]. These include, recombination at interface states in the depletion region, interband tunnelling, and field effects in the bulk semiconductor. However, they are generally insignificant at LED operating voltages, and practical p–n homojunction LEDs can have values of γ close to unity.

The potential of the p–n junction in electroluminescent devices has stimulated the investigation of a number of alternative p–n junction structures for use in the II–VI compounds. For example, yellow–orange electroluminescence was obtained from a p–n heterojunction consisting of an n–type ZnSe crystal with a p–type overlayer of ZnTe [69]. Unfortunately, the band gap gradient (figure 2.21) implies that minority carriers are more easily injected into the ZnTe than the ZnSe. ZnTe is not strongly luminescent, so many of the injected electrons recombine non–radiatively. More recently, energy band diagrams for the ZnSe–ZnTe and $ZnS_{0.5}Se_{0.5}$–ZnTe superlattices have been calculated, taking into account the lattice mismatch between the materials. These calculations indicate that the $ZnS_{0.5}Se_{0.5}$ (30 Å)– p–type ZnTe (5 Å) superlattice would be a p–type material with $p = 10^{17}$ cm^{-3}. Such a superlattice would form an efficient p–type injecting layer to n–type ZnSe [70].

2.4 Hot electron impact luminescence

Impact excitation is a majority carrier process, and can be used to excite luminescence in the II–VI compounds where it is difficult to make light emitting diodes using p–n junctions. It is a high field process, and so introduces considerable techno-

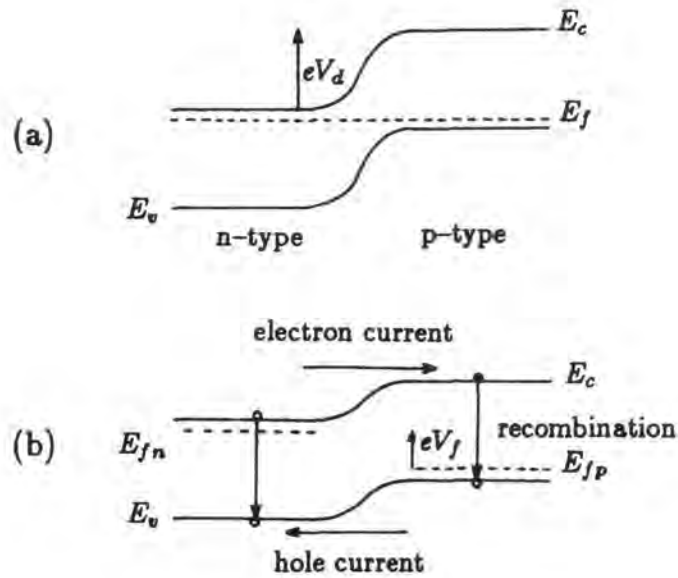

Figure 2.20 The p–n junction under (a) equilibrium and (b) forward bias.

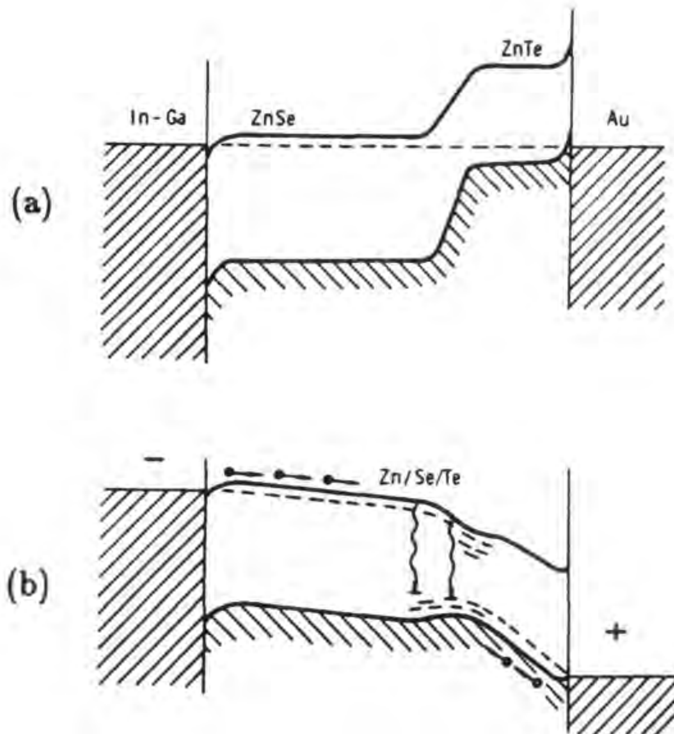

Figure 2.21 The ZnSe–ZnTe heterojunction: (a) equilibrium, (b) forward bias (ref. 69).

logical difficulties, particularly with regard to device maintenance. However, impact luminescence devices are particularly well suited to the production of large area flat panel displays, and their considerable commercial potential has stimulated continued interest in the II–VI compounds.

2.4.1 Hot electron generation and impact excitation

The basic process for hot carrier generation is acceleration of electrons in a high electric field, until they acquire a kinetic energy which is much greater than kT. The electric field may be maintained in either:

(1) depletion regions of reversed biased MS contacts [71],
(2) high resistivity I–layers in MIM or MIS structures [72].

In both structures the applied voltage is dropped over a thin insulating layer, developing fields of the order of 10^6 V cm^{-1} at voltages of approximately 100 V. The band diagrams for a reversed biased MS contact, and a MIS structure, are shown in figures 2.22a and 2.22b respectively. The injection mechanism will be discussed further in section 6.1, however, it is instructive to consider here the physical mechanisms of electron heating and impact luminescence [72].

The average energy E gained by a conduction electron in an electric field is:

$$E = e\epsilon\bar{l} \tag{2.13}$$

where ϵ is the field strength and $\bar{l}$ the electron mean free path. The main electron cooling process is phonon emission. Phonon coupling in ZnS is dominated by optical phonons, and the LO–phonon interaction energy is given by [73]:

$$E_{phon} = 2h\nu\left(\frac{exp(h\nu/kT) - 1}{exp(h\nu/kT) + 1}\right) \tag{2.14}$$

E_{phon} is the minimum energy requirement for the *electron* before it can interact with a LO–phonon, and in ZnS this is $E_{phon} \sim 0.06$ eV. Electrons with energy greater than E_{phon} are likely to lose energy by optical phonon emission. However, if an electron acquires energy $E \geq 2E_{phon}$ over a path length $\bar{l}$, the likelihood of phonon cooling becomes smaller since multi–phonon emission involving energy quantisation is a less probable event. The electron energy then rapidly increases to a level at which ionisation and impact excitation becomes possible. The threshold field ϵ_T for the production of such hot electrons can be determined from equation 2.13 by setting $E = E_{phon}$, and noting that the mean free path of an electron in ZnS is of the order of 10 Å [73]. These values give the minimum field for ionisation and impact excitation as $\epsilon_T \sim 0.60 \times 10^6$ V cm^{-1}. For fields greater than ϵ_T , electrons rapidly acquire a kinetic energy which

is much greater than kT. If their energy is comparable with the ionisation energy of either the band gap, or the binding energy of a carrier to a defect, then ionisation can occur, producing either electron–hole pairs or isolated carriers. These carriers are accelerated in the field and can themselves cause further ionisation events, leading to current avalanching. Impact excitation of the Mn^{2+} centre can occur when the electrons have energies greater than 2.3 eV, which is the energy difference between the ground and excited states. The characteristic yellow 2.12 eV light emission is produced during the decay process. These theoretical results are consistent with the experimental observations shown in figure 2.23, where both avalanching and light emission are only observed for fields greater than 0.6×10^6 V cm^{-1}.

Having now considered some of the physical principles involved in hot electron generation and impact excitation, the following section describes the practical realisation of hot electron luminescence.

2.4.2 Electroluminescent panel displays

An electroluminescent (EL) panel has been defined [74] as "a large area display which is capable of covering an area of 100 cm^2 or more, or alternatively, is capable of displaying at least 3500 pixels". In general these are high field devices, because the current requirements for injection luminescent devices of this area are prohibitive. Since the first observation of high field EL by Destriau [75], his AC capacitatively coupled cell shown in figure 2.24a has been refined to a solid state device, and several variants are now available commercially.

Many alternative types of EL panel displays are also available, and these may be categorised: (I) according to their mode of operation as AC or DC coupled; and (II) according to structural configuration, as powder or thin film cells. The capacitatively coupled (AC) thin film structure [76] is possibly the most successful device at present, due to its exceptionally bright and stable operation. A typical AC coupled structure is shown in figure 2.24b. The insulator layers (Y_2O_3 or Si_3N_4) are designed to allow an adequate displacement current, but provide sufficient current limiting to prevent any destructive avalanching. The main disadvantage of the AC EL panel lies in the complexity and cost of the bi–polar driving circuit, although this is offset to some extent by an inherent device memory effect (hysteresis) which simplifies the addressing of a large number of pixels.

Since it was first reported [77], the DCEL powder cell has also been considerably refined in order to satisfy a large number of operational requirements. The main difficulty, which is to provide a perfectly uniform field within a powder phosphor, has been overcome using an electrical forming process. The Zn in the outer layer of the ZnS:Mn,Cu phosphor particles is replaced by copper in an electroless process, forming a conducting Cu_xS coating around each particle [78]. The phosphor is then mixed

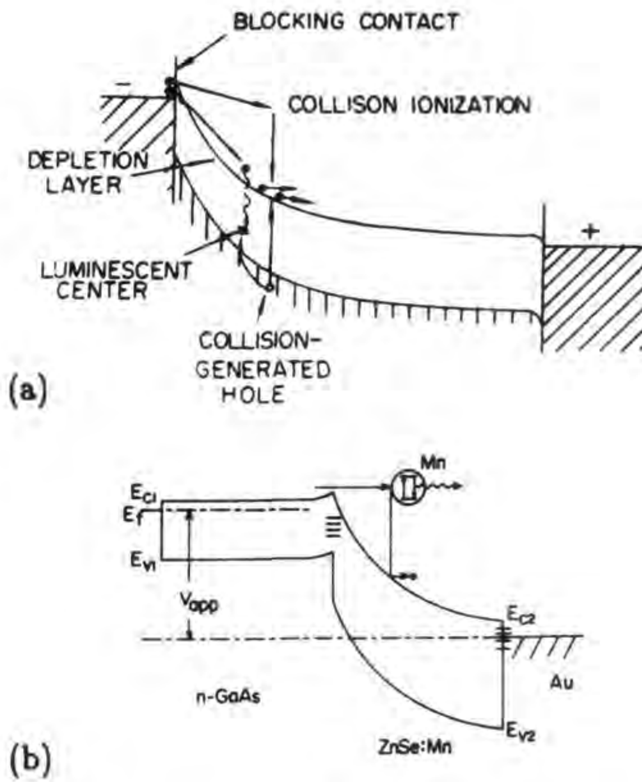

Figure 2.22 Band diagrams of structures used for high field electroluminescence (a) reverse biased MS contact, (b) forward biased MIS structure (ref. 67,69).

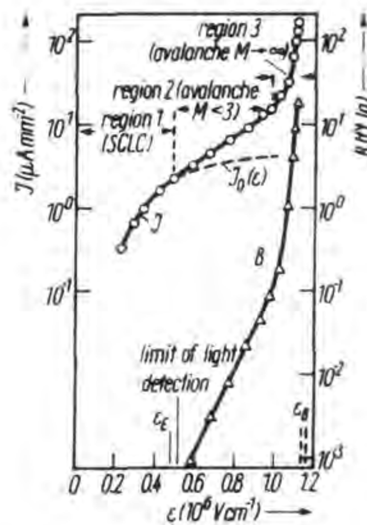

Figure 2.23 Avalanching and electroluminescence in ZnS:Mn film as a function of electric field strength (ref. 72).

with a fixed weight of organic binder (polymethylmethacrylate) and deposited on to transparent conducting oxide coated glass. "Forming" is initiated by applying a bias of +10 V to the transparent electrode, which results in copper migrating from the positive electrode and leaving behind a layer of ZnS phosphor, as shown schematically in figure 2.25. The process is continued until a complete plane of highly resistive material is formed at the positive electrode, and a uniform electric field can be established despite the many geometrical irregularities. DCEL powder panels have useful lifetimes of several thousand hours, and the failure mode is non-catastrophic. The un-formed Cu_xS acts as a *local* load resistor, so that if an area of instability develops, localised current limiting prevents catastrophic breakdown. The main disadvantage of the DCEL powder display is the need for copper doping, since migration of copper under the applied field can seriously reduce the device lifetime.

More recent work has been concentrated on DCEL in copper free thin film ZnS:Mn, which can be deposited by a variety of techniques including; metalorganic chemical vapour deposition, thermal evaporation, and RF diode sputtering. A semi-insulating control layer between the phosphor and electrodes is required in order to provide localised current limiting, in the same way as the Cu_xS layer does in powder devices. This control layer is deposited either as a powder in hybrid (powder control layer and thin film phosphor) devices [79], or by sputtering in all thin film structures [80]. The thin film structure shows great promise as a commercial flat panel display, however many problems remain to be solved, notably the prevention of localised destructive breakdown in the phosphor layer. This problem is currently the subject of intense investigation, and will be discussed further in chapter 6.

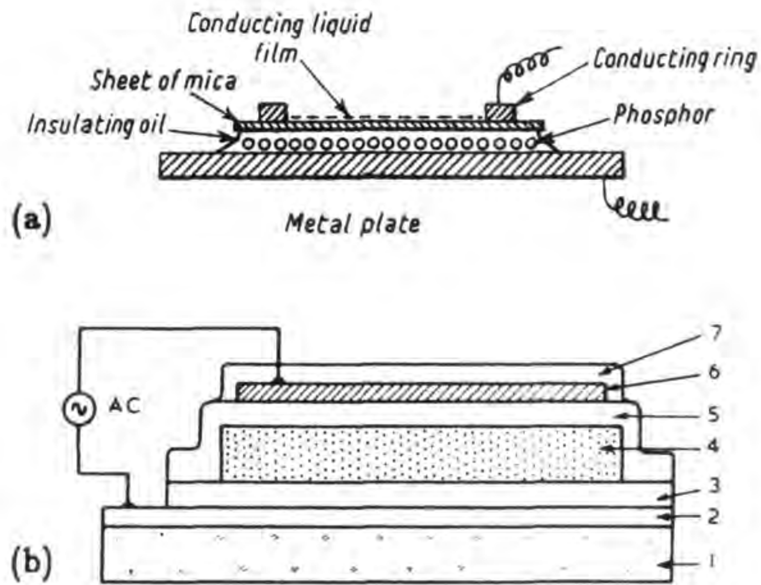

Figure 2.24 AC electroluminescent panels (a) cell originally used by Destriau, (b) commercial thin film cell (1) glass substrate (2) transparent electrode (3) insulating layer (4) ZnS:Mn (5) insulating layer (6) metal electrode (7) encapsulation (ref. 75,78).

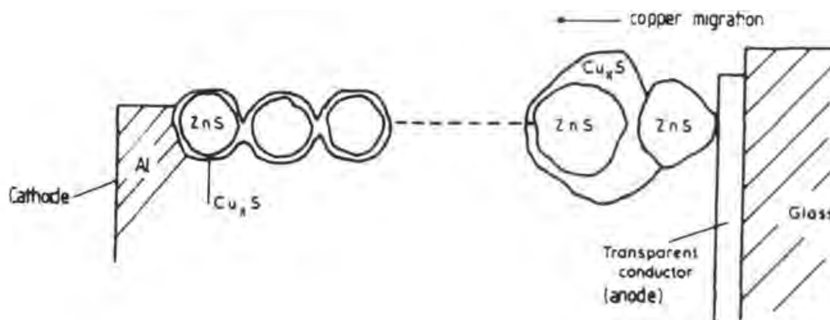

Figure 2.25 Structure of a formed DCEL powder panel (ref. 78).

CHAPTER THREE

ELECTROLUMINESCENCE IN BULK ZnSe

3.1 Introduction

Minority carrier injection electroluminescence (EL) in the II–VI compounds was first observed in CdS MIS devices [1] with I-layers sufficiently thin to allow minority carrier tunnelling [2]. Subsequently, research was concentrated on ZnS and ZnSe which have the potential of allowing efficient EL over a wider spectral range. ZnS and ZnSe MIS devices were investigated by many authors, and a variety of different I–layer materials employed. These have included SiO_2 [3], ZnO [4], ZnS [5], and more recently, organic I-layers deposited using the Langmuir–Blodgett technique [6]. A common feature of this work is the observation that the I–layer thickness required to optimise the EL efficiency exceeds that which allows direct quantum mechanical tunnelling. For example, the EL efficiency of the Au/ZnO/ZnS (MIS) system increases sharply with I-layer thickness up to 50 nm, and remains approximately constant thereafter [7]. Similar findings are reported for the Au/ZnSe/ZnSe (MIS) system, where the efficiency remains constant with I-layers of up to 400 nm in thickness (figure 3.1) [8].

The energy level diagram for a proposed model [8] of hole injection in the forward biased Au/ZnSe/ZnSe (MIS) system is shown in figure 3.2. Electrons leaving the semiconductor are accelerated by the electric field in the I-layer, and excite electrons below the metal Fermi level through an impact ionisation mechanism. In essence, the model predicts the formation of a deep hole population in the metal, with a maximum energy below the metal Fermi level corresponding to the barrier height. This may be thought of as an energy mirror–image of the energetic electrons arriving over the barrier [9]. Some of the holes migrate through the valence band of the insulator, and radiative recombination with electrons occurs in the semiconductor. The model is similar to one first proposed for MS structures without any interfacial layer [10], where an inversion layer is formed when the relationship:

$$V_d = \phi_m - \chi_s > \frac{E_g}{2} \tag{3.1}$$

is satisfied. Electrons arriving at the metal from the semiconductor conduction band are able to transfer their energy to electrons below the Fermi level of the metal, creating energetic holes capable of entering the valence band of the semiconductor (figure 3.3). Experimental evidence for the validity of these models was obtained in an extensive study of blue light emitting ZnS MS and MIS diodes [5]. With MS Schottky diodes, forward bias EL was only observed using metal electrodes such as Au or Pt where the barrier height exceeded $\frac{E_g}{2}$, so that the ZnS at the interface was in slight inversion. With

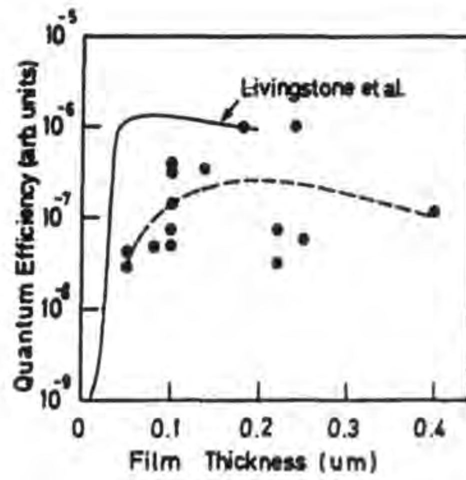

Figure 3.1 Quantum efficiency of ZnSe MIS diodes as a function of I–layer thickness (ref. [8]).

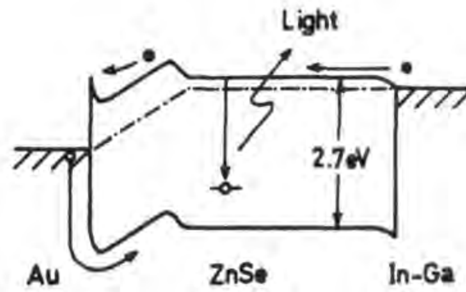

Figure 3.2 Minority carrier injection in the forward biased Au/ZnSe/ZnSe MIS junction (ref. [8]).

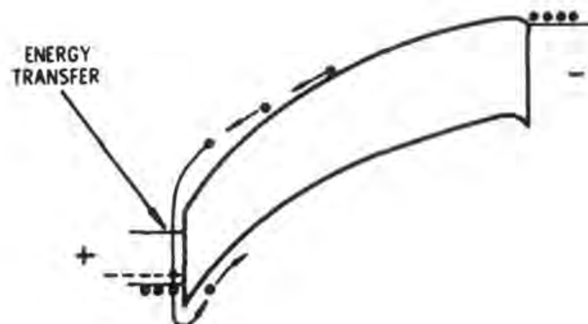

Figure 3.3 Minority carrier injection in a MS junction by energy transfer from electrons to holes (ref. [10]).

metals such as Cu or In, which result in barrier heights of less than $\frac{E_g}{2}$, no inversion layer was formed, and EL was not observed. However, injection EL was obtained in MIS structures incorporating these electrode materials. Furthermore, direct evidence for the production of hot holes within the metal by an Auger process was provided by the identification of plasma radiation, emitted when hot electrons entered the metal [5]. Figure 3.4 shows the potential energy model for the Au/ZnO/ZnSe barrier, which was developed on the basis of experimental measurements of the barrier height [11].

A major factor in determining the minority carrier injection ratio is the hole creation rate. In a recent theoretical analysis the energy distribution of the hole population was calculated using perturbation theory [12]. It was assumed that hole transport via the insulator valance band was unimpeded, and that conduction was limited by the supply of holes to the metal–insulator interface. Applied to the Au/ZnS/ZnS (MIS) system, with a barrier height of 2.2 eV, the probability of an injected electron creating a hole with sufficient energy to enter the valence band of the insulator was calculated to be approximately 2%. Since the electron mean free path in ZnS is only 1 nm [13], the injected electron energy is not a strong function of the electric field in the insulator. Thus, assuming unimpeded hole transport through the insulator valence band, the minority carrier injection ratio will remain approximately constant once a positive field is established in the I–layer. The II–VI compounds are efficient phosphors, with as many as 1% of holes injected into the valence band recombining radiatively [14]. Therefore the model predicts an overall quantum efficiency of approximately 2×10^{-2} %, which compares well with experimentally determined values [15].

Unfortunately, despite the fact that external quantum efficiencies of up to 0.05% have been obtained, reproducible operating characteristics have not been achieved. However, there remains considerable current interest in the use of single crystal ZnS and ZnSe for EL applications, and although much of the early work was of an empirical nature, recent work on a firmer theoretical foundation has provided more encouraging results. Theoretical and experimental work based on the injection model discussed above suggests that the injection efficiency is dependent on the height of the metal–semiconductor barrier. For this reason, the extent to which the minority carrier injection ratio can be enhanced by using an electrode material with an electronegativity greater than gold has been investigated [16]. Polymeric sulphur nitride, SN_x, is a quasi 1–dimensional metal [17] which allows the production of ZnS diodes with barrier heights approximately 0.75 eV higher than those obtained using gold. Figure 3.5 shows the measured external quantum efficiency of ZnS LEDs as a function of barrier height. The relationship follows the same general trend established for other contact materials, and shows that the EL efficiency may be increased by a factor of 100 when SN_x electrodes are used. Thus the wide band gap II–VI compounds remain promising materials for LED fabrication.

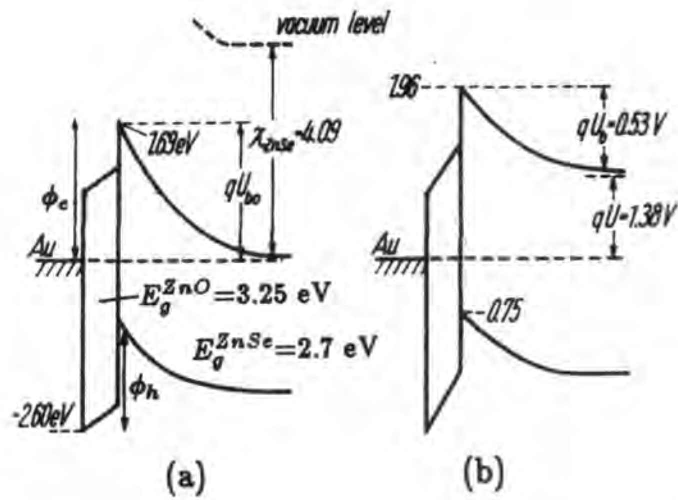

Figure 3.4 Potential energy diagram of the Au/ZnO/ZnSe system (a) at sero bias, (b) under forward bias (ref. [4]).

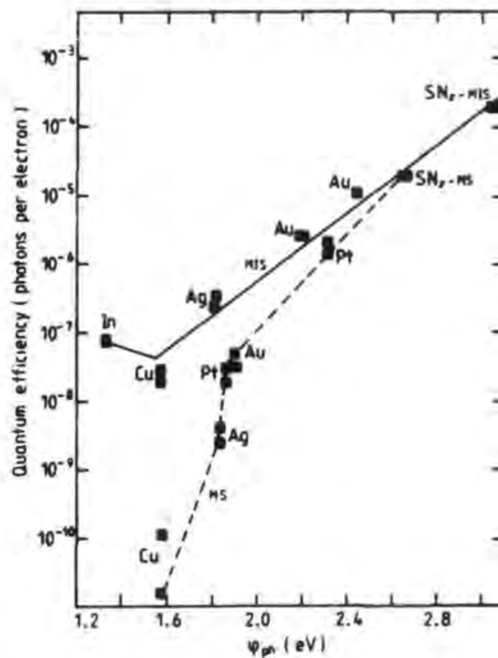

Figure 3.5 Quantum efficiency of ZnS MS and MIS diodes as a function of photoelectric barrier height (ref. [16]).

This chapter describes the fabrication and characterisation of bulk single crystal ZnSe injection luminescence devices. The optical and electrical characteristics of these devices were recorded in order to identify the electronic transitions responsible for the electroluminescent spectrum, and to provide a starting point for the development of thin film epitaxial devices.

3.2 Device fabrication

3.2.1 Source purification and crystal growth

Single crystal ZnSe was grown from a high purity powder source. The ZnSe powder (Merck Suprapur, with impurities quoted as Cu 0.5 ppm, Ni 0.1 ppm, Co 0.1 ppm and Fe 1.0 ppm) was first purified by sublimation in a stream of argon, as shown in figure 3.6. A silica boat was loaded with 50 g of ZnSe powder, and the system assembled with the deposition liners in contact, thus ensuring that the configuration was reproducible from one run to the next. The powder was maintained at a temperature of 600 °C in a stream of high purity argon for 10 hr in order to remove volatile impurities. The temperature was then increased to 1165 °C for the sublimation, and with an argon flow rate of 500 ml/min, approximately 20 g of ZnSe were deposited on the inner wall of the first liner within 5 days. Impure material deposited on the second (cooler) liner was discarded.

Single crystal ZnSe was grown from the purified powder using the vapour phase growth system [18] illustrated in figure 3.7. ZnSe was sublimed at a temperature of 1165 °C to the top of the tube, where growth took place at a temperature of about 1100 °C. Elemental zinc in the tail reservoir was held at a temperature of 555 °C in order to maintain the vapour in stoichiometric proportions. The tube was pulled through the furnace at a rate of 15 mm per 24 hr, and a boule 3–4 cm long consisting of several large grains was grown in 140 hr.

3.2.2 Impurity extraction and doping

As–grown crystals of ZnSe are highly resistive ($\sim 10^{12} - 10^{14}$ Ω cm), and in order to reduce the resistivity to a range suitable for device applications ($\sim 1-100$ Ω cm), the crystals were heated in liquid zinc. The so–called zinc extraction process is particularly effective in removing copper contamination [19], which forms deep acceptors in ZnSe [20] and compensates any donors introduced into the material. Another effect of the process is to change the stoichiometry and introduce an excess of zinc. Any zinc vacancies in the ZnSe, which act as acceptors, are filled, and shallow donors in the form of selenium vacancies or zinc interstitials introduced [21]. It is also possible to introduce foreign donors by adding suitable impurities to the zinc melt and for this work some ZnSe was doped with gallium during the extraction process. Gallium doping also offers the

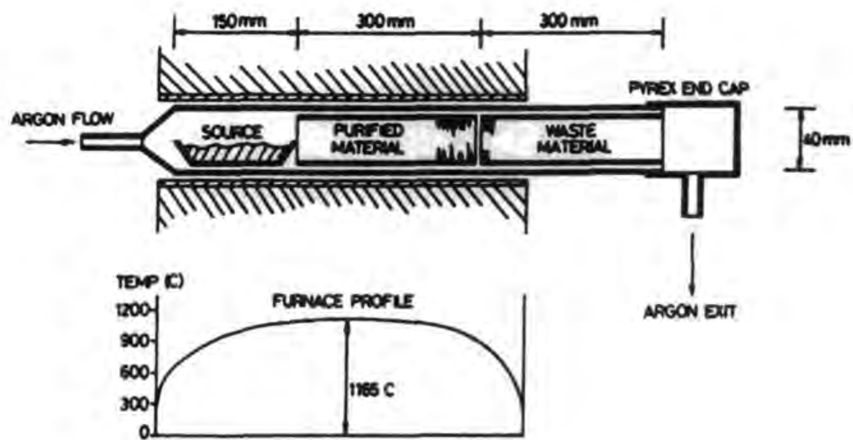

Figure 3.6 Purification of ZnSe by argon flow sublimation.

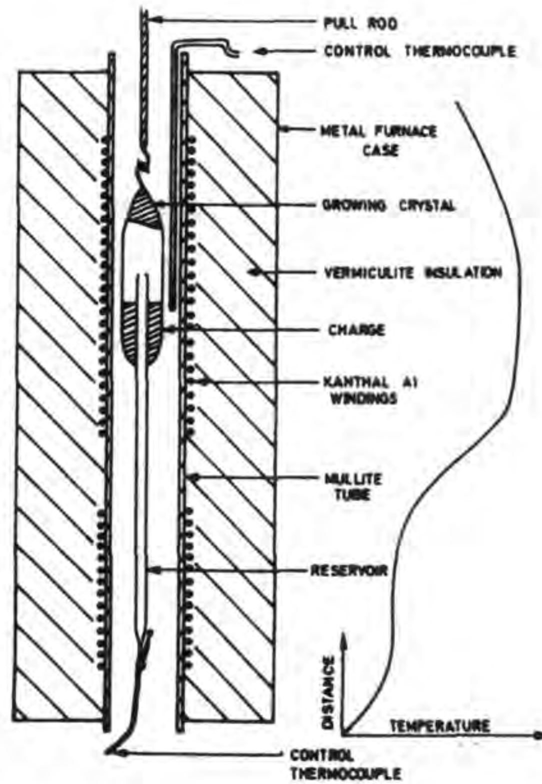

Figure 3.7 Experimental arrangement for the growth of ZnSe from the vapour phase (ref. [18]).

possibility of neutralising the effect of any copper impurity by forming the inert complex (Cu^{+}_{Zn} – Ga^{3+}_{Zn}), as discussed in section 2.3.1. Photoluminescence studies indicate that doping with gallium suppresses the copper green emission in ZnSe [22], and an attempt was made to reproduce this result in EL devices.

Single crystal ZnSe die, with dimensions $3 \times 3 \times 2$ mm^3, were cut from the boule and sealed in a silica tube containing zinc and any dopant elements. The tube was suspended in a vertical furnace and held at temperature (600 or 850 °C) for 5 days. On completion, the tube was removed from the furnace and inverted in order to separate molten zinc from the die, which was restrained by a small constriction in the tube.

3.2.3 Electrical contacts

The ZnSe die were mechanically polished using 1 μm alumina powder until two flat and parallel surfaces were obtained, and then chemically polished for 2 min in a solution of 2% bromine in methanol. This solution was diluted with methanol until the bromine concentration became negligible, and the die immersed in carbon disulphide in order to remove Se–Br compounds formed on the surface. An ohmic contact was prepared by pressing indium onto one chemically polished face, and then heating to 220 °C in an argon ambient for 10 min. After protecting the indium contact with lacomit, the large area face opposite this electrode was repolished and etched, and a gold Schottky contact deposited by thermal evaporation at 10^{-6} torr.

3.3 Optical measurements

3.3.1 Direct current electroluminescence

Electroluminescent emission spectra were recorded using the computer controlled system shown in figure 3.8. Devices were operated in forward bias from a constant current supply, and the EL emission was focussed onto the entrance slits of a Hilger and Watts D330 grating monochromator. A stepper motor allowed wavelength scans to be made under computer control with a wavelength step of 1.25 Å. The output from the monochromator was measured using an EMI 9558B photomultiplier (PM) tube in conjunction with a Brookdeal 5002 current pre–amplifier and 9502 lock–in amplifier. The amplifier was connected, through suitable attenuation and protection circuits, to an analogue input port on the computer. In operation, the computer was programmed to step through the required wavelength range and record the EL intensity at each interval. If the signal was noisy several readings were made and an average value recorded. The microcomputer was subsequently used to process the spectra, making corrections for the spectral response of the PM tube, and for the non–linear energy dispersion of the monochromator.

Figures 3.9a and 3.9b show typical EL emission spectra, recorded from ZnSe MS

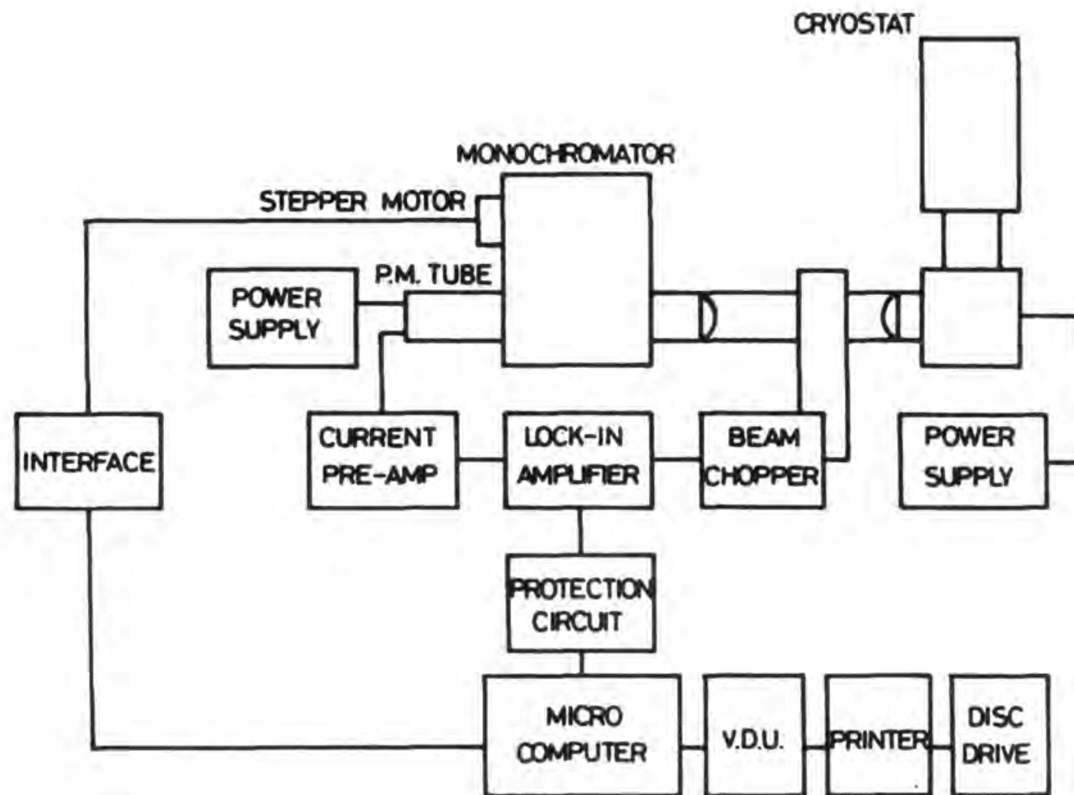

Figure 3.8 Schematic diagram of the automated electroluminescence system.

devices operating under forward bias at 77 K. Figure 3.9a shows the spectrum obtained from ZnSe which had been heated in molten zinc containing 1 wt% Ga at 600 °C for 5 days. The spectrum contains contributions from both deep centre and near band edge (NBE) emissions. NBE emission will be discussed in the following section, but it is useful to consider here the effect of gallium doping on the deep centre emission. Identification of the centre responsible is hindered by the broad nature of the band, and the fact that several different transitions occur in the same spectral region. These include the self activated (SA) (1.92–2.06 eV), copper green (2.34 eV), and the copper red (1.95 eV) emission bands [23]. Of interest here is the observation (figure 3.9b) that re–heating the same sample in Ga/Zn for a further 5 days at 850 °C considerably reduced the intensity of the deep centre emission. This is consistent with the results obtained (figure 3.10) in a separate study of photoluminescence (PL) in ZnSe. The PL spectrum recorded after heating ZnSe in Zn/Ga at 600 °C was dominated by deep centre (copper green) emission. In contrast, samples heated in the same melt at 850 °C showed only NBE emission [22].

3.3.2 Time–resolved electroluminescence

The time–resolved luminescence (TRL) technique involves recording the luminescent spectrum of a material at intervals after an excitation pulse. The increased spectral resolution and kinetic information obtained can considerably simplify the identification of radiative transitions in luminescent materials. Most TRL studies reported in the literature are concerned with photoluminescence excited by either a pulsed laser or discharge tube. In this work the TRL technique was used to examine the NBE emission from ZnSe MS LEDs, in which luminescence was excited using a pulsed power supply.

Figure 3.11 shows a block diagram of the time-resolved EL (TREL) system, in which a microcomputer provided both system control and the data transfer and analysis functions required to record EL transients over a range of wavelength intervals [24]. TREL spectra were recorded from ZnSe LEDs operated at 77 K, with the sample mounted in a liquid nitrogen cooled cryostat (Oxford Instruments D10200). The devices were pulsed in forward bias at 100 Hz with a 2% duty cycle at currents of up to 200 mA. For each wavelength interval, selected by a stepper motor on the monochromator, the digital storage oscilloscope (DSO) (Gould 1425) was triggered on the falling edge of an excitation pulse and the luminescent decay transient recorded. The DSO was programmed to average up to 256 transients, thus reducing the effect of noise from the PM tube. The stored transient was transferred to the microcomputer and then to disc for subsequent analysis. TREL spectra were derived by selecting points corresponding to specific delay times from transients recorded over a range of wavelengths. The spectra were corrected for the PM tube response, and the relative luminescent intensity was plotted as a function of photon energy.

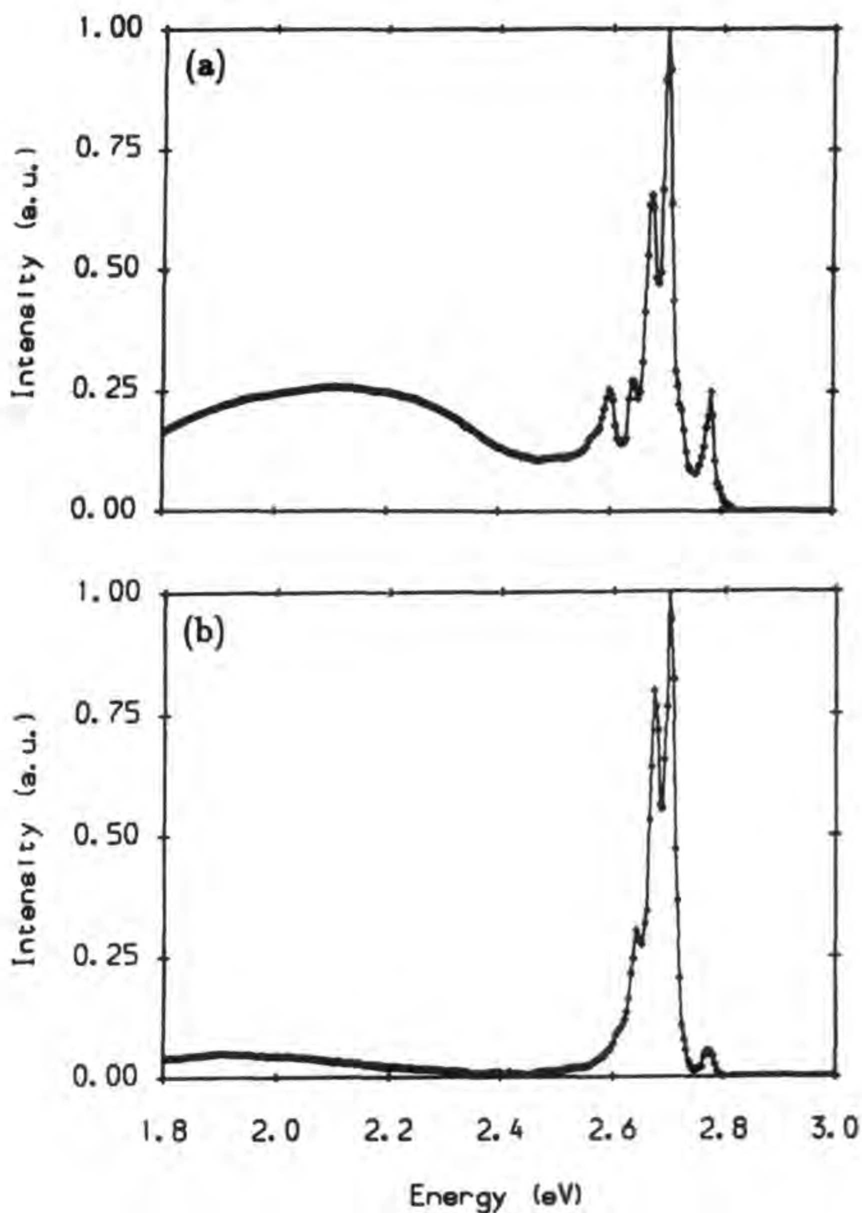

Figure 3.9 Spectral distribution of the electroluminescence at 77 K from ZnSe diodes treated in Zn/Ga at (a) 600 °C, (b) 850 °C.

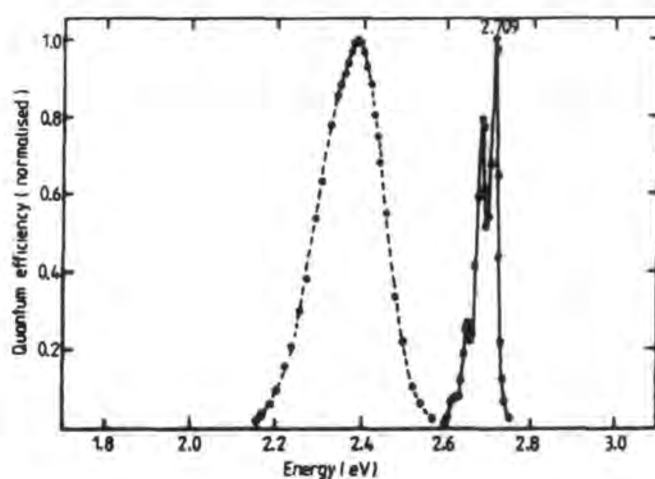

Figure 3.10 Photoluminescence emission at 80 K from samples of ZnSe after heating in Zn/Ga at 600 °C (broken curve) and 850 °C (full curve) (ref. 22]).

Figure 3.12a shows part of a conventional steady state (DC) EL spectrum from a ZnSe LED operating in forward bias. The spectrum is dominated by two peaks; however, as is usually the case with DC spectra, the bands are too broad to allow identification of the electronic transitions. Figure 3.12b shows the time–resolved spectrum taken from the same sample. Now the bands are well resolved and it is possible to make comparisons with published data. The peak assignments in figure 3.12b have been made on the basis of comparisons with published photoluminescence data, using the labelling convention shown in figure 2.8. The peak positions of the Q_0(FB) and Q_0(BB) bands correspond closely to the Li acceptor free to bound and bound to bound (DAP) transitions [25]. There is an overlap between the P_0(FB) (sodium acceptor free to bound) and Q_0(BB) transition peaks, although at the relatively high temperatures used for this work the free to bound transition will dominate. The peak labelled P_0(BB) corresponds to the sodium acceptor DAP transition [26]. These assignments must be regarded as tentative, since a study of devices deliberately doped with the respective acceptors was not attempted. However, atomic absorption analysis of the ZnSe revealed contamination with sodium and lithium (acceptor type impurities) at concentrations of 1.0 ppm and 0.01 ppm respectively.

3.4 Electrical characterisation

3.4.1 Photoelectric response

Irradiation of an MS contact with monochromatic light of energy $h\nu \geq e\phi_{bn}$ can result in electrons from the metal being excited over the energy barrier. For a Schottky barrier, the photocurrent per absorbed photon (R) is given by [27]:

$$R = C(h\nu - e\phi_{bn})^2 \qquad \text{for} \qquad e\phi_{bn} \leq h\nu < E_g \tag{3.2}$$

where C is a constant, $h\nu$ the energy of the incident radiation, and $e\phi_{bn}$ the barrier energy. Thus a plot of $R^{\frac{1}{2}}$ *vs* $h\nu$ (Fowler plot) is linear, with an intercept corresponding to the energy barrier presented to electrons. The photoelectric measurement is the most direct and accurate method of determining the barrier height [28], although errors can arise as a result of deep centres in the semiconductor contributing to the total photocurrent [29].

The photoelectric response of ZnSe MS diodes was recorded using the automated system described in section 3.3.1. A quartz halogen lamp was used in conjunction with the system in order to provide a monochromatic light source, and the photocurrent measured using the same lock–in amplifier arrangement. The spectrum was corrected for the spectral emission characteristic of the lamp, which was recorded using a calibrated PIN detector. Figure 3.13 shows a typical Fowler plot for a ZnSe MS device, where the intercept corresponds to a barrier height $\phi \sim 1.64$ eV, in good agreement with

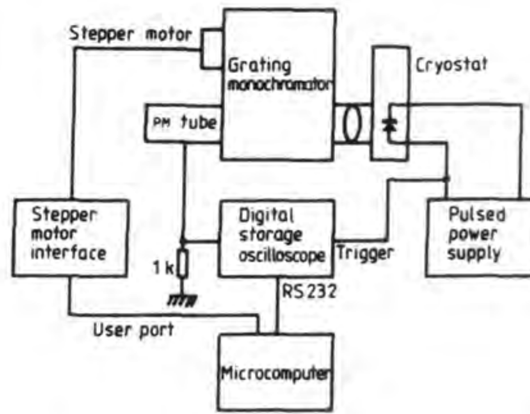

Figure 3.11 Schematic diagram of the microcomputer based TREL system.

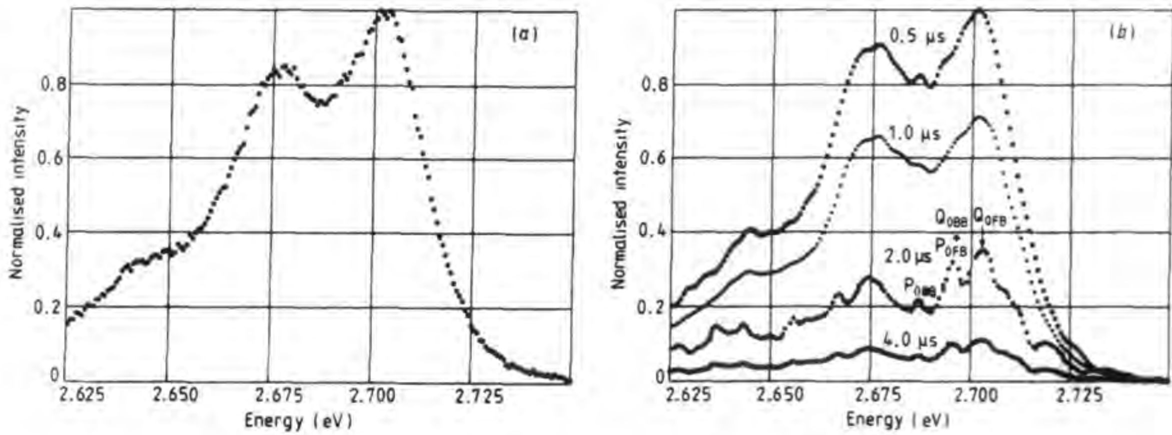

Figure 3.12 (a) DC EL spectrum at 70 K from a ZnSe LED operating in forward bias at 50 mA, (b) TREL spectra from the same sample at specified delay times after excitation.

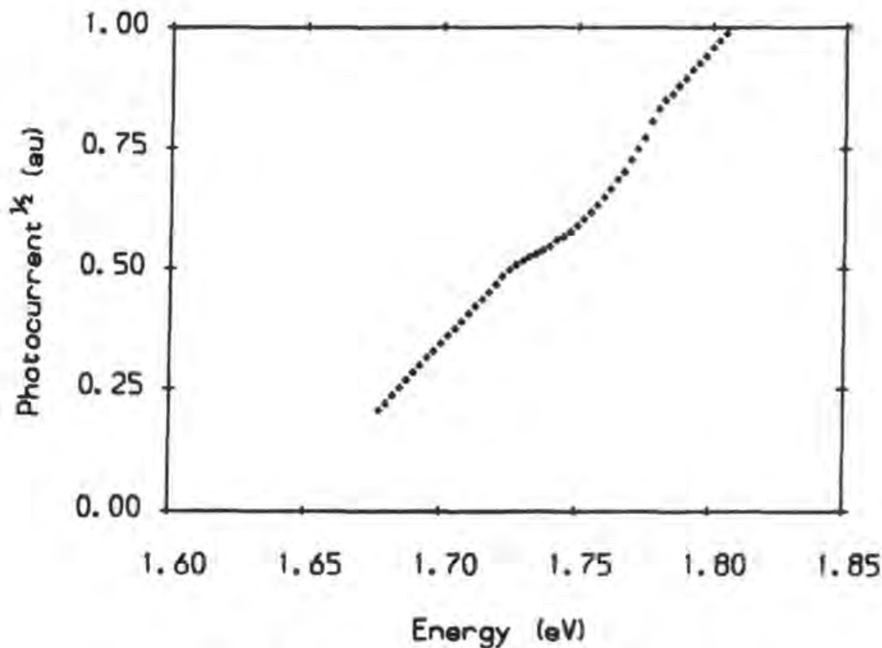

Figure 3.13 Fowler plot for a typical Au/ZnSe MS diode.

values quoted in the literature for chemically polished ZnSe devices [30]. Non-linearity in the plot at 1.75 eV was caused by a large emission peak from the lamp, which was not completely corrected for by the system.

3.4.2 Capacitance–voltage characteristics

The capacitance of the depletion region in a Schottky barrier is bias dependent since its width varies with the applied voltage. Assuming that the charge distribution in the depletion region is constant (eN_d, where N_d is the ionised donor density), and neglecting both the effect of interface states and contributions from mobile carriers at the edge of this region, the bias dependence of the depletion layer capacitance is given by:

$$C_d = \frac{\delta Q}{\delta V} = \left[\frac{e\epsilon_s N_d}{2(V_d - V)}\right]^{\frac{1}{2}} \tag{3.3}$$

where ϵ_s is the dielectric constant of the semiconductor, and V_d the diffusion potential. The uncompensated donor density is given by:

$$N_d = -2\left[e\epsilon_s \frac{\delta(\frac{1}{C^2})}{\delta V}\right]^{-1} \tag{3.4}$$

Thus if experimentally determined values of $\frac{1}{C^2}$ are plotted *vs* the bias voltage, estimates for N_d and V_d may be determined from the slope and the intercept on the voltage axis respectively. It should be noted that a true barrier height cannot be determined using this technique, since electrons do not cross the barrier as they do in conductivity measurements. However, for moderately heavily doped semiconductors, the diffusion potential and the barrier height are approximately equal [31].

In this work, capacitance–voltage (*CV*) characteristics were recorded using a 1 MHz capacitance bridge (Boonton 72B), which superimposed a small (15 mV) test signal on a DC bias. The bias voltage was derived from a computer controlled digital to analogue converter, and the output from the bridge recorded using a digital meter interfaced to the computer. Thus the *CV* characteristic could be recorded automatically, and a least squares fit to the data enabled calculation of the voltage axis intercept and carrier concentration. Figures 3.14a and 3.14b show a typical *CV* characteristic and $\frac{1}{C^2}$ plot respectively. From figure 3.14b, the diffusion potential is calculated to be $V_d = 2.00$ eV, and the uncompensated carrier concentration $N_d = 6.3 \times 10^{15}$ cm^{-3}. These results are in agreement with those found in the literature for similar ZnSe MS devices [30].

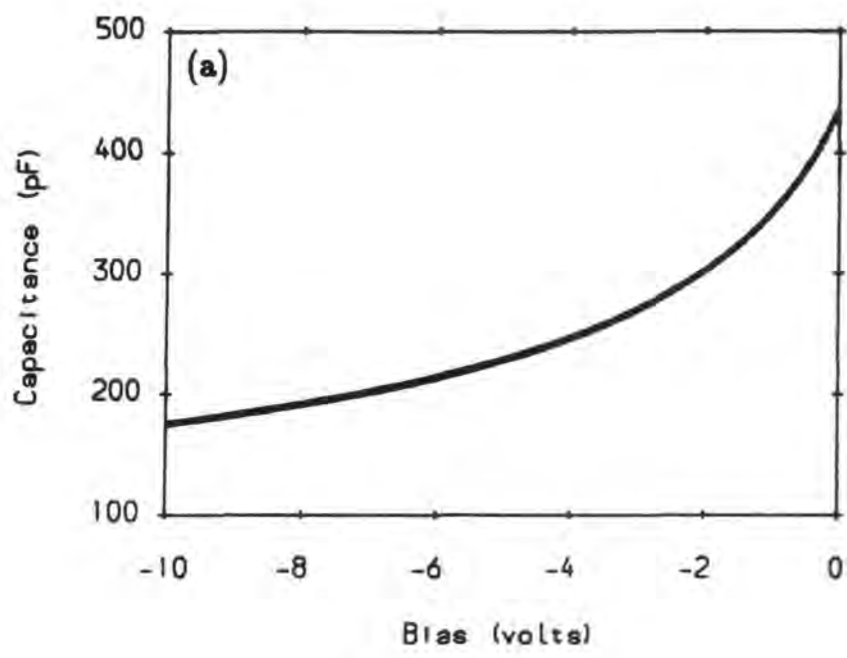

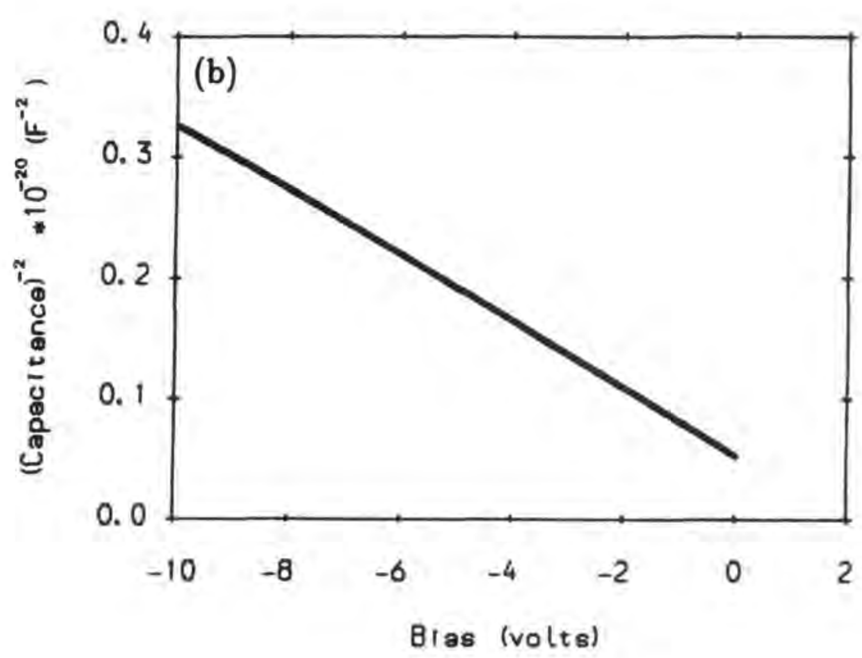

Figure 3.14 Typical plots of (a) capacitance (C) vs voltage (V), and (b) $\frac{1}{C^2}$ vs V for an Au/ZnSe diode.

3.4.3 Current–voltage characteristics

Carrier transport in a Schottky barrier can occur through a number of mechanisms:

(1) electron emission over the barrier,
(2) tunnelling through the barrier,
(3) electron hole recombination.

Of these mechanisms, item (1) is the most important in practical devices. At room temperature, and with "normal" doping levels, the barrier is too wide for there to be an appreciable tunnelling current, and as discussed in the previous chapter, the minority carrier injection ratio in an ideal MS device is negligible. Two main models have been proposed to explain the conduction process, namely diffusion theory [32] and thermionic emission [33]. Diffusion theory describes the conduction process in terms of carrier drift and diffusion, as determined by the transport equation. Thermionic emission theory neglects the effects of drift and diffusion, and it is assumed that the major influence on transport is the probability that a carrier will have sufficient energy to overcome the energy barrier. There has been some dispute as to which process is most important in determining the current–voltage characteristics of practical devices, however it is now generally accepted that thermionic emission theory provides the most accurate description [34]. This theory predicts an *IV* relationship:

$$J = J_s \left[\exp\left(\frac{eV}{kT}\right) - 1\right] \tag{3.5}$$

where:

$$J_s = A^* T^2 \exp\left(-\frac{e\phi_{bn}}{kT}\right) \tag{3.6}$$

and:

$$A^* = \frac{4\pi m_e^* e k^2}{h^3} \tag{3.7}$$

A^* is known as the Richardson constant.

For an ideal device, a plot of $\log_n(J)$ *vs* V will be linear with a intercept J_s on the current axis. Figure 3.15 shows a typical *IV* characteristic for a ZnSe MS device, which was recorded using a Time Electronics 2003S voltage calibrator and a Keithley model 602 electrometer. The plot is linear over only a small range of current, the saturation at higher current densities resulting from the series resistance of the bulk ZnSe. Abnormally high current levels at low voltages have previously been assigned to current leakage through surface layers formed during the chemical polish [30]. Extrapolation of the linear region of the plot to zero bias leads to a value for the saturation current of

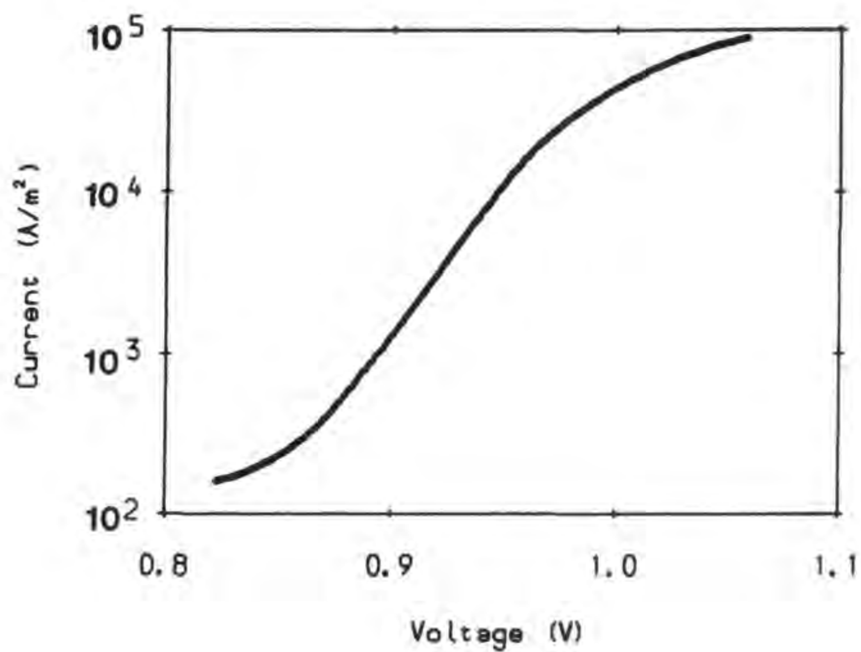

Figure 3.15 Current voltage characteristic of an Au/ZnSe diode in forward bias.

$J_s = 6.58 \times 10^{-14}$ Am^{-2}, from which a barrier height of $\phi_{bn} = 1.40$ eV may be calculated using equations 3.6 and 3.7, assuming an electron effective mass $m_e^* = 0.17\ m_e$. Again, these results correspond well with those in the literature [30].

3.5 Summary

The work described in this chapter has provided some representative characteristics of bulk single crystal II–VI compound EL devices, and forms a basis for further research with novel structures. However, some of the results are of direct interest in the present study, and warrant further discussion here.

Steady state EL measurements have shown that doping with gallium is effective in suppressing the deep centre EL emission in II–VI compound devices. This result is in accordance with the model discussed in chapter 2 which predicts the formation of inert Cu/Ga complexes. It is worth noting here that some of the most efficient blue luminescence, in highly conducting ZnSe, was obtained using material grown by liquid phase epitaxy from Zn/Ga solutions [35,36]. These results may be significant for the MOCVD growth of ZnS and ZnSe, since the most commonly used substrate for epitaxial growth is GaAs, and it has been established that gallium can diffuse into the II–VI layers from the III–V substrate [37]. Time resolved EL measurements have identified the electronic transitions responsible for the blue light emission in the present devices as free to bound and bound to bound transitions, involving sodium and lithium acceptor type impurities.

The photoelectric response of the devices indicated that the barrier energy was approximately 1.64 eV, however, the diffusion potential calculated from *CV* measurements was 2.0 eV. The disparity between these estimates of barrier energy can be attributed to the presence of an interfacial layer between the gold contact and the ZnSe, which may become as thick as 25 nm depending on the chemical etching procedure [30]. Several authors have discussed the influence of such interfacial layers on the *CV* characteristic [31,38,39], but here it is sufficient to simply note that an interfacial layer exists. The barrier height determined from *IV* measurements, $\phi_{bn} = 1.40$ eV, is lower than that determined from the photoresponse. In other words, the saturation current, $J_s = 6.58 \times 10^{-14}$ Am^{-2}, is greater than would be expected for a barrier height of $\phi_{bn} = 1.64$ eV ($J_s = 5.16 \times 10^{-18}$ Am^{-2}). The observation of an abnormally high saturation current, together with the fact that EL was recorded in forward bias, indicates that hole injection was occurring through the insulating layer [30].

In conclusion, blue LEDs were successfully prepared using bulk single crystal ZnSe. However, the luminescent characteristics of these devices were dominated by impurities, most notably copper, sodium and lithium. The most likely source of these impurities is contamination from silica and other furnace components during crystal growth and

subsequent processing. In addition to their effect on the EL spectrum, such impurities may preclude the preparation of p–n junctions, which are essential for the fabrication of more efficient devices. For these reasons it is necessary to investigate the application of alternative lower temperature growth techniques to the production of II–VI compound semiconductor EL devices.

CHAPTER FOUR

MOCVD GROWTH AND CHARACTERISATION OF EPITAXIAL ZnS/ZnSe STRUCTURES

4.1 Introduction

The metalorganic chemical vapour deposition (MOCVD) technique offers the possibility of growing thin film single crystal layers of II–VI compound semiconductors in a highly controlled manner, at a much reduced temperature in comparison with bulk growth by traditional methods. For instance, bulk single crystals of ZnSe [1] and ZnS [2] are usually grown in the vapour phase from high purity polycrystalline material at temperatures of the order of 1100 and 1500 °C respectively. Growth at these temperatures thermodynamically favours the formation of impurity, defect, or impurity–defect complexes, which can act as electron traps [3]. The control of such defects by suitable choice of growth conditions is of special importance in opto–electronic applications.

MOCVD was first applied to the growth of the zinc and cadmium sulphides, selenides and tellurides by Manasevit and Simpson [4]. Single crystal layers were grown onto insulating ceramic substrates, using the reaction between diethyl zinc or dimethyl cadmium and the group VI hydrides. A vertical reactor was employed, and the reactants were transported in hydrogen at atmospheric pressure. Following this work, a similar design of reactor was used in a study of the epitaxial growth of ZnSe [5,6]. A horizontal system [7] has also been developed for use with II–VI compounds, where the uniform gas flow over a susceptor tilted at $\sim 10°$ to the horizontal (towards the gas flow) leads to more uniform growth as the reactants are depleted from the gas stream. A variety of substrate heating methods, including resistive, radiant, and radio–frequency induction have been employed, and both types of reactor have been operated at atmospheric and reduced pressure. Growth at reduced pressure offers several advantages [8] including:

(1) A reduction in premature gas phase reactions between the source compounds.
(2) An increase in the gas flow velocity while retaining laminar flow.
(3) Reaction limited rather than transport limited growth, leading to more uniform deposition over larger areas.

However, the need for a pumping system capable of handling toxic and pyrophoric waste products has stimulated the development of growth apparatus capable of operation at atmospheric pressure [9]. Premature gas phase reactions in such a system can be significantly reduced by using compounds in which the group VI element is more tightly bound than in the corresponding hydride. For example, growth of ZnS and ZnSe at

atmospheric pressure without premature reaction has been achieved using heterocyclic compounds of sulphur and selenium (tetrahydrothiophene and selenophene respectively) in reaction with dimethyl zinc [10].

Recent work on ZnS, ZnSe, and their alloys, has been concerned with both the structural integrity of the substrate–epitaxial layer interface and the electrical and optical quality of the layers. High resolution transmission electron microscope (HRTEM) studies have shown that good lattice matching, and hence epitaxial quality, can be obtained by growing ZnS_xSe_{1-x} with $x = 0.06$ on GaAs substrates [11,12]. Furthermore, a significant reduction in gallium diffusion from the substrate was observed when the epitaxial layer was lattice matched to the GaAs. Of the wide band gap binary compounds, ZnSe has received most attention because of its potential application in light emitting devices, and its very similar lattice spacing to that of widely available GaAs substrates. Some control of the electrical properties has been achieved through doping during growth. For example, highly conducting n–type material, with $\rho < 0.05\ \Omega$ cm, was obtained by doping with aluminium from a trimethylaluminium source [13]. The p–type dopants nitrogen and phosphorous have been introduced during growth from dimethyl zinc and H_2Se, using NH_3 and PH_3 respectively [14]. Unfortunately, good p–type conductivity has not been reproducibly achieved, although evidence for the presence of acceptors has been detected in photoluminescence studies (see chapter 2).

A common figure of merit used in assessing the luminescent quality of epitaxial films is the ratio, R, of the intensity of the near band edge emission to the intensity of the deep level luminescence [15]. The value of R in MOCVD material ($R \sim 10^2$) [16] is now comparable with that of material grown by molecular beam epitaxy (MBE) [17]. MOCVD also offers the advantage of a much greater maximum growth rate ($\sim 10\ \mu$m/h for MOCVD [9] and $\sim$1–2 μm/h for MBE [18]) and thicker layers generally have better structural [18], electrical [19], and luminescent [16] properties. Recent improvements in the luminescence efficiency of MOCVD ZnSe, for which an *internal* quantum efficiency of 30% has been reported [20], indicate that this material remains an attractive prospect for the production of EL devices.

The potential for MOCVD in the production of II–VI compound EL devices has been demonstrated in a composite DCEL structure incorporating thin film ZnS:Mn and a powder based current control layer [21]. This chapter discusses the growth, and structural and electrical assessment of MOCVD ZnS and ZnSe layers for use in all thin film EL devices. The fabrication and characterisation of these devices is discussed in subsequent chapters.

4.2 MOCVD Growth

4.2.1 Growth apparatus

All of the epitaxial ZnS and ZnSe layers used in this investigation were grown using apparatus developed by P.J. Wright and B. Cockayne of the Royal Signals and Radar Establishment [9]. The apparatus is shown schematically in figure 4.1. A horizontal reactor, consisting of a water cooled silica envelope, contains a SiC coated graphite susceptor which is heated by radio frequency induction. The hydrogen used to transport the reactants, namely dimethyl zinc (DMZ), H_2S and H_2Se, is purified using a palladium diffuser. Reactant gases are controlled by pneumatically operated valves and mass flow controllers, and conveyed to the reactor through stainless steel pipe work. The DMZ bubbler is cooled to -10 °C in an alcohol/water mixture to obtain an appropriate vapour concentration. The alkyl and hydride gas streams remain separate up to the reactor inlet in order to reduce premature reaction, and a carefully designed mixer nozzle in the reactor is positioned for optimum growth on the susceptor.

4.2.2 Source and substrate materials

The basic reactions used in the growth of ZnS and ZnSe are given by equations 5.1a and 5.1b respectively:

$$(CH_3)_2Zn + H_2S \rightarrow ZnS + 2CH_4 \tag{5.1a}$$

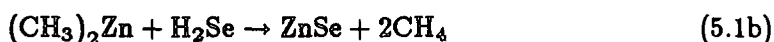

$$(CH_3)_2Zn + H_2Se \rightarrow ZnSe + 2CH_4 \tag{5.1b}$$

Although premature reactions between DMZ and the hydrides can occur (even at room temperature), these can be minimised by using low concentrations of the reactants (typical mole fractions are: 5×10^{-5} DMZ and 2×10^{-4} H_2Se). Coupled with a high flow rate of 4.5 l/min and correct positioning of the mixer nozzle, these conditions allow the reaction to occur predominantly at the susceptor. Unwanted gas phase reactions can be eliminated using heterocyclic compounds of sulphur and selenium in reaction with DMZ [10], but these sources require growth temperatures in excess of 450 °C. The ZnSe layers used in this work were grown at a substrate temperature of 275 °C, which results in a low resistivity and good structural properties [16,19]. The growth rate is determined by the flow rate of the minority reactant, which for ZnS and ZnSe is DMZ, since an excess of this component with respect to the hydride results in polycrystallinity and poor surface morphology [9].

The choice of substrate material is an important consideration for high quality epitaxial deposition. Ideally the substrate should be perfectly lattice matched to the epitaxial layer as in homoepitaxial systems. Unfortunately, single crystal II–VI

substrates are difficult to obtain and consequently members of this family of compounds are generally grown heteroepitaxially. GaAs was selected as a substrate for the present study because of its wide availability and close lattice match with ZnSe (a_{GaAs} = 5.6535 Å and a_{ZnSe} = 5.6686 Å [9]). Good epitaxial growth of ZnSe and ZnS was obtained on the {100} plane, despite considerable lattice mismatch in the latter system (a_{ZnS}=5.4093 Å [9]).

4.2.3 Growth of structures for device applications

Figure 4.2 shows the different structures which were required for the fabrication of (a) ZnSe MS and (b) ZnS/ZnSe MIS EL devices. The III–V layers shown in figure 4.2c, which formed an etch stop when processing an alternative MIS structure, were deposited using a separate growth system. GaAs {100} orientated substrates were supplied as slices cut from single crystals grown by the Czochralski technique, and polished using standard mechanical and chemical techniques to a mirror finish. Prior to growth, the substrates were degreased in boiling propan–2–ol and blown dry in filtered nitrogen before etching in a 5:1:1 solution of H_2SO_4:H_2O_2:H_2O for 20 min at 40 °C. Substrates were then rinsed in deionised water and blown dry from boiling propan–2–ol, before loading into the MOCVD reactor. The system was flushed with purified hydrogen for 15 min prior to a 10 min bake out at 500 °C. The temperature was then reduced to 275 °C and the reactants admitted to the growth chamber. With flow rates of 5 cc/min and 40 cc/min for DMZ and H_2Se respectively, 3–4 μm of ZnSe were deposited in 1 h, and a ZnS I–layer 0.2 μm thick was deposited in 2–3 min with an H_2S flow rate of 80 cc/min. When growing ZnS/ZnSe structures, the reactor was flushed with hydrogen for 2 min after growth of the ZnS layer in order to expel any residual H_2S. This procedure avoided growth of the alloy ZnS_xSe_{1-x} when the H_2Se was first admitted, and thus allowed the production of a sharp ZnS/ZnSe interface. On completion of the growth run, the sample was allowed to cool naturally under flowing hydrogen. Figure 4.3 shows SEM micrographs of cross sections obtained by cleaving some typical multi–layer structures grown on GaAs substrates.

4.3 Structural assessment

4.3.1 X–ray diffraction

X–ray diffraction profiles were recorded (using cobalt Kα radiation) from the as–grown (100) surface of the epitaxial layers. With this orientation the only planes able to satisfy the Bragg condition, $2d\sin\theta = n\lambda$ (where d=inter–planer spacing, θ=diffraction angle, λ=wavelength and n is an integer corresponding to the order of diffraction), are those belonging to the (h00) family (h=integer). Furthermore, structure factor effects impose the additional requirement that h must be even. Since $\frac{\delta\theta}{\delta\lambda}$ increases with

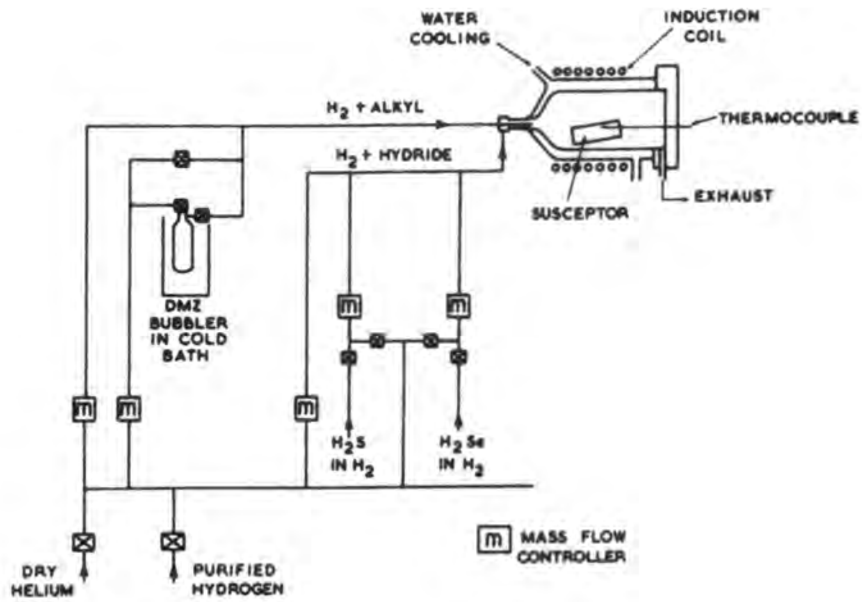

Figure 4.1 Horisontal reactor MOCVD growth system (ref. [9]).

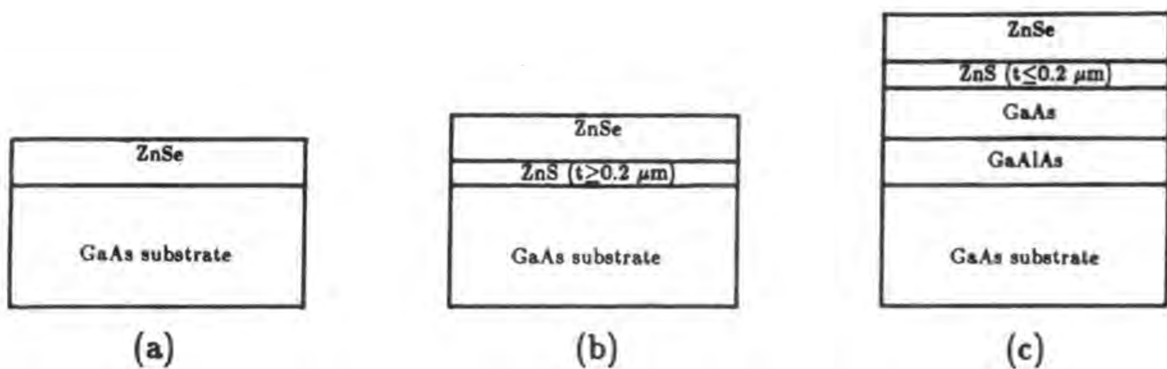

Figure 4.2 Structures used in the fabrication of (a) ZnSe MS, (b) and (c) ZnS/ZnSe MIS devices.

diffraction angle, profiles were recorded using relatively high angle reflections so that the cobalt $K\alpha_1/\alpha_2$ doublet would be resolved, thus simplifying identification of the diffraction peaks. Figure 4.4 shows an X-ray diffractometer scan of the (400) peak from a ZnS(0.2 μm)/ZnSe(3 μm) structure. The well resolved narrow peaks for both the substrate and ZnSe layer are indicative of good epitaxial growth. Analysis of X-ray rocking curves for MOCVD grown ZnSe on GaAs indicates that the layers undergo tetragonal distortion [22]. The strain may be taken up elastically [23] or relieved by the creation of dislocations [22].

4.3.2 Surface morphology

With the growth conditions described above it was possible to deposit specular quality ZnS and ZnSe on {100} GaAs substrates, although thicker layers had a hazy appearance, which became more pronounced with higher growth rates. Figure 4.5 shows SEM micrographs taken from the as-grown surface of (a) ZnS of thickness 0.2 μm, (b) a ZnS/ZnSe structure with layer thicknesses of 0.2 μm and 4 μm respectively, and (c) ZnSe of thickness 8 μm. The ZnS layer has a fairly uniform surface, the major feature being a slight "orange peel" texture, however, the surface morphology of the ZnSe layers is dominated by ridge shaped features. These are most pronounced in the ZnSe layer shown in figure 4.5c, which is twice as thick and was grown at twice the rate of that in figure 4.5b. Reflection high energy electron diffraction (RHEED) and SEM studies confirmed that the ridges always ran parallel to just one {110} direction. These observations are in accordance with previous findings, which were interpreted in terms of crystallographic non-equivalence of the two perpendicular (110) and ($\bar{1}$10) cleavage planes [24] (see section 4.3.4).

Although the growth ridges ran over most of the wafer, a different morphology was observed at the edges. Figure 4.6a shows a micrograph taken from the edge of the sample shown in figure 4.5c. The ridges are visible to the right of the micrograph, but the extreme edge of the layer is characterised by isolated regions of highly faceted material. Approximately 40 μm in from this edge, the ZnSe surface is more uniform, and there is a sharp boundary between this region and the ridges which characterise the rest of the wafer. This sample was grown at approximately twice the "normal" rate by doubling the DMZ flow, and an energy dispersive X-ray map obtained using the Zn($K\alpha$) line (figure 4.6b) shows a high concentration of zinc at the edge of the sample. Figure 4.6c shows similar growth features at the edge of a ZnSe layer which was grown with the "normal" DMZ flow rate. In this case energy dispersive X-ray spectra clearly indicated an increased selenium concentration at the edge of the substrate, although differences in elemental concentrations were not large enough to record an X-ray map. These growth features may be a result of preferential deposition on the susceptor, leading to a localised depletion of reactants in the carrier gas.

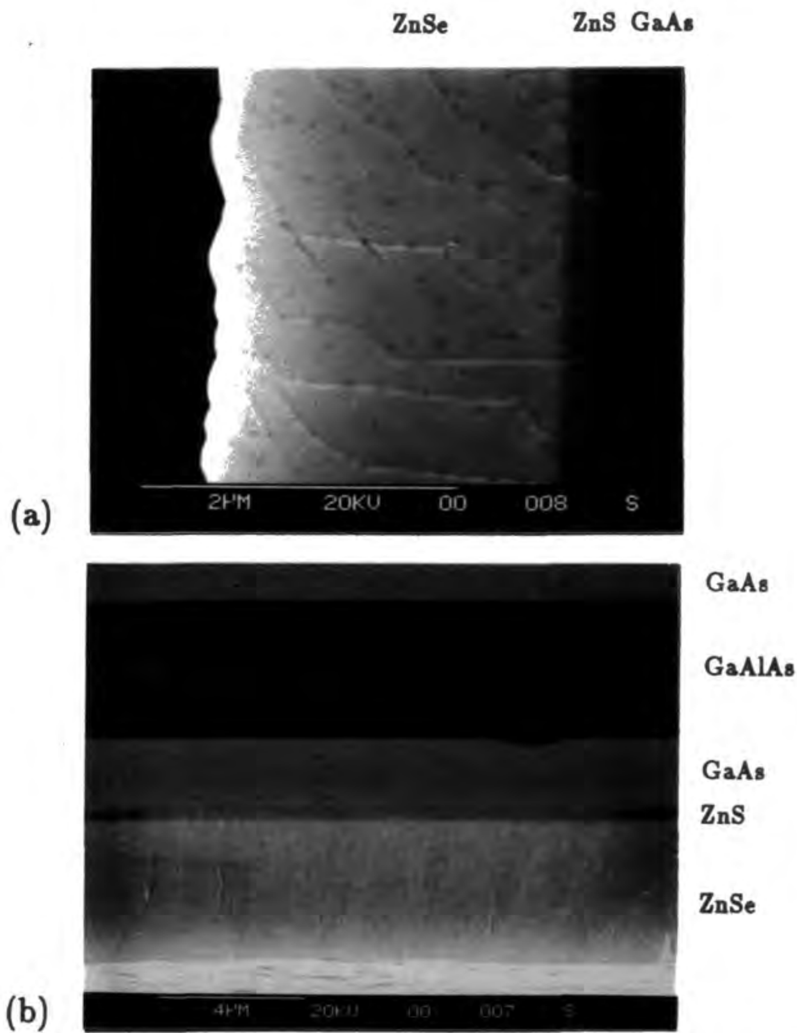

Figure 4.3 Cross sections obtained by cleaving multi–layer structures grown on GaAs substrates: (a) GaAs/ZnS/ZnSe, (b) GaAs/GaAlAs/GaAs/ZnS/ZnSe.

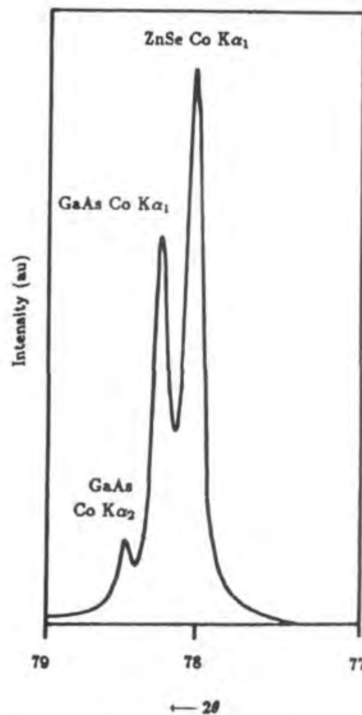

Figure 4.4 X–ray diffraction peaks for the (400) reflection from a ZnS/ZnSe epitaxial structure on (100) orientated GaAs.

(a)

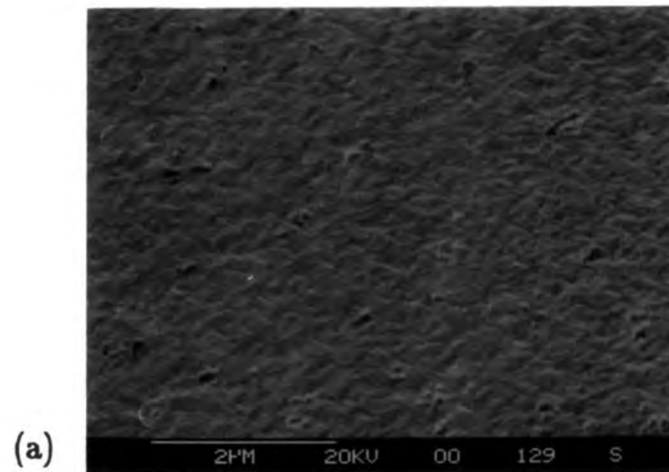

(b)

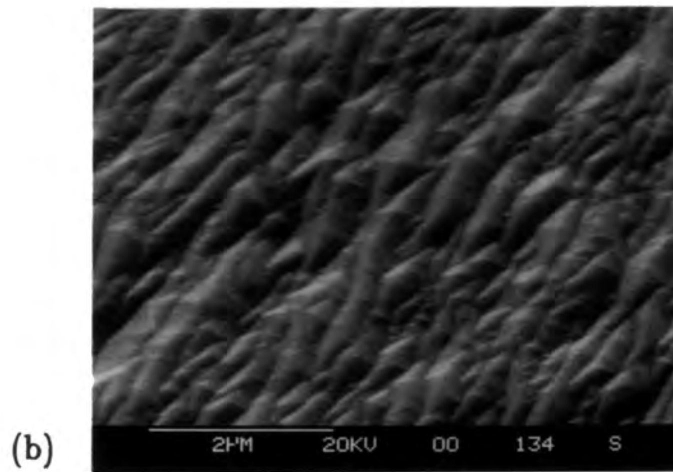

(c)

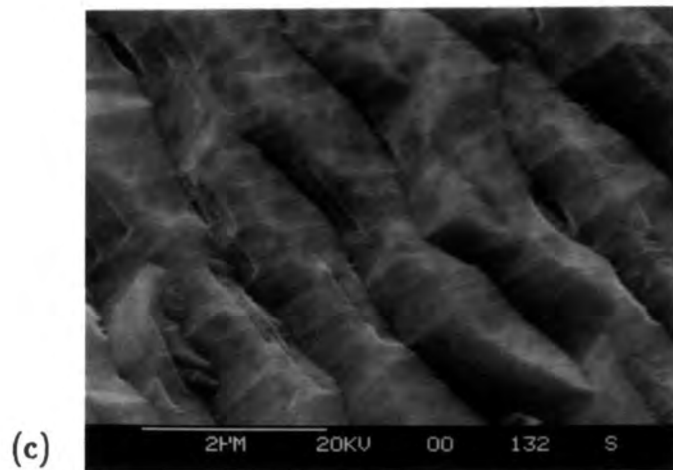

Figure 4.5 The surface morphology of epitaxial layers grown on GaAs substrates: (a) ZnS (0.2 μm), (b) ZnS/ZnSe (0.2 μm/4.0 μm) and (c) ZnSe (8.0 μm).

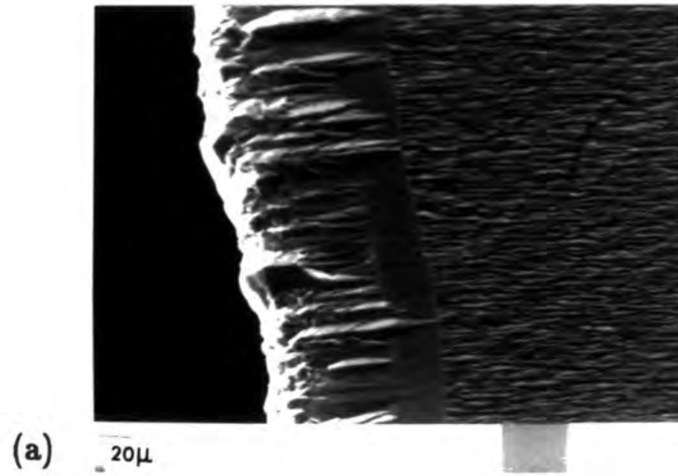

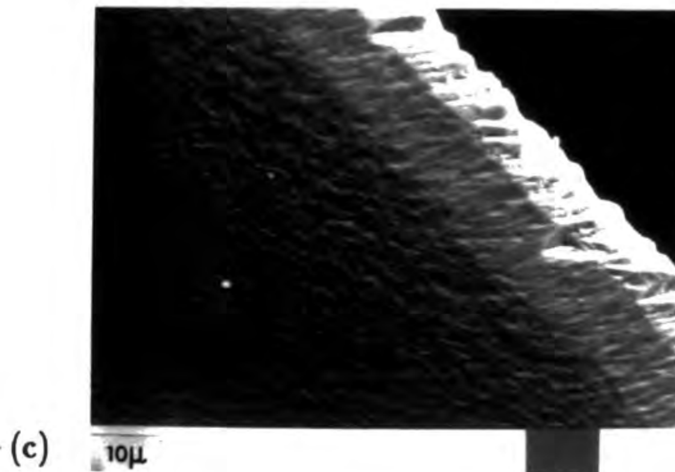

Figure 4.6 Growth features at the substrate edge: (a) ZnSe (8.0 μm) grown with a "high" DMZ flow rate, (b) X-ray map for sinc taken from the same area, (c) ZnSe (3.0 μm) grown at the "normal" DMZ flow rate.

4.3.3 RHEED investigations

The structural quality of as–grown layers was investigated routinely using RHEED in a JEM 120 transmission electron microscope operated at 100 kV. RHEED patterns typical of those recorded with the beam incident along a <110> direction in the cubic structure for a range of samples are shown in figure 4.7. In general, distinct spot patterns with no arcing provided a clear indication of the excellent epitaxial quality of the II–VI layers deposited by MOCVD. However figure 4.7a, which was taken from a single layer of ZnSe on GaAs, shows diffraction streaks passing through the matrix reflections in two directions inclined at $\sim 35°$ to the shadow edge of the sample. This observation would be consistent with the presence of thin planar defects lying on the $\{111\}$ planes which are inclined at $54° \, 44'$ to the interface. These defects might arise from the lattice mismatch between the GaAs substrate and the ZnSe epitaxial layer. Figure 4.7b, taken from a GaAs/ZnS/ZnSe structure with the beam incident along the [110] direction, shows similar diffraction streaks, but in this case additional diffraction spots are observed at positions displaced from the matrix reflections by $\frac{1}{3}$ the distance between them. These spots reveal the presence of microtwins lying on both of the two $\{111\}$ planes parallel to the incident beam. Figure 4.7c shows a RHEED pattern from the same sample after a rotation of 90° about the substrate normal, that is with the beam incident along the $[\bar{1}10]$ direction. With this orientation, diffraction spots arising from microtwins are not present, thus indicating an absence of stacking disorder on the $\{111\}$ planes now parallel to the beam. The observation of twins on the $\{111\}$ diffracting planes in figure 7b, and their absence on the other pair of $\{111\}$ diffracting planes in figure 7c, is related to the polar properties of the zincblende structure (see section 4.3.4). Finally, figure 4.7d shows a typical RHEED pattern recorded from a ZnS/ZnSe structure incorporating III–V buffer layers, which incidentally provided a higher quality substrate for epitaxial growth. The presence of Kikuchi bands in this diffraction pattern provides further evidence for the excellent structural quality of the II–VI layers.

4.3.4 Cross sectional TEM studies [1]

The observation of growth ridges lying in only one <110> direction (figure 4.5), and the non–equivalence of perpendicular $\{110\}$ planes revealed by RHEED, instigated a cross sectional transmission electron microscope (XTEM) investigation into the anisotropy of the defect distribution in ZnS and ZnSe epitaxial layers [25]. Although there have been several previous high resolution TEM studies of epitaxial ZnSe [26,27,28,29], ZnS [30], and $ZnSe_{0.94}S_{0.06}$ [11,12], only one of these has addressed the problem of in–plane anisotropy of the defect concentration [26]. The aim of the present work is to redress this omission by highlighting the contrasting defect structure in epi-

[1] Experimental investigation by P.D. Brown of this department.

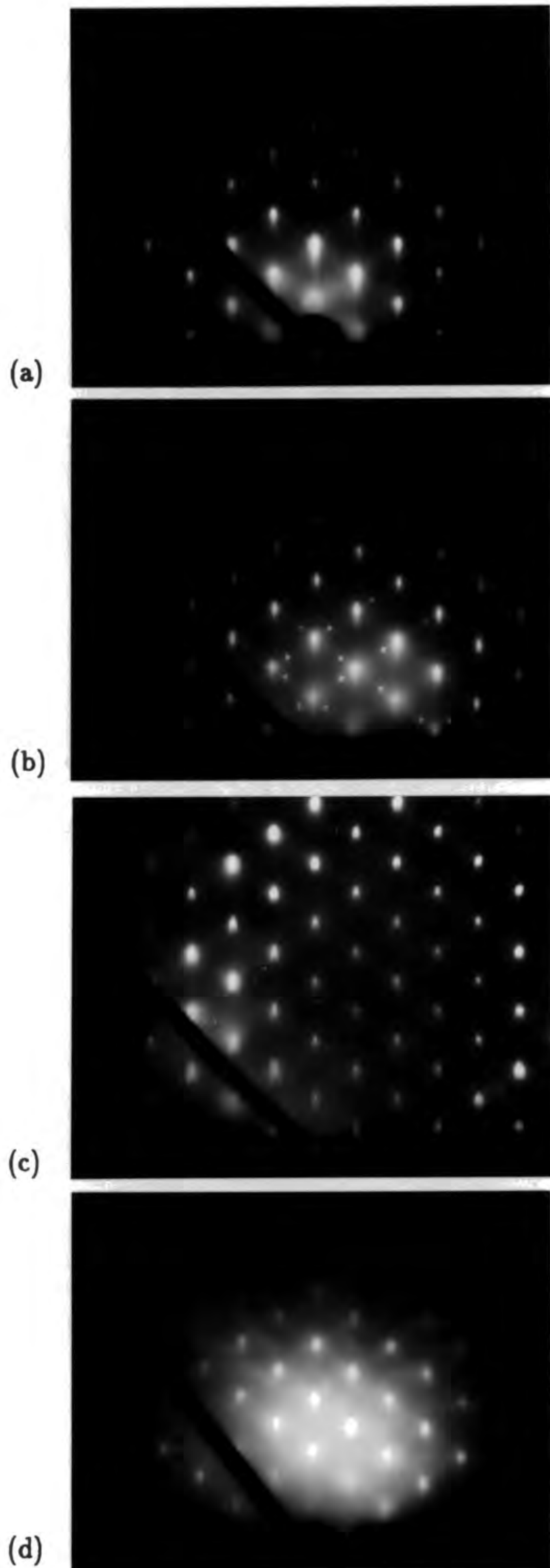

Figure 4.7 100 kV <110> zone axis RHEED patterns recorded from the as–grown surface of: (a) GaAs/ZnSe, (b) GaAs/ZnS/ZnSe (beam along [110]), (c) GaAs/ZnS/ZnSe (beam along [$\bar{1}$10]), and (d) GaAs/GaAlAs/GaAs/ZnS/ZnSe structures.

taxial layers of ZnS/ZnSe on (100) GaAs when observations are made along orthogonal <110> directions for the same samples. Specimens were prepared for observation in the TEM by bonding epilayer/GaAs slices face to face using epoxy resin. These slices were cleaved along orthogonal {110} planes lying mutually perpendicular to the specimen surface. After mechanical polishing, the composite samples were thinned using the reactive iodine ion sputtering technique [31], and TEM observations were made using a JEOL 100CX microscope operated at 100 kV. Observation of the electron transparent regions on either side of the glue line in the microscope corresponded to the projection of the two orthogonal <110> zone axes, thus allowing comparison of the defect structures in cross sections prepared from (110) and $(1\bar{1}0)$ slices.

A range of GaAs/ZnS/ZnSe samples, with ZnS I–layer thicknesses in the range 0.2 to 0.9 μm, were investigated. The defect structures observed in the orthogonal <110> directions for a sample with a 0.9 μm thick ZnS layer are illustrated in figures 4.8a and 4.8b. Selected area diffraction patterns recorded from the region shown in figure 4.8a confirmed that the planar defects were microtwins. These micrographs are typical of all the samples examined, and demonstrate that the different types of defect which predominate in the different <110> orientations of the ZnS are propagated across the ZnS/ZnSe interface into the ZnSe epilayer. The different defect structures in the [110] and $[\bar{1}10]$ orientations are consistent with the RHEED patterns recorded with the beam incident along [110] and $[\bar{1}10]$. Both the RHEED and XTEM studies reveal the preferential formation of microtwins on either the $\{111\}A$ or $\{\bar{1}\bar{1}\bar{1}\}B$ families of planes. Previous authors have used the different etching characteristics of the A and B planes to show that the microtwins lie on the $\{\bar{1}\bar{1}\bar{1}\}B$ (selenium) planes in the zincblende structure [32]. The origin of this anisotropic defect content is not clear, although studies of the III–V group semiconductors with the same crystal structure show that partial dislocations on the B planes are able to propagate at 100 times the speed of those on the A planes [33]. Since the formation of microtwins involves the creation of partial dislocations, the relative ease of their motion on the B planes may explain the higher incidence of microtwins on these faces.

The XTEM study also enabled the angle made by the surface growth ridges (figure 4.5) to the interface to be determined. Several measurements were made, and the angle was found to be $18^\circ \pm 4^\circ$. Comparing this measured angle with the expected intersection angles for low order crystal planes, the most probable assignment for the surface of the growth ridges is <411>. Again this result is in accordance with observations in the III–V semiconductors, which were interpreted in terms of the free energy of the growth face [34].

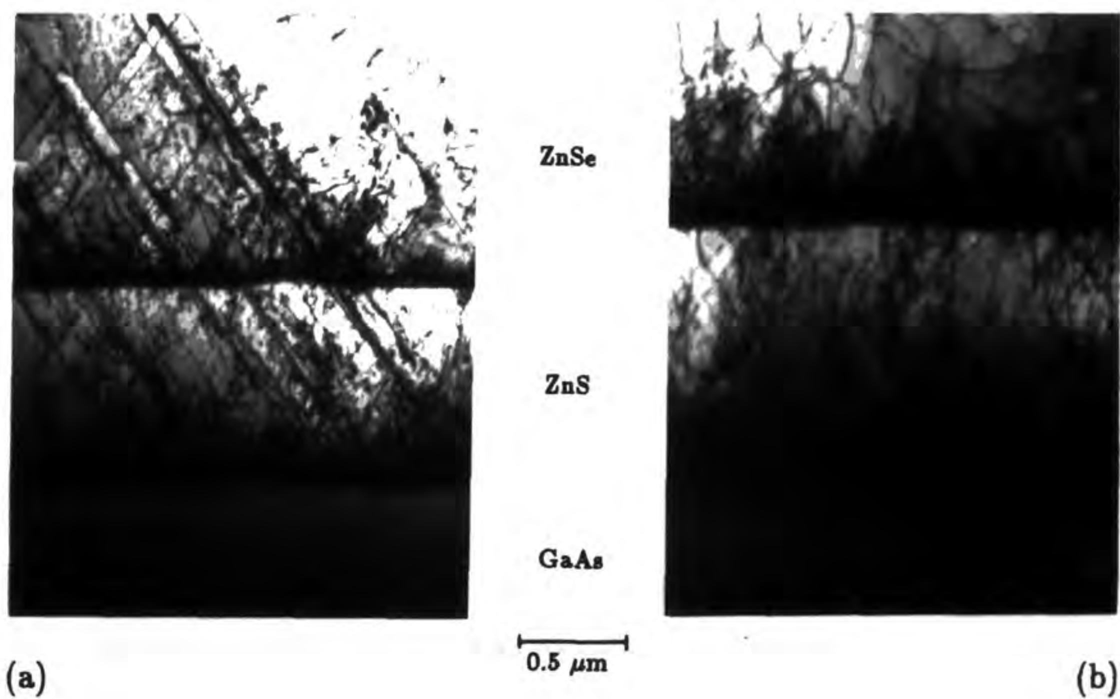

Figure 4.8 XTEM micrographs of ZnS/ZnSe on (001) GaAs observed along (a) [110] and (b) [1$\bar{1}$0].

It is difficult to relate the defect content of the layers to the optoelectronic properties of devices. However, it is likely that such high densities of defects will act as scattering centres for charge carriers [24], and so reduce the device efficiency [30]. One significant result for the work discussed later in this thesis is that the defect structure appears to be independent of the ZnS I–layer thickness.

4.4 Electrical assessment

MOCVD grown ZnSe was characterised electrically using mercury probe capacitance voltage (CV) profiling and Hall measurements. CV profiling is a rapid and non-destructive method of recording the doping profile in semiconductors. The uncompensated carrier density is found from differential capacitance measurements (equation 3.4), and a profile determined using the simple expression for the width (w) of the depletion region: $w = \frac{\epsilon}{C_d}$ [35,36]. This analysis is based on the depletion layer approximation for a Schottky barrier, and the assumption of a zero Debye length can introduce significant errors if the doping profile has large gradients [36]. Figures 4.9a and b show the $\frac{1}{C^2}$ *vs* V characteristics and the corresponding carrier concentration profile of a ZnSe layer. The carrier profile is uniform throughout the depth range (which was limited by the bias available on the apparatus), and the average uncompensated carrier concentration is $N_d = 2.9 \times 10^{16}$ cm^{-3}. Hall measurements on the same sample gave the following results at room temperature: carrier concentration $N_d = 3.8 \times 10^{16}$ cm^{-3}, resistivity $\rho = 0.70\ \Omega$ cm, and mobility μ =227 cm^2 V^{-1} s^{-1}. These results are similar to those reported by other workers (see for example [22]), but unfortunately some samples had uncompensated carrier concentrations of the order of 10^{18} cm^{-3}. The carrier concentration was dependent on the DMZ source used, and this may have been a result of contamination with gallium, which is difficult to eliminate since its chemistry is very similar to that of zinc. Contamination with high concentrations of gallium has unfortunate implications for the luminescent properties of ZnSe, which are discussed in the following chapter.

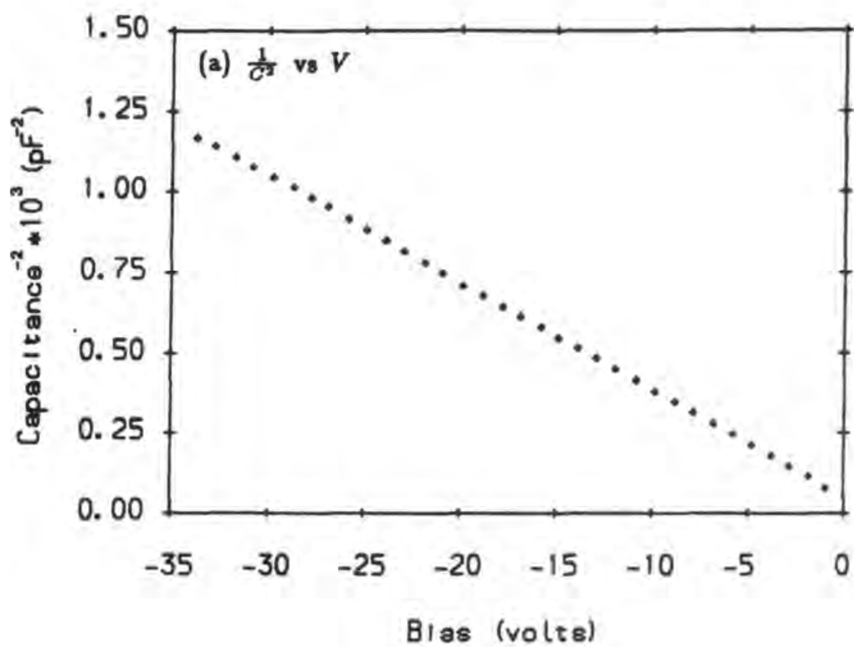

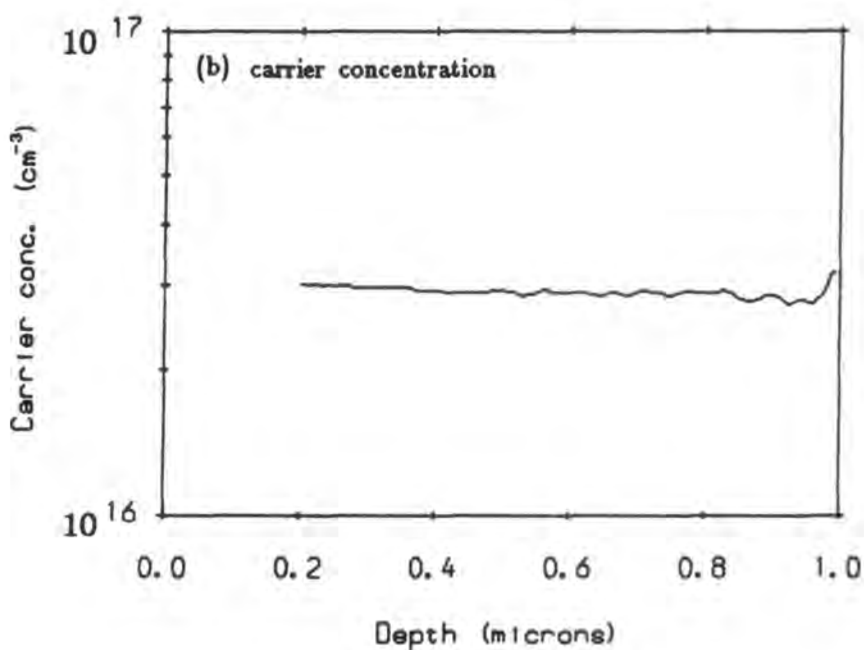

Figure 4.9 (a) $\frac{1}{C^2}$ vs V and (b) the corresponding carrier concentration profile of an MOCVD grown layer of ZnSe.

CHAPTER FIVE

EPITAXIAL THIN FILM ZnS/ZnSe INJECTION DEVICES

5.1 Introduction

In this chapter, the fabrication and characterisation of minority carrier injection EL devices using MOCVD grown ZnS and ZnSe are described. Although it was possible to fabricate simple devices on the as-grown surface of the II–VI layers, their efficiency was limited by the electrical and optical properties of the GaAs substrate. For this reason a novel device geometry was developed in order to investigate the electrical and optical properties of the epitaxial II–VI layers in the absence of any influence from the substrate material. The fabrication process involved the use of III–V buffer layers and a sequential etching procedure firstly to remove the GaAs substrate, and then etch through the remaining II–VI layers to electrical contacts previously deposited by thermal evaporation. The structural and electrical characteristics of the epitaxial devices were investigated using X-ray diffraction and RHEED, and comparisons were made with an alternative device structure which incorporated a polycrystalline I–layer. Further comparisons were made in an electron beam induced current (EBIC) study, which allowed the spatial distribution of current flow in devices with both polycrystalline and epitaxial I–layers to be recorded.

5.2 Metal–semiconductor devices

The simple MS device geometry used for the initial assessment of MOCVD grown ZnSe is shown in figure 5.1. A gold Schottky contact, 1.5 mm in diameter, was deposited by thermal evaporation onto the as-grown ZnSe at a pressure of 10^{-6} torr, and an ohmic contact made by pressing a small pellet of indium onto the ZnSe surface, and heating the device to 220 °C for 2 minutes in an argon atmosphere. The MS device provided a rapid means of assessing the EL properties of MOCVD grown ZnSe. However, it was only possible to observe EL around the edges of the gold contact. Furthermore, MS EL devices are inherently inefficient (chapter 2), and it was not possible to extend the simple geometry to the production of MIS devices.

Although a ZnS I–layer could be deposited over the ZnSe during the same growth run, it was then impossible to make ohmic contacts directly to the ZnSe. Selective chemical etching of the I–layer to expose the ZnSe underneath was impracticable since the ZnS was considerably more resistant to the etch than the ZnSe, which was attacked very rapidly once exposed. An alternative approach would have been to use a highly conducting substrate in a GaAs/ZnSe/ZnS/Au series structure, with an ohmic con-

tact to the GaAs. However, this configuration would have introduced an undesirable electronic barrier at the GaAs/ZnSe interface, and because GaAs is opaque to visible radiation, it would still only have been possible to record EL emission at the edge of the contact. For these reasons an alternative MIS structure was developed, where chemical removal of the GaAs substrate allowed electrical contacts to be made directly to the II–VI layers, in a configuration which enabled EL emission to be observed over the entire electrode area.

5.3 Fabrication of metal–insulator–semiconductor devices

5.3.1 Epitaxial MIS devices

MIS devices were fabricated [1] using the structure shown in figure 4.2b. The ZnSe layer was typically 3–4 μm thick, while, for reasons which are discussed later in this chapter, the ZnS I–layer thickness was limited to a range of roughly 0.2–1.0 μm. An ohmic contact was made to the ZnSe using indium as described above, and the device mounted securely on a clean glass slide using epoxy resin, with a gold wire contact to the indium passing through an aperture in the glass. The complete assembly was immersed in a solution containing 95% H_2O_2 (100 volumes) and 5% NH_3 (35% solution) [2], at a temperature of 25 °C. This etch dissolved the GaAs substrate but did not attack the ZnS, which served a dual purpose as an etch stop and a device I–layer. The substrate was dissolved in 1–2 hours, and when dissolution was judged (by eye) to be complete, the device was immersed in a fresh solution for a further 5 minutes to ensure that the GaAs was completely removed. After washing in deionised water and drying with a jet of filtered nitrogen, the device was mounted in an evaporator, and two 1.5 mm diameter gold contacts evaporated at 10^{-6} torr. The final device geometry is shown in figure 5.2.

The procedure described above allowed the problems associated with the simple MS device geometry to be overcome, but two important limitations arose. Firstly, it was found that structures where the thickness of the I–layer exceeded $\sim$ 1 μm tended to crack during removal of the GaAs substrate. Figure 5.3 shows typical cracks in such a structure, which run along just one edge of the two orthogonal <110> directions in the plane of the layers, consistent with the direction of the growth ridges discussed in section 4.3.2. These cracks are associated with residual strain in the ZnS layer, and in figure 5.3b it is possible to distinguish between what appear to be "mechanical" cracks and subsequent chemical attack. Fortunately, such cracking only occurred in structures where the ZnS layer thickness exceeded $\sim$ 1 μm, which was considerably greater than the optimum for a minority carrier injection device. For the purpose of the present investigation, a second and more serious problem arose because the ZnS layer remained exposed to the H_2O_2/NH_3 solution for several minutes while the substrate was removed. During this time the ZnS was susceptible to chemical attack

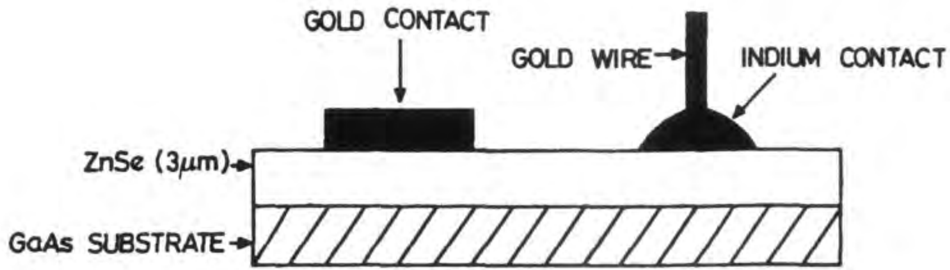

Figure 5.1 Epitaxial ZnSe MS EL device with GaAs substrate.

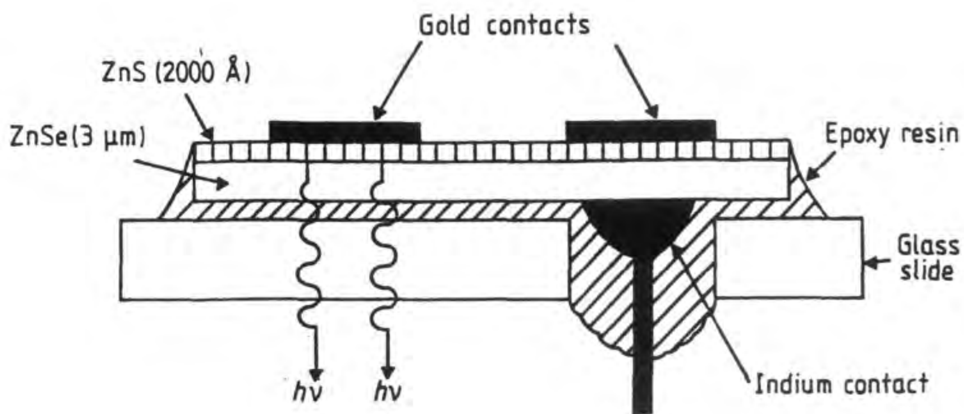

Figure 5.2 ZnSe MIS device with epitaxial ZnS I-layer.

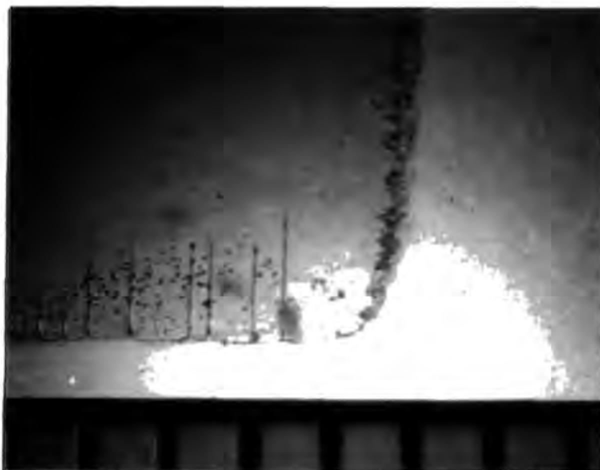

(a)

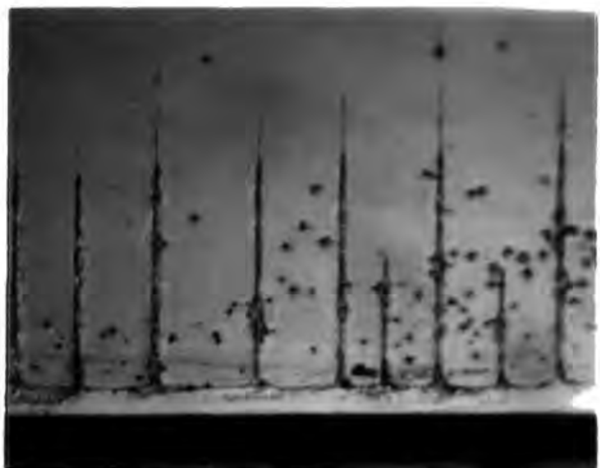

(b)

Figure 5.3 (a) Uniaxial cracking along [110] and (b) subsequent chemical attack of a ZnS I-layer during chemical removal of the GaAs substrate (mm scale).

by the etch, and once perforated, the ZnSe underneath was dissolved very rapidly. For this reason it was not possible to reduce the I–layer thickness below the 0.2–0.3 μm required for an efficient chemi–stop. Unfortunately, this thickness was greater than the optimum required for efficient minority carrier injection [3]. Figure 5.4 shows SEM micrographs of typical etch damage caused during exposure of a 0.2 μm thick ZnS I–layer to the H_2O_2/NH_3 solution for a few minutes. The attack always followed the same pattern, starting with perforation of the I–layer as shown in the secondary electron SEM image in figure 5.4a. The region behind the perforation in this micrograph is darker than the surrounding area, indicating that there was less material to contribute to the secondary electron signal, and by implication, that the ZnSe underneath the ZnS layer had been preferentially dissolved. Figure 5.4b shows a micrograph of the same area which was recorded using a lower electron accelerating potential. By using lower energy primary electrons the image is made more surface specific, and the image intensity is now uniform over the entire sample. Taken together, figures 5.4a and b show that the ZnSe underneath the I–layer was dissolved preferentially once the ZnS layer was perforated. Subsequent attack led to the rapid destruction of the device, as shown in figures 5.4c and d. It is interesting to note that this chemical attack also occurred preferentially in one of the two orthogonal <110> directions in the plane of the layers. The severe damage to both the ZnS and ZnSe layers shown in figure 5.4d obviously precluded the fabrication of devices with I–layers less than 0.2 μm in thickness, and an alternative etching procedure was developed in order to overcome this limitation.

5.3.2 MIS structures incorporating III–V compound buffer layers

Chemical removal of the substrate using the etching procedure discussed above was non–uniform, and as a consequence, the first areas of the ZnS layer to be exposed remained in contact with the H_2O_2/NH_3 solution for several minutes while the remaining GaAs was dissolved. Problems associated with subsequent chemical attack of the I–layer were overcome by using III–V compound chemi–stop layers (figure 4.2c), which enabled selective etching up to a very thin layer of GaAs over the ZnS [4]. Chemical removal of this thin GaAs layer was very rapid, and therefore the first areas of ZnS to be exposed only remained in contact with the H_2O_2/NH_3 solution for a few seconds.

The first stage of device production was the growth by MOCVD of the III–V epitaxial layers to enable the GaAs substrate to be selectively removed at a later stage. The substrates were baked out at 850 °C for 20 minutes under an AsH_3 atmosphere (which inhibited the loss of arsenic from the GaAs), and the layers were then grown at 700 °C. The first layer grown was a 2 μm thick layer of $Ga_{1-x}Al_xAs$ with x greater than 0.6, which was followed by a capping layer of GaAs approximately 1 μm thick. The substrates were then transferred to a second MOCVD reactor for the deposition of the II–VI layers, and following a bake out at 500 °C, the ZnS I–layer and a 3–4 μm

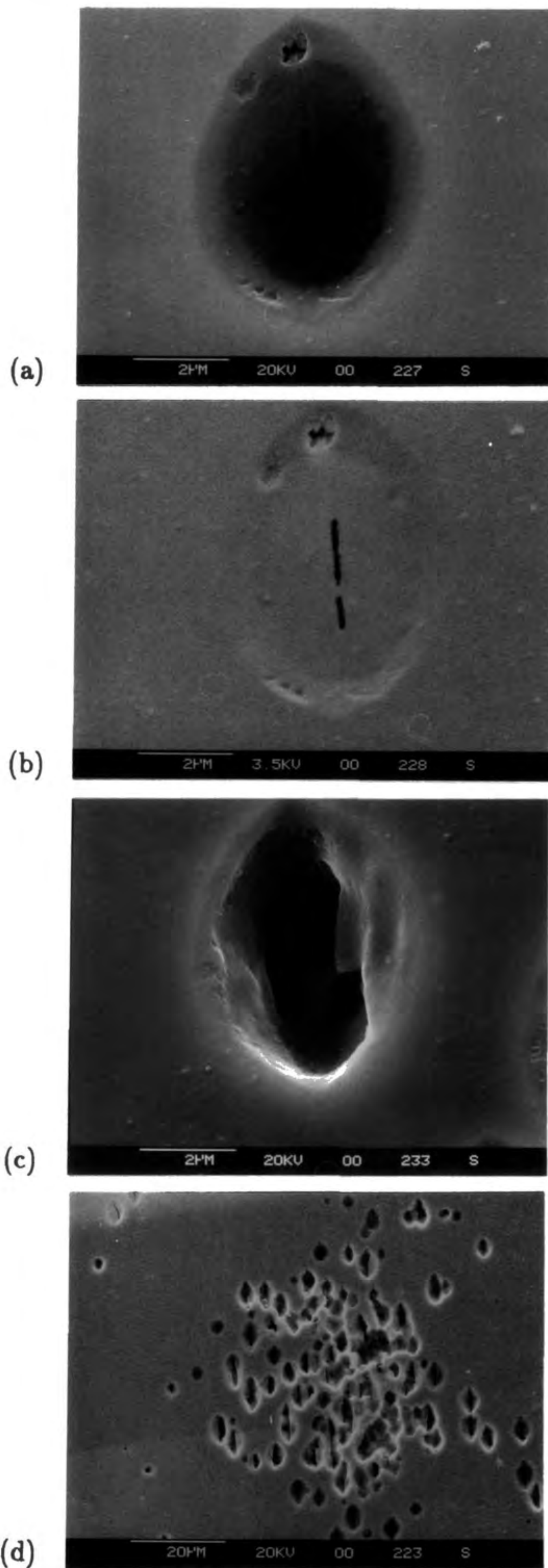

Figure 5.4 SEM micrographs showing: (a),(b) perforation of the ZnS I–layer (electron accelerating voltages 20 kV and 3.5 kV respectively), (c) subsequent attack of the ZnSe underneath the I–layer by the H_2O_2 etch, and (d) the preferred [110] orientation of the attack.

thick ZnSe layer were deposited at 275 °C. Several such structures were grown under identical conditions, while the thickness of the ZnS I–layer was varied in the range 50–200 nm.

Ohmic contacts were deposited onto the as–grown ZnSe by sequential thermal evaporations of aluminum and indium films with thicknesses of 100 nm and 200 nm respectively. The structure was then mounted on a glass slide with transparent epoxy resin, as shown in figure 5.5a, in order to protect the contacts and to provide support for the epitaxial layers after substrate removal. A solution of 95% H_2O_2 (100 volumes) and 5% NH_3 (35% solution) removed the GaAs substrate in 1–2 hours, but was stopped at the GaAlAs layer due to the formation of a protective film of aluminum oxide [2]. This oxide film and the GaAlAs layer were subsequently etched in a 15% solution of HF. The GaAs layer exposed by this etch dissolved more slowly than the GaAlAs, and developed a very smooth chemically polished surface, which provided a clear indication of the complete removal of the GaAlAs layer. Since the remaining GaAs layer was extremely thin and dissolved uniformly in the H_2O_2/NH_3 solution, the first areas of ZnS to be revealed were only exposed to the solution for a few seconds. The control afforded by the use of chemi–stop layers allowed the thickness of the ZnS I–layer to be reduced to 50 nm, and the exposed surface was extremely smooth, with no visible evidence of cracks or other defects. A gold contact of diameter 1.5 mm was evaporated onto the ZnS and protected with epoxy resin as shown in figure 5.5b. In order to make ohmic contacts directly to the ZnSe, the ZnS over the aluminium layer was removed by a chemical polish composed of 35% phosphoric acid saturated with CrO_3, and 65% HCl [5]. This polish removed the ZnS within a few seconds and allowed subsequent uniform removal of the ZnSe in concentrated HNO_3 which dissolved the ZnSe, but passivated and hence did not attack the aluminum. The exposed aluminum allowed electrical connections to be made to the ZnSe via the indium contacts on the underside of the device, as shown in figure 5.5b.

5.3.3 Thin film MIS devices with polycrystalline I–layers

MIS devices incorporating MOCVD grown single crystal ZnSe and a polycrystalline I–layer were prepared for comparison with the epitaxial devices described above. The same GaAs/ZnS/ZnSe structure was employed for consistency, although the MOCVD grown epitaxial ZnS layer did not form an active component of the device. An I–layer was deposited onto the as–grown ZnSe surface by electron beam evaporation of ZnS granules. The thickness (~0.1–0.2 μm) and rate of deposition (~ 0.1 nm/s) of this film was measured using a quartz crystal monitor. Indium and gold electrodes were formed in the same way as for the epitaxial devices. The device geometry is shown in figure 5.6.

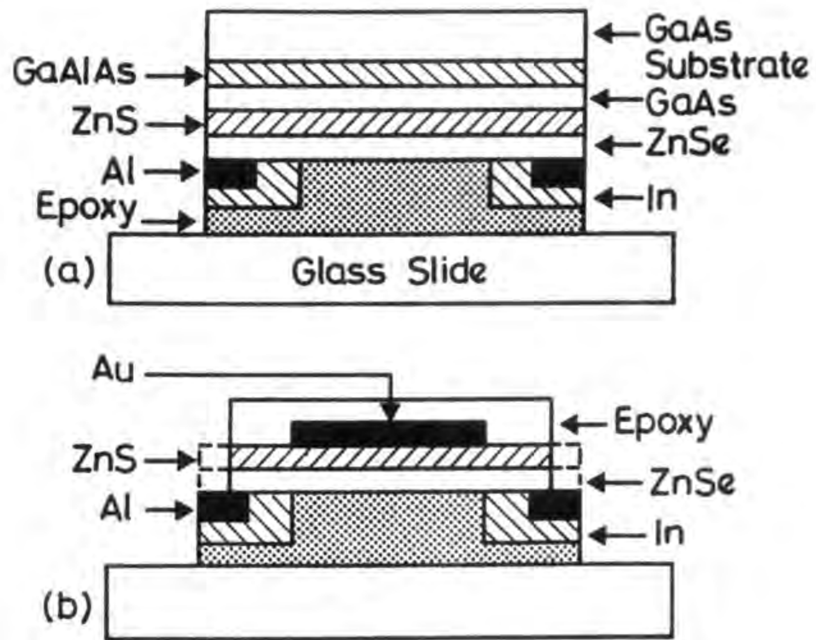

Figure 5.5 Fabrication sequence for an epitaxial ZnS/ZnSe device using III–V compound buffer layers (a) as–grown structure, (b) final device geometry (dotted region indicates structure prior to final etch to expose ohmic contacts).

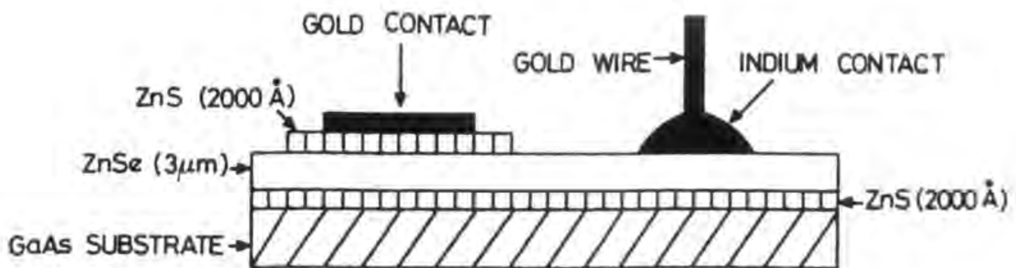

Figure 5.6 ZnSe MIS device with evaporated polycrystalline ZnS I–layer.

5.3.4 Structural assessment

The structural quality of the MIS devices was investigated using RHEED and X–ray diffraction. RHEED patterns typical of those recorded from MOCVD grown and electron beam evaporated ZnS I–layers are shown in figure 5.7a and b respectively. In figure 5.7a, the beam is incident along a <110> zone axis, and the distinct spot pattern and absence of any arcing of the spots or diffraction streaks connecting them provides an indication of the excellent epitaxial quality of the ZnS I–layer deposited by MOCVD. The streaking of the spots in a direction perpendicular and towards the shadow edge is characteristic of diffraction at a very flat surface. Beyond the field of view of the figure, Kikuchi bands were observed, providing a further indication of the excellent crystallinity of the ZnS I–layer. In contrast, the RHEED pattern in figure 5.7b shows that evaporated ZnS I–layers were polycrystalline in nature, with a set of rings corresponding to the zincblende structure, and exhibiting only slight evidence of a preferred orientation.

X–ray diffraction profiles were recorded from ZnS/ZnSe samples, with the ZnS layer uppermost in the diffractometer. Figures 5.8a and b show the (400) diffraction peaks, recorded using cobalt Kα radiation, from the ZnSe and ZnS layers respectively. The ZnSe peak is similar to that recorded from as–grown samples (figure 4.4), except that the peak corresponding to the GaAs substrate is absent. Although the Kα_1/α_2 doublet is still resolved, there is some increase in peak width compared with the as–grown samples, indicative of strain in the epilayers as a result of substrate removal. The effect is more pronounced in the ZnS layer, and the corresponding diffraction peak (figure 5.8b) shows considerable broadening, to the extent that the cobalt Kα_1/α_2 doublet can no longer be resolved. Strain in the epilayers, which arises as a result of relaxation when the substrate is removed, probably accounts for the cracking in structures with relatively thick ZnS I–layers.

Strain effects in heteroepitaxial growth are of importance in optoelectronic applications since they lead to changes in the near band edge (NBE) luminescence spectrum. In MOCVD grown ZnSe, the line widths of the NBE transitions (≥ 1 meV) are broader than those observed in high quality single crystal material (≤ 0.15 meV) [6], and, for ZnSe grown on (100) GaAs, the transitions are shifted to lower energies by 2.5 to 3.5 meV depending on the growth conditions [6]. Two dimensional strain in the growth plane is equivalent to a uniaxial strain parallel to the growth direction, which splits the upper valence band in ZnSe. The effects of such splitting may be observed in the photoluminescence excitation spectrum of the material, from which it is possible to estimate the magnitude of the strain [7]. The effective uniaxial stress can also be calculated using a bi–metallic strip description [8], and for ZnSe on GaAs, both approaches give the same result ($\epsilon = 1.5 \times 10^{-3}$), suggesting that all the mismatch strain is taken up elastically. Although lattice mismatch in the ZnS/GaAs system is greater than for

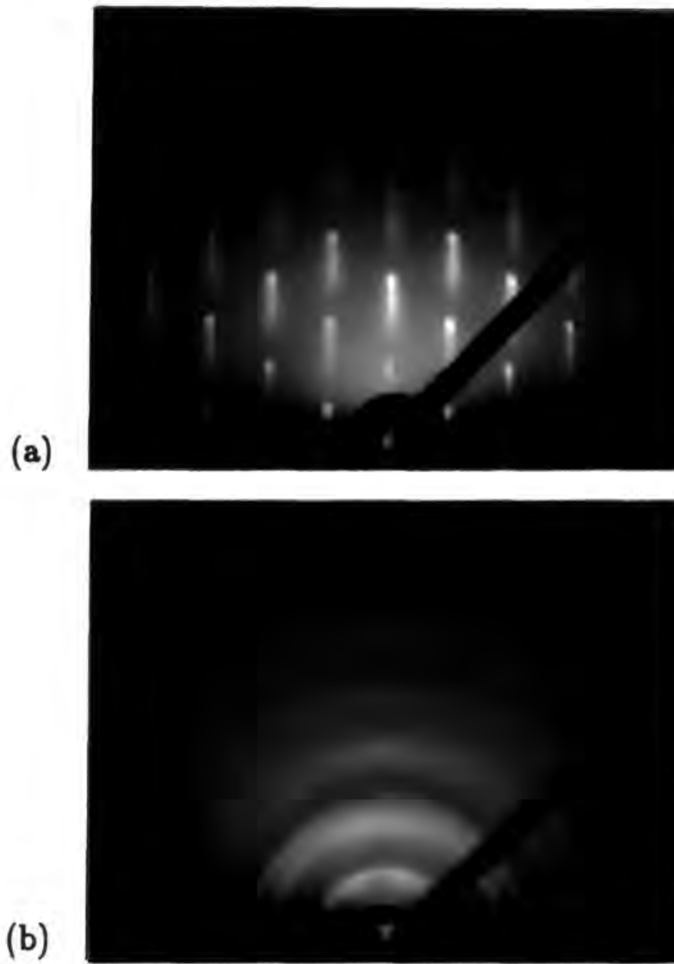

Figure 5.7 100 kV <110> zone axis RHEED patterns recorded from (a) an epitaxial ZnS I–layer, (b) a polycrystalline ZnS I–layer.

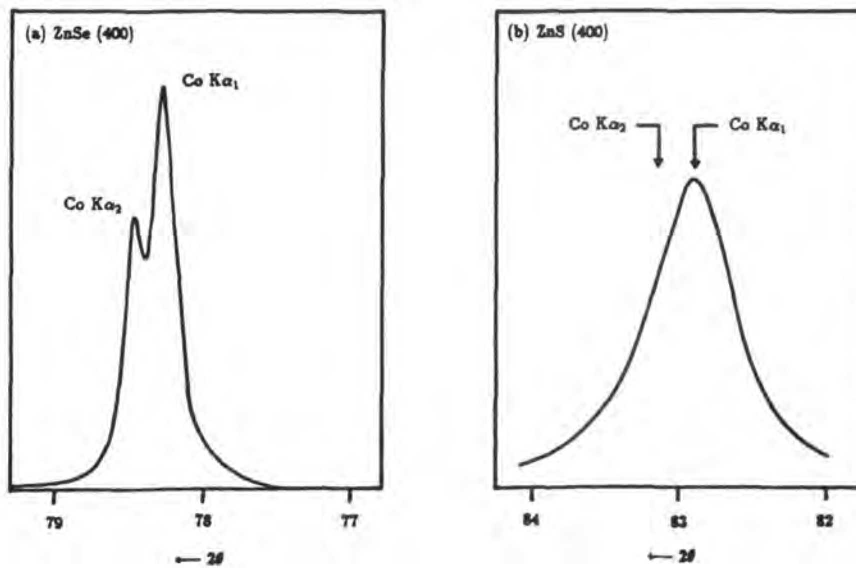

Figure 5.8 X–ray diffraction peaks for the (400) reflection from (a) ZnSe and (b) ZnS, in a ZnS/ZnSe epitaxial structure.

ZnSe/GaAs, shifts in the luminescence spectrum are smaller, indicating that the strain is partially relieved by inelastic processes [6] such as the creation of misfit dislocations.

5.3.5 Surface chemical analysis [1]

The chemical compositions of both the as-grown ZnS surface, and the ZnS surface which was exposed after chemical removal of the substrate, were investigated using electron spectroscopy for chemical analysis (ESCA) with a Kratos ES 300 instrument. Sets of two samples were cleaved from the same ZnS/GaAs wafer, one of which was mounted with the ZnS face down on a glass slide and the substrate removed as described above, while the other was mounted ZnS face up so that the as-grown surface could be analysed. Figures 5.9a and b show respectively the Zn(2p) and S(2p) peaks which were recorded from the as-grown surface. These plots are uncorrected for the effect of specimen charging, which caused the peaks to shift to higher energies. Reference to the carbon peak (from contamination with diffusion pump oil) recorded during the same run indicated that the magnitude of this shift was ~ 7.5 eV. The corresponding zinc and sulphur peaks recorded from the ZnS exposed after chemical removal of the substrate are shown in figures 5.9c and d respectively. The marked asymmetry of the sulphur peak is characteristic of chemical bonding in two different environments. Gallium and arsenic were also detected on the exposed ZnS surface, and figures 5.9e and f show the As(3p) and Ga(2p) peaks respectively. After correcting for the system response and the photo-ionisation cross-sections of the elements, the sulphur concentration (referenced to zinc) was calculated to be a factor of 2.5 higher on the chemically exposed ZnS surface than on the as-grown surface, and the concentration of gallium on the exposed surface was approximately 14 times higher than that of arsenic.

The relatively high gallium and sulphur concentrations, and the observation that sulphur was bonded in two different chemical environments on the exposed ZnS surface, indicates that stable Ga–S bonds are formed at the GaAs/ZnSe growth interface. Further evidence for this conclusion is available in the literature. For example, chemical data from secondary ion mass spectrometry and energy dispersive X-ray analyses confirm that an enhancement in sulphur concentration occurs at the growth interface in the GaAs/$ZnSe_{0.94}S_{0.06}$ system, and also establish that gallium can diffuse into the II–VI layer from the III–V substrate [9]. In a separate study of the GaAs/ZnSe interface grown by MOCVD, ESCA depth profiles recorded using argon ion sputtering revealed the presence of a thin Ga–Se bonded layer at the interface [10]. The formation of a stable Ga–Se layer was found to improve the stoichiometry of the ZnSe at the interface and inhibit direct Zn–As bonding. The relatively low concentrations of zinc and arsenic recorded from the exposed ZnS surface in the present work are in accordance with this

[1] Experimental investigation by Dr. H. Munro and Mr. I. McBriar of the chemistry department, University of Durham.

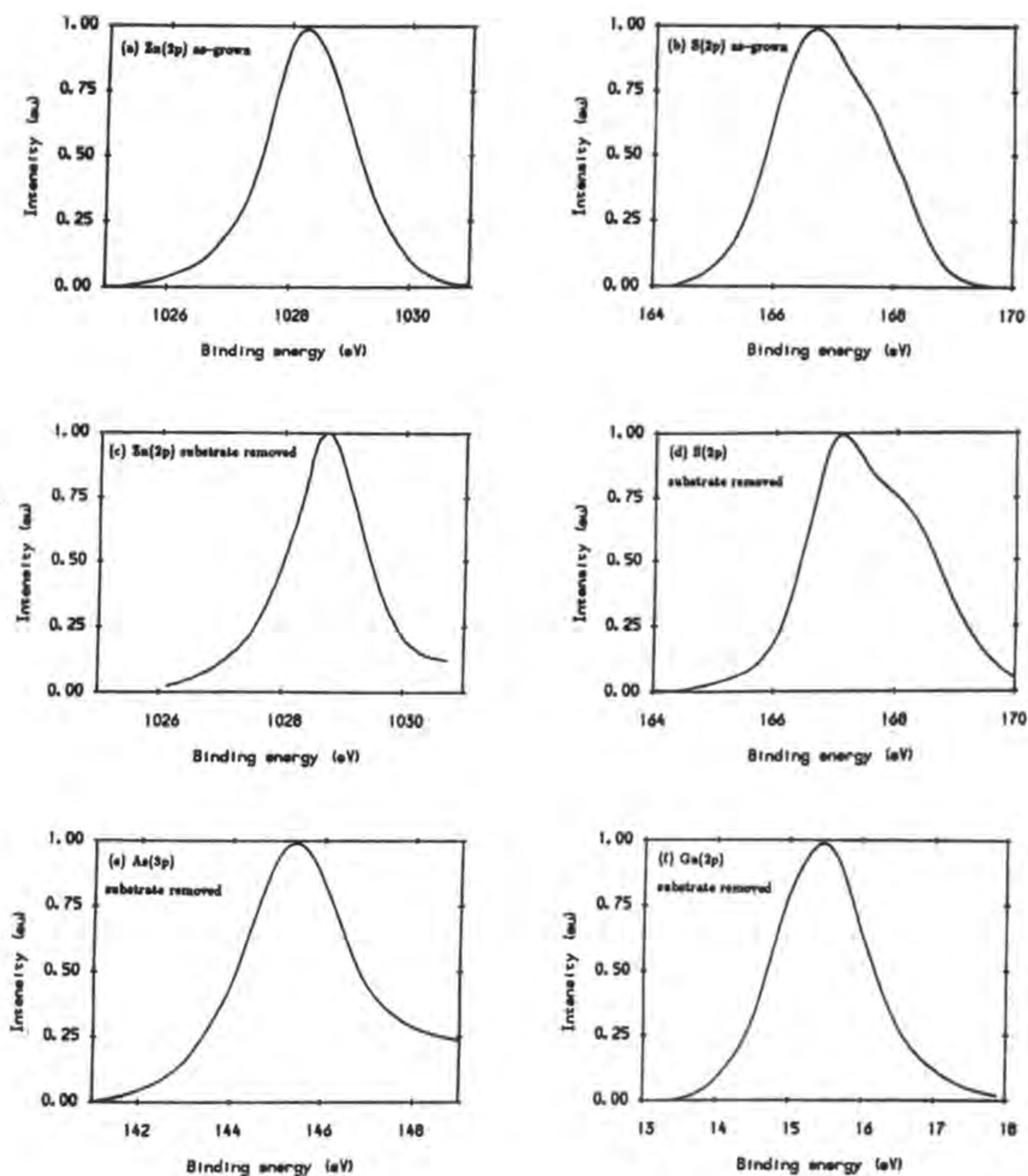

Figure 5.9 ESCA profiles from a MOCVD ZnS I-layer: (a) zinc and (b) sulphur on the as-grown MOCVD ZnS surface; (c) zinc, (d) sulphur, (e) arsenic and (f) gallium on the surface revealed by removal of the GaAs substrate.

finding. The interfacial layer may be up to 17 nm in thickness [10], which represents a significant fraction of the total I-layer thickness ($\sim$ 200 nm) in a practical MIS device.

5.4 Electrical characterisation

MS and MIS devices were characterised electrically using both *IV* and *CV* measurements. Unfortunately, because a pure source of DMZ was not available, the II–VI layers deposited by MOCVD were of inconsistent chemical purity, and since the electrical properties of the ZnSe were strongly influenced by the contamination (possibly gallium), a detailed study of the electrical characteristics of the devices was not undertaken. For the purpose of this thesis the electrical uniformity of the devices was of more immediate importance, and an electron beam induced current (EBIC) study was made in order to investigate the uniformity of current flow in the semiconductor and insulator layers.

5.4.1 Current–voltage characteristics

Several test structures were made in order to determine the suitability of both evaporated and diffused indium electrodes as ohmic contacts to MOCVD ZnSe, which, for the purpose of these measurements, was grown over ZnS on a semi-insulating GaAs substrate. The *IV* characteristics of the contacts were recorded before and after chemical removal of the GaAs, so that any electrical influence from the substrate could be eliminated. In general, the diffused indium electrodes provided a good ohmic contact, which had a linear and symmetrical *IV* response over a wide current range, but the evaporated contacts were less satisfactory in that their *IV* characteristics were non-linear. Figure 5.10a shows the response of typical contacts over a current range of –100 to +100 mA, and clearly illustrates the electrical superiority of the diffused electrodes. Identical *IV* characteristics were recorded both before and after substrate removal. Although the evaporated contacts were less satisfactory electrically, their geometry was more compatible with the thin film structure, and at typical operating voltages their effect on the overall performance of the device was very small. Attempts to form diffused contacts by heating the evaporated indium layers to 220 °C under argon resulted in the electrode breaking up, with the formation of small beads of metal.

Typical *IV* characteristics of MS and MIS devices are shown in figures 5.10b and c respectively. Both devices have a good rectifying response, with a low reverse bias leakage current. However, the shallow gradient of the *IV* plots in forward bias is indicative of a high series resistance. This is probably associated with contamination of the ZnSe by gallium, which results in the growth of resistive material. Because of the contamination, further analysis of the *IV* plots was not considered to be justified, and electrical measurements were concentrated on quantifying the advantages associated with the

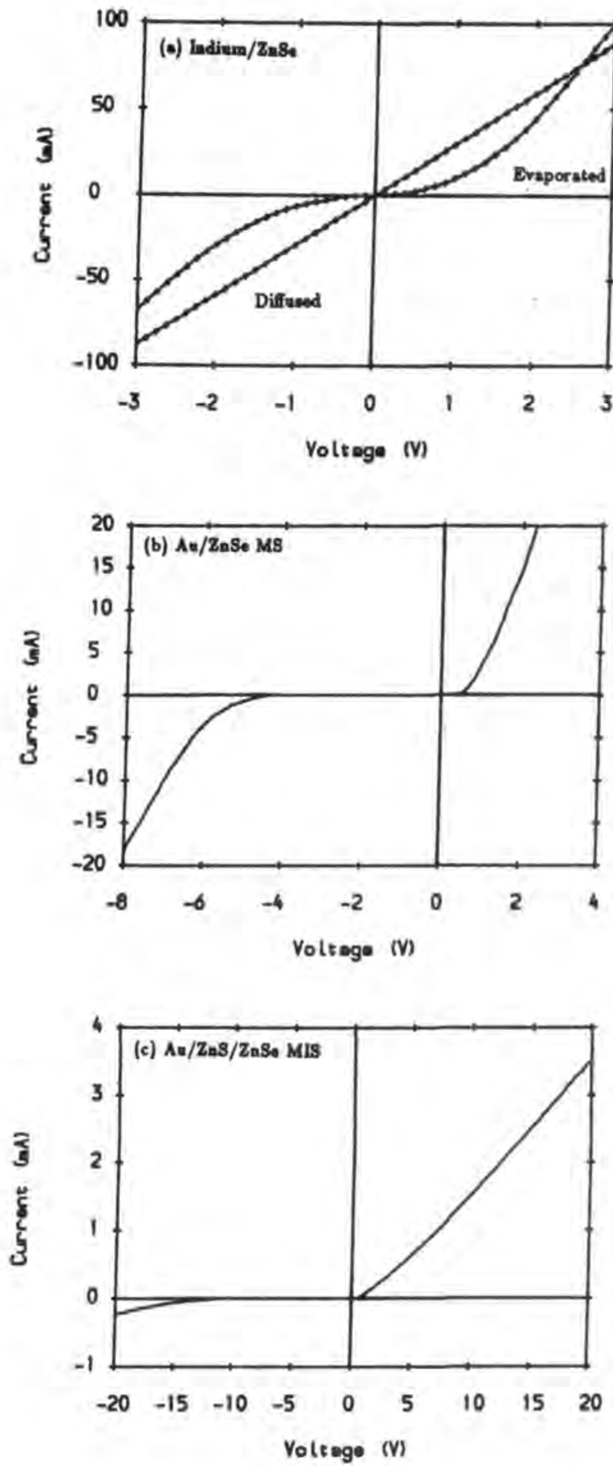

Figure 5.10 Current–voltage characteristics: (a) diffused and evaporated indium contacts on ZnSe, (b) epitaxial Au/ZnSe MS diode, (c) epitaxial Au/ZnS/ZnSe MIS diode.

elimination of the GaAs/ZnSe interface, and the uniformity of the semiconductor and I–layers.

5.4.2 Capacitance–voltage characteristics

The CV characteristics of the MIS structures were recorded in order to establish that any electrical influence attributable to the substrate had been eliminated. Figure 5.11a shows the CV characteristics of an epitaxial Au/ZnS/ZnSe MIS device, while figure 5.11b shows the response of a structure incorporating a GaAs substrate in an Au/ZnS/ZnSe/GaAs series configuration. The CV characteristic of the latter structure deviated markedly from that expected for a simple MIS device, and was probably influenced by a depleted region in the ZnSe at the GaAs/ZnSe interface. However, the response of the thin film structure, in which an ohmic contact was made directly to the ZnSe, approximated the idealised relationship [11] for an MIS device:

$$\frac{1}{C_{total}} = \frac{1}{C_{ZnS}} + \frac{1}{C_{ZnSe}} \tag{5.1}$$

where C_{total} is the total device capacitance, C_{ZnS} the capacitance of the ZnS I–layer, and C_{ZnSe} the capacitance of the ZnSe depletion region. The plateau in figure 5.11a is associated with the voltage independent geometrical capacitance of the ZnS I–layer, which dominates the overall characteristic at low reverse bias voltages when the width of the ZnSe depletion region is very small. For all the devices investigated, the thickness (t) of the ZnS layer, calculated using C_{total} at low reverse bias voltages ($t = \frac{\epsilon}{C}$) was in good agreement with the thickness determined from SEM micrographs of cleaved sections.

5.4.3 Electron beam induced current studies

The EBIC mode of operation of the SEM enables imaging of electrically active defects such as dislocations [12], stacking faults [13], and grain boundaries [14]. EBIC investigations of MIS devices have shown that bright contrast features in the image can be attributed to defects in either the semiconductor or the I–layer [15]. Furthermore, it has been demonstrated that the position of these EBIC contrast features correlates with the position of bright EL spots in bulk ZnSe MIS devices [16]. The purpose of this section is to discuss the EBIC response of both epitaxial ZnSe MS devices, and ZnSe MIS devices with either evaporated polycrystalline or MOCVD grown epitaxial I–layers, and to relate any features in the EBIC image to defects observed using the secondary electron imaging mode of the SEM. The EBIC signal was recorded using a Cambridge S600 SEM, with the electron beam scanning the surface carrying the gold electrode. A reverse bias of between 1 and 2 Volts was applied to the sample from a stabilised DC supply, and a Keithley model 427 low noise current amplifier was used to derive the EBIC signal for the video display.

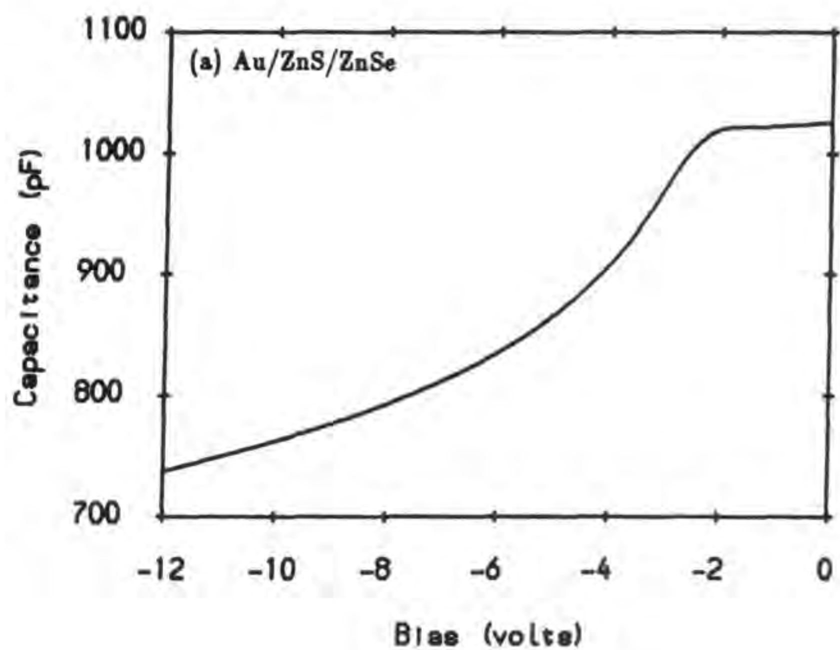

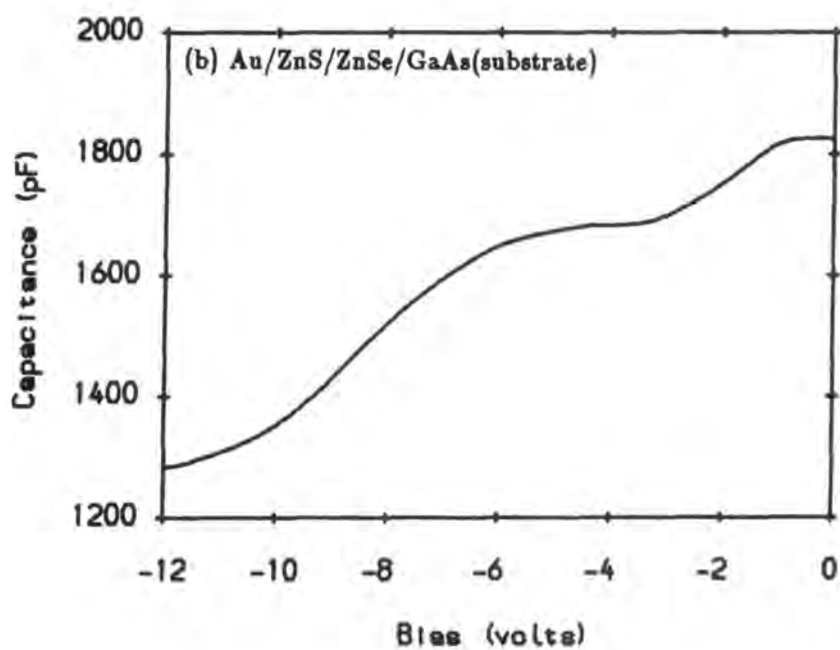

Figure 5.11 Capacitance–voltage characteristics of epitaxial MIS devices: (a) Au/ZnS/ZnSe, (b) Au/ZnS/ZnSe/GaAs(substrate).

With MS devices (figure 5.1), the main feature of the EBIC image was the uniformity of the signal recorded over the gold electrode. With incident electron energies of 7.5 kV or more, the gold contact was semi-transparent to the beam, so that the generation of electron hole pairs and charge collection took place over the entire area defined by the electrode, leading to the EBIC image shown in figure 5.12a. The only contrast observed was at the periphery of the electrode, where the gold was thinner and thus more readily penetrated by the incident electrons. A secondary electron image from the same area, shown in figure 5.12b, demonstrates that both the ZnSe surface and the gold electrode were free from any structural artefacts. An enhancement in the EBIC signal at the edge of a contact can be explained using the simple model shown in figure 5.12c. When the electron beam is scanned across the gold electrode, a larger proportion of its energy is dissipated in the ZnSe under the edge of the contact, where the metal film is thinner and thus more easily penetrated by the incident electrons. Furthermore, the application of a reverse bias causes the depletion layer to extend beyond the edge of the contact, resulting in an additional enhancement to the absorption of incident electrons. Similar EBIC images have previously been reported for MS devices fabricated on bulk single crystal ZnSe [16].

The EBIC images from MIS devices incorporating an evaporated polycrystalline I–layer (figure 5.6) were characterised by an enhanced signal in the region of artefacts in the I–layer. Figures 5.13a and b show a typical EBIC image and a secondary electron micrograph recorded from the same area. Although at first sight these two images do not correlate with each other, careful inspection of figure 5.13a reveals that the central bright spot is surrounded by a region which corresponds to the surface feature shown in figure 5.13b. Such defects in the I–layer are probably associated with foreign particles on the surface which mask the substrate during evaporation of the ZnS, thus producing a pinhole. An enhancement in the EBIC signal over this area is probably a result of greater electron penetration in the thinner region of the I–layer. However, the secondary emission micrograph does not reveal any obvious physical defect at the position of the brightest region of the EBIC image shown in figure 5.13a. This observation may indicate the presence of a localised region of the I–layer with anomalous electrical properties. Similar bright spots in EBIC images have been observed with bulk single crystal ZnSe MIS diodes with evaporated I–layers [16], and also in CdS MIS devices with evaporated SiO I–layers [15].

Figure 5.14a shows that MIS devices incorporating epitaxial ZnS I–layers (figure 5.2) were characterised by an extremely uniform EBIC response over the entire area of the gold electrode. At higher magnifications (figure 5.14b) an enhancement in EBIC signal at the edge of the contact was observed, although this was not so pronounced as in epitaxial MS devices, presumably because the ZnSe depletion region was not directly exposed to the incident electron beam. No other contrast features could

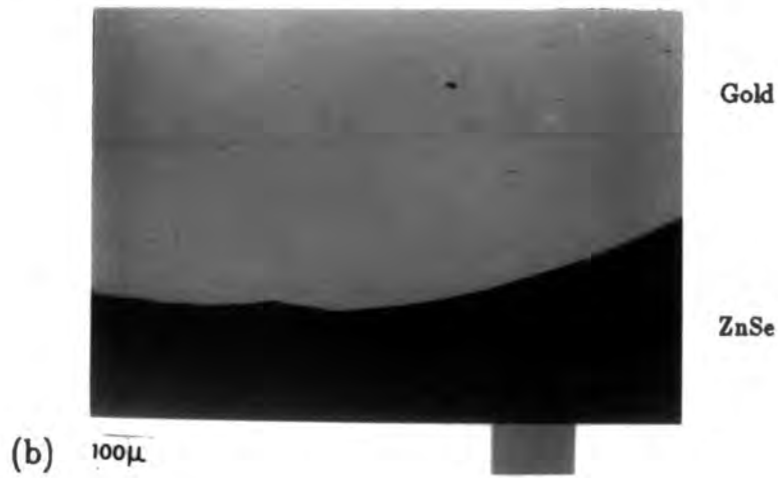

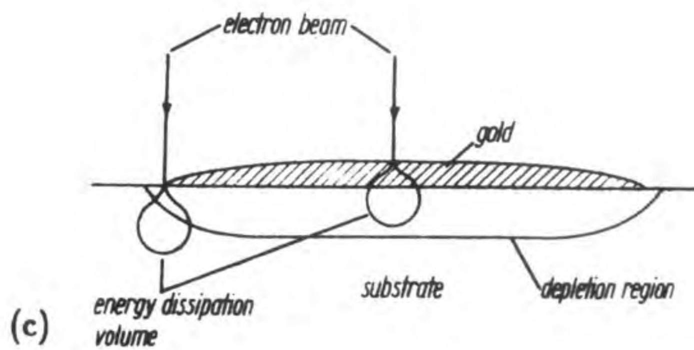

Figure 5.12 **(a) EBIC image and (b) secondary electron micrograph of a gold Schottky contact on epitaxial MOCVD ZnSe, (c) model to explain the EBIC contrast of MS diodes (ref. [15]).**

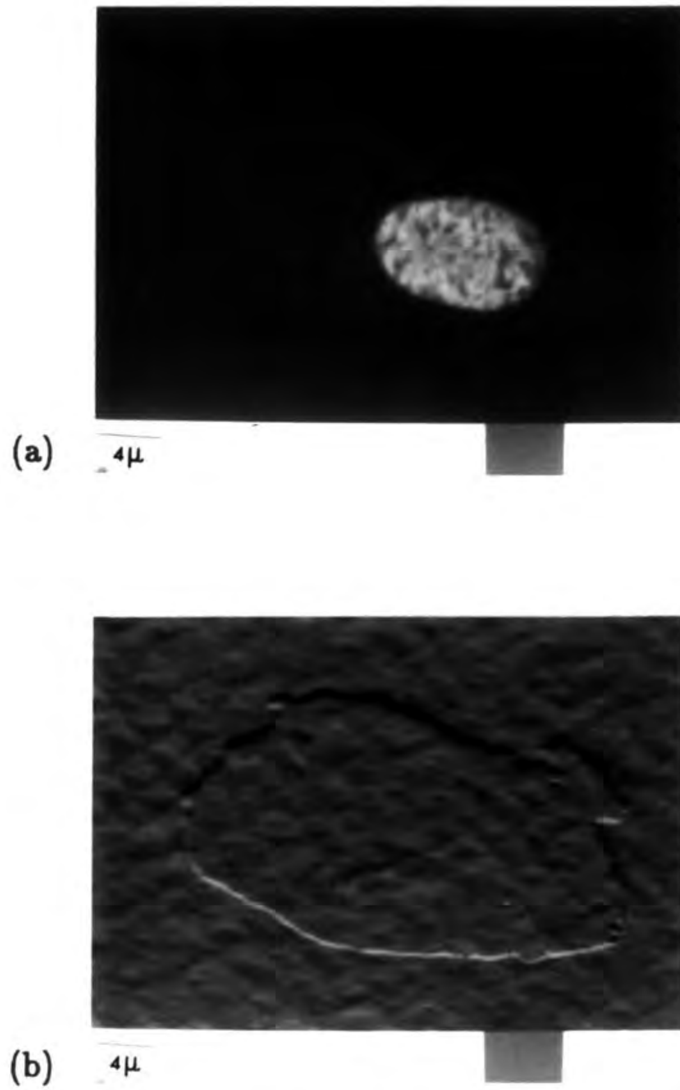

Figure 5.13 (a) EBIC image and (b) secondary electron micrograph of an ZnSe MIS device with a polycrystalline ZnS I–layer.

be detected in either the EBIC or secondary emission modes of the SEM.

The results discussed here illustrate the significant improvement in the electrical uniformity of II–VI compound MIS devices afforded by the use of epitaxial I–layers. Previous workers have attributed a non–uniform EBIC response in MIS devices to pinholes in the I–layer [15] and (non–radiative) recombination centres at the insulator–semiconductor interface [16]. Neither of these effects appears to be significant in the present Au/ZnS/ZnSe MIS devices, providing further evidence for the excellent integrity and uniformity of the epitaxial layers deposited by MOCVD.

5.5 Optical characterisation

5.5.1 Transmittance

In contrast to previous investigations (see for example [16]), the present MIS device geometry allowed the spectral and spatial distribution of EL to be recorded without the need for a transparent top contact. However, the EL was observed through a multilayer structure of ZnSe/epoxy/glass. In order to determine the likely effect of self absorption on the recorded EL spectrum, the overall transmittance of the device was measured using a Pye–Unicam UV–visible spectrophotometer. Figure 5.15 shows the optical transmittance spectra of both ZnS/epoxy/glass and ZnS/ZnSe/epoxy/glass structures. In each case the transmittance cuts off at the band edge of the material with the smallest band gap, and the transmittance of the latter spectrum, which corresponds to the MIS geometry, falls to only 1% for incident light of energy $\geq$ 2.72 eV. An unfortunate consequence is that any EL in this region of the spectrum will be severely attenuated in comparison with lower energy emission (eg the self activated emission band).

5.5.2 Electroluminescent spectrum

The EL emission spectra of both MS and MIS structures were recorded using the system described in section 3.3.1, with the devices operating at 77 K. Figure 5.16a shows a typical EL spectrum, comprising both NBE and deep centre emission, which was recorded from a MS diode operating in forward bias at 15 mA. The low optical efficiency of this simple MS device (in which the substrate was retained) prevented a detailed analysis of the NBE emission, because of the necessity to use a large slit width on the monochromator in order to provide sufficient signal. The deep centre emission is almost certainly self activated luminescence [17], which arises in highly doped n–type material as a result of the self compensation mechanism (section 2.2.4). To the naked eye, the blue EL emission appeared to be concentrated around the edge of the gold electrode on the ZnSe surface, while yellow emission was observed at the cleaved edges of the GaAs/ZnSe wafer. It is possible that the "true" EL spectrum contained a much larger proportion of NBE emission, which was attenuated by self absorption in the

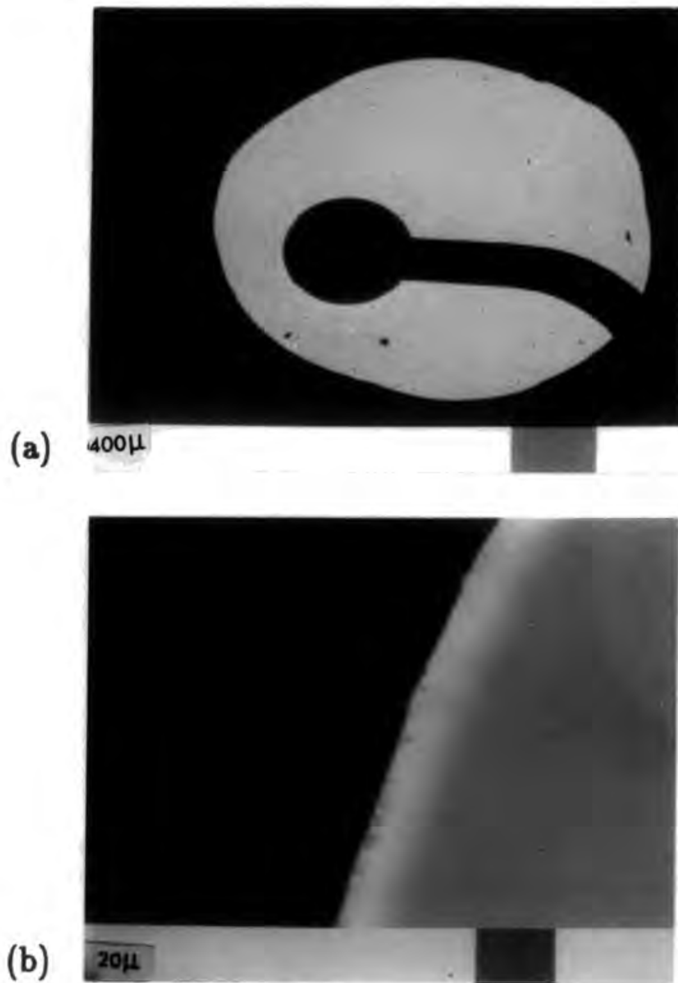

Figure 5.14 EBIC images of a ZnSe MIS device with an epitaxial ZnS I-layer at (a) low and (b) high magnification.

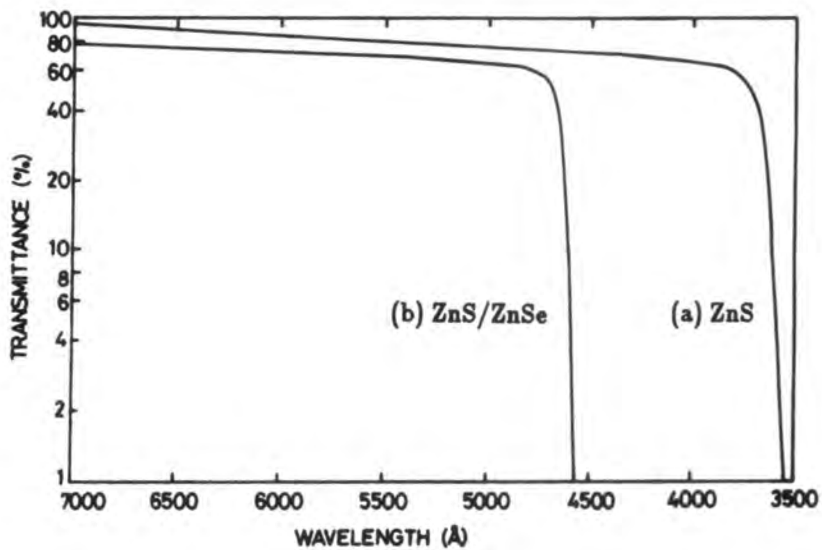

Figure 5.15 Optical transmittance spectra of (a) ZnS/epoxy/glass and (b) ZnS/ZnSe/epoxy/glass structures.

ZnSe. This would explain the difference in the colour of luminescence observed on the surface and at the edge of the wafer.

The EL spectra of MIS devices were also dominated by the self activated emission band. Figure 5.16b shows a typical spectrum recorded from a device operating under a forward bias of 15 mA at 77 K. None of the MIS devices investigated showed any measurable NBE emission, but because of contamination with gallium, it was not clear whether this was a result of self-compensation or self-absorption in the ZnSe.

5.5.3 Spatial distribution of electroluminescence

Although forward biased ZnSe EL MIS diodes have been investigated extensively, attention has generally been focused on determining the origin of the spectral distribution of EL. Recently, it has been shown that the *spatial* distribution of EL is also an important factor, because the introduction of a polycrystalline I-layer results in a very non-uniform distribution of bright EL spots [16]. Since II-VI compound MS EL devices exhibit a homogeneous spatial distribution of EL, the origin of non-uniformity in MIS devices can be attributed to the introduction of the I-layer. As well as giving a poor aesthetic appearance, the spots are indicative of localised regions of high current density, which will probably have an adverse effect on the device lifetime.

It has previously been demonstrated that the EBIC image of MIS diodes correlates well with the spatial distribution of EL [16]. Since the EBIC response of the present MIS devices was homogeneous, it was thought likely that the spatial distribution of EL would also be uniform, and examination of the EL emission with the naked eye and a low power optical microscope confirmed this expectation. A photograph of the EL emission over the gold contact is shown in figure 5.17, which illustrates the highly uniform nature of the luminescence [1]. The only contrast is a shadow towards the left of the electrode which was caused by excess epoxy on the glass slide. Texture in the image is a result of air bubbles trapped in the epoxy resin used to mount the epilayers. Again, this result is indicative of the high quality and electrical uniformity of the ZnS I-layers and ZnSe luminescent layers which were deposited by MOCVD.

5.6 Summary

The fabrication of both MS and MIS EL devices has been discussed in this chapter, and the characteristics of structures incorporating epitaxial and polycrystalline I-layers have been contrasted. Simple MS devices enabled rapid assessment of the EL characteristics of MOCVD grown ZnSe, but did not allow observation of the spatial distribution of luminescence. Furthermore, *CV* measurements on MIS devices, where the substrate was retained in a GaAs/ZnSe/ZnS/Au series configuration, revealed the presence of an undesirable electronic barrier at the GaAs/ZnSe interface. Both of these disadvantages

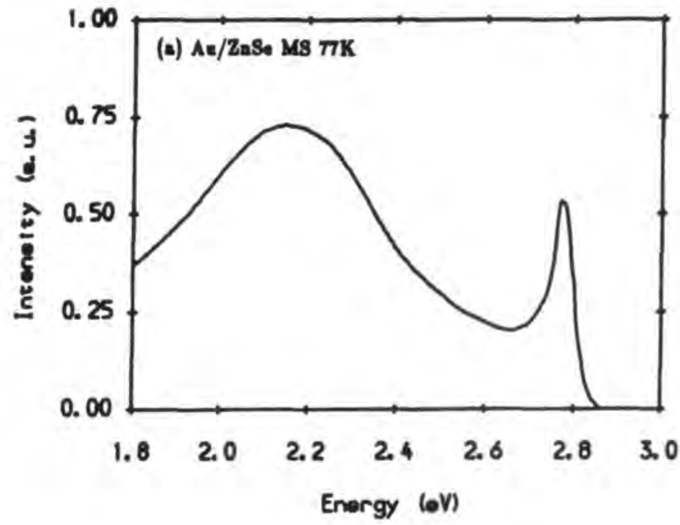

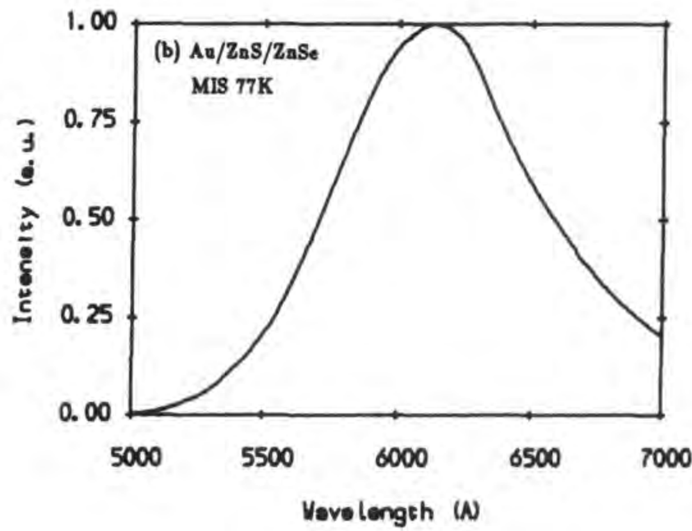

Figure 5.16 Typical EL spectra of epitaxial EL devices: (a) Au/ZnSe MS, (b) Au/ZnS/ZnSe MIS.

Figure 5.17 Spatial distribution of EL from a ZnSe MIS diode with an epitaxial ZnS I-layer (actual contact diameter 1.5 mm).

were overcome using an alternative device geometry, which allowed electrical contacts to be made directly to the II–VI compound epilayers. Difficulties associated with chemical attack of the ZnS I–layer during removal of the substrate were avoided by using a sequential etching process involving III–V compound chemi–stop layers, which were deposited by MOCVD onto the GaAs substrate prior to growth of the II–VI layers.

A comparative study of MIS devices incorporating epitaxial and polycrystalline I–layers clearly demonstrated the superiority of the epitaxial I–layers deposited by MOCVD. RHEED indicated that the epitaxial I–layers were of extremely high structural perfection, with a very flat and uniform surface. EBIC studies demonstrated the marked improvement in electrical uniformity afforded by the use of an epitaxial device structure. This conclusion was confirmed by the greatly improved spatial uniformity of EL in these devices.

The results discussed here demonstrate the inherent uniformity of current distribution and EL in epitaxial II–VI compound devices. In the following chapter the application of these structures to a study of more commercially orientated thin film DCEL displays is discussed. At present, non–uniformity of current distribution and subsequent localised breakdown is a significant obstacle to the commercial exploitation of these devices.

CHAPTER SIX

DC ELECTROLUMINESCENCE IN EPITAXIAL THIN FILM ZnS:Mn/ZnSe STRUCTURES

6.1 Introduction

The ZnS:Mn electroluminescent panel is an attractive prospect for the production of a low cost, large area display device, and many different forms of EL panel displays are available (section 2.4.2). Discussion in this chapter will be restricted to DC coupled cells, which offer the possibility of producing large area displays, without the complex driving circuitry associated with AC driven panels.

DC thin film EL (DCTFEL) panels, fabricated using conventional thin film deposition methods such as vacuum evaporation and sputtering, have been the subject of several studies aimed at elucidating the physical processes of current conduction and luminescence. Initially, all–thin–film DCEL devices were based on active luminescent layers of copper doped ZnS:Mn, with a composition similar to that used in powder type cells. The role of copper in these structures is not completely understood, although it is known to form a p–type Cu_xS phase at the surface of the ZnS film, and recombination of holes injected from this layer with electrons injected into the ZnS from a metal contact has been proposed as a possible excitation mechanism for the Mn^{2+} ion [1]. By incorporating copper in high concentration [2], it is possible to use a "forming" technique (section 2.4.2) to provide the field enhancement, homogenisation and localised load resistance which are thought to be essential in obtaining non–destructive and uniform EL at low voltages [3]. The main disadvantage of these devices is a relatively short operational lifetime (of the order of a few tens of hours [4]), which is associated with migration of copper under the applied electric field. More recently, high EL intensities and longer operational lifetimes have been obtained in copper free ZnS:Mn [5] structures. Since these devices are prone to avalanche breakdown, current control layers are sometimes included in the structure in order to inhibit localised breakdown mechanisms. Two different types of control layer have been used, the functions of which are best illustrated by specific examples [6]. The first of these is an RF sputtered layer of amorphous silicon with a low field resistivity of 10^4 Ω cm, which behaves as a localised load resistance, preventing current runaway. A second form of control layer is a 20%Ni/SiO_2 cermet with a resistivity of 100 Ω cm, which is RF sputtered from a SiO_2 target overlaid with strips of nickel. The cermet appears to act as an array of point contacts, breaking up the current across the ZnS:Mn layer into discrete paths, and so preventing catastrophic current runaway should one of these paths breakdown.

Unfortunately, commercial exploitation of DCTFEL panels has been limited by their relatively short operational lifetime, which is in part associated with the occurrence of localised destructive breakdown (LDB). This problem has recently been addressed in a theoretical analysis of the device, where a dielectric breakdown model of EL was developed [7,8]. Good qualitative agreement with experimentally observed steady state device characteristics was found. However, although the sputtering technology used in the experimental work enabled high quality films to be produced, their microstructure was complex [6], raising the possibility of materials artefacts influencing the device characteristics. Furthermore, the theoretical work was handicapped by a lack of data for the polycrystalline or semi–amorphous material used [7]. Thus, in addition to the commercial requirement for an inexpensive thin film deposition technique, there is a clear need for a well controlled device technology for research purposes. High quality injection and luminescent thin films are required so that dielectric breakdown and injection phenomena in ZnS:Mn phosphors can be studied in the absence of any influence from materials artefacts.

The work discussed here is aimed at addressing some of these requirements. It has already been demonstrated that ZnS/ZnSe films deposited by MOCVD exhibit a highly uniform spatial distribution of current flow and luminescence. These characteristics are desirable in a study of DCTFEL, where short device lifetimes appear to be associated with localised high current filaments [6]. Furthermore, physical data for materials in single crystal form are widely available, enabling a more realistic comparison of theoretical predictions with experimental observations to be made. The high structural quality of single crystal devices also allows fundamental effects to be distinguished from those due to materials artefacts. In this chapter the fabrication of an epitaxial ZnS:Mn structure, and its application in a study of steady state and transient effects in DCTFEL devices, are discussed. Comparisons are made with commercial powder panels and sputtered structures, and the influence of operational conditions on the nature of breakdown phenomena is discussed.

6.2 Device fabrication

6.2.1 Current DCTFEL device geometries

Before describing the epitaxial thin film structure used in the present investigation, it is useful to consider some DCTFEL structures which have previously been used in fundamental studies, or are under development for commercial exploitation. Directly coupled operation is difficult to achieve in thin–film–only structures [9], although DCEL has been investigated in MOCVD grown polycrystalline ZnS:Mn [10], using a composite [11] (powder/film) structure. These devices yielded EL properties comparable with those of thin film structures produced using other deposition techniques, although they

still required a powder based current control layer to be deposited in the traditional way. All–thin–film devices, incorporating a sputtered MnO_2 control layer, suffered significant deterioration after 24 hours running through erosion of both MnO_2 and the accompanying aluminium electrode [10]. Of more direct interest to the present study, DCTFEL devices based on a ZnS:Mn/ZnSe structure have been investigated, although it should be emphasised that in these devices the layers were polycrystalline (deposition was by vacuum evaporation), and therefore subject to the influence of grain boundaries *etc.* There has also been some question as to the primary role of the ZnSe. In one study [12] it was shown that the ZnSe acted as a distributed resistive layer, which protected the ZnS:Mn against avalanche breakdown. In the other investigation [13] the ZnSe was considered to play an important part in carrier injection. These different interpretations provide further evidence of the need for a reproducible epitaxial device fabrication technology. Single crystal DCTFEL devices have been studied [14], but these were grown over a GaAs substrate, thus introducing an electronic barrier which is not present in commercial devices. One further device which is of relevance to the present study is a copper free ZnS:Mn thin film structure [6], which is currently being developed for the commercial market. These structures are fabricated by RF sputtering a layer of ZnS:Mn over a transparent conducting cadmium stannate electrode on a glass substrate, followed by deposition of aluminium electrodes onto the ZnS:Mn by thermal evaporation. Some samples are provided with a current control layer of either DC sputtered amorphous silicon or RF sputtered Ni/SiO_2 cermet, which are found to reduce the LDB rate.

6.2.2 MOCVD growth and epitaxial DCTFEL device fabrication

The fabrication sequence for epitaxial DCTFEL structures [15] was very similar to that already described for epitaxial ZnS/ZnSe MIS devices (section 5.3.1). The additional requirement for the production of DCTFEL devices was a suitable source of manganese during MOCVD growth of the ZnS layer. In MOCVD, dopants are usually incorporated by adding a small amount of a volatile alkyl compound to the carrier gas stream. Unfortunately no simple stable manganese alkyl compound exists, however an alternative compound, tricarbonylmethyl cyclopentadienyl manganese (TCM) (figure 6.1), which is liquid at room temperature with an acceptable vapour pressure [16], was available. Recently, it has been demonstrated that another compound, di–π–cyclopentadienyl manganese, can be used as a dopant in the growth of ZnSe:Mn DCEL cells [17]. This compound does not contain oxygen, which is thought to degrade the performance of EL cells. Unfortunately, such a source was not available for this work.

The DCTFEL device layers were grown by MOCVD onto (100) oriented GaAs substrates. The conditions were similar to those described previously (section 4.2.3), except that the growth temperature for ZnS:Mn was increased in order to crack the TCM. A

layer of ZnS:Mn of thickness ~0.2–1.0 μm was grown at a temperature of 400 °C, with a manganese bubbler temperature of 70 °C [16]. Subsequent to this growth the apparatus was flushed for 2 minutes to expel H_2S from the reaction cell, and the substrate temperature reduced to 275 °C before growing a layer of ZnSe approximately 3 μm thick over the ZnS:Mn. RHEED patterns recorded from the as-grown layers showed that they were of excellent crystallinity. The mean concentration of manganese in the ZnS films was determined by dissolving a thick (~10 μm) layer in a mixture of concentrated HCl and HNO_3 acids. The resulting solution was analysed for zinc and manganese by atomic absorption spectroscopy. Typically, the manganese concentration, expressed as a weight percentage with respect to zinc, was ~0.1 %. The ZnSe produced was n-type with an uncompensated carrier concentration of 3–4$\times 10^{16}$ cm^{-3} and a resistivity of approximately 0.7 Ω cm. Conducting ZnSe was used to allow the breakdown behaviour of the structure to be investigated; no attempt was made to optimise the device lifetime through the use of current control layers.

A 2 mm wide aluminium contact of thickness 200 nm was deposited onto the ZnSe by thermal evaporation, and the structure mounted with the aluminium face downward on a glass slide using epoxy resin such that the GaAs substrate remained exposed. The substrate was removed by an etch comprising 95% H_2O_2 (100 volumes) and 5% NH_3 (35% solution), which was used at room temperature. Transparent gold top electrodes of width 2 mm were deposited perpendicular to the first aluminium electrode by thermal evaporation onto the exposed ZnS:Mn surface, forming a "pixel" with an active area of 4 mm^2. The final structure is illustrated schematically in figure 6.2, and figure 6.3 shows a photograph of a typical four pixel device.

6.3 Device characterisation

6.3.1 The dielectric breakdown theory of DCEL

Localised dielectric breakdown in DCTFEL devices has, in the past, been attributed to geometrical artefacts introduced during film deposition. However, recent studies have shown that this explanation is inconsistent with experimental observations [6], and have also indicated that in ZnS:Mn, both LDB and EL may be consequences of dielectric breakdown. A computational equilibrium model has shown that with assumed values for electronic parameters, current controlled negative differential resistance (CC-NDR) is expected under normal operating conditions [7,8]. A natural consequence of CCNDR is localised (filamentary) conduction [18], which may account for a number of the operational characteristics of practical DCEL devices, including LDB.

Figure 6.4 shows a schematic band diagram of a ZnS:Mn DCEL device under different bias conditions [7,8]. The ZnS is taken to be insulating, and the low net donor density implies that carrier depletion does not locally enhance the cathode field.

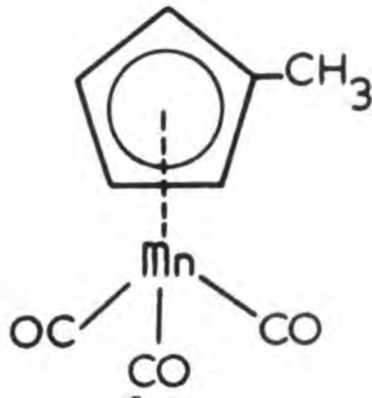

Figure 6.1 The structural formula of tricarbonylmethyl cyclopentadienyl manganese (ref. [16]).

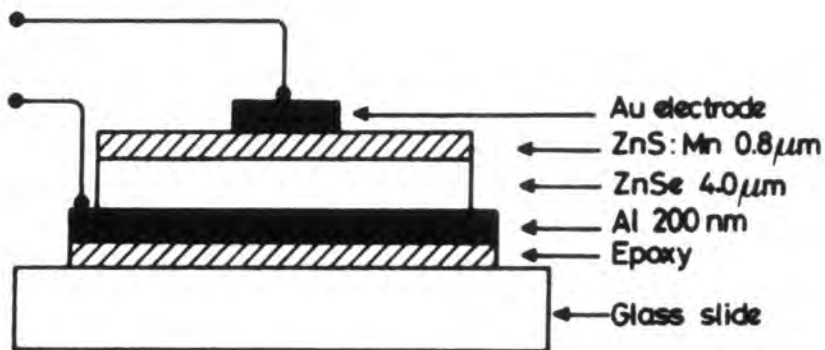

Figure 6.2 Epitaxial thin film ZnS:Mn DCEL device geometry.

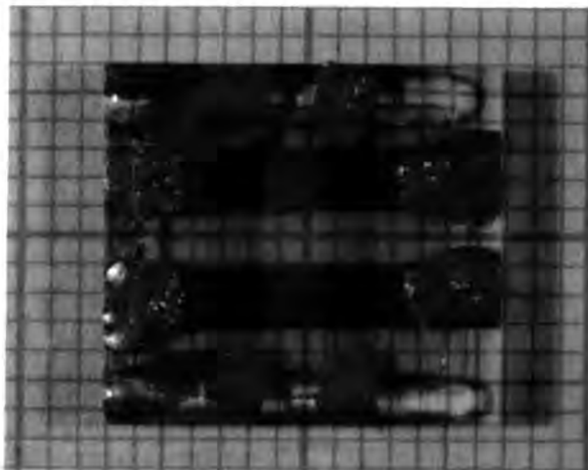

Figure 6.3 Plan view of a four pixel epitaxial DCTFEL device (mm grid).

Under moderate bias all of the applied voltage is dropped across the semiconductor and the current is limited by thermionic emission. As the field increases, the barrier at the interface becomes thinner and tunnelling becomes significant. With sufficiently high fields holes can be created in the ZnS valence band by impact ionisation, and these holes drift towards the cathode under the influence of the electric field. The low mobility of the holes results in their accumulation at the cathode and this affects the charge distribution in the ZnS, enhancing the cathode field as shown in figure 6.4c. As a result of the localised field enhancement the tunnelling current is increased, which in turn leads to further hole creation through impact ionisation, causing a further increase in the cathode field. Thus a "positive feedback loop" may be established, leading to CCNDR and filamentary conduction.

The steady state behaviour of DCEL devices can be modelled using a set of equations which relate the carrier concentration in the ZnS:Mn to the electric field [7,8]. The first of these is Poisson's equation, giving the spatial derivative of the field in terms of charge density:

$$\frac{dE(x)}{dx} = \frac{|e|}{\epsilon\epsilon_o}(p(x) - n(x)) \tag{6.1}$$

where $E(x)$ is the field at a distance x from the cathode, and $n(x)$ and $p(x)$ are the electron and hole concentrations respectively. The current continuity condition implies that:

$$J_{total} = J_n(x) + J_p(x) \tag{6.2a}$$

$$= n(x)|e|\mu_e E(x) + p(x)|e|\mu_h E(x) \tag{6.2b}$$

where μ_e and μ_h are the mobilities of the electrons and holes. As a result of impact ionisation, the electron current increases with distance from the cathode. The change in the electron current is given by:

$$\frac{dJ_n(x)}{dx} = \alpha(E(x))J_n(x) \tag{6.3}$$

where α is the probability of an impact ionisation event per unit length. Finally, the tunnelling current through the triangular barrier at the cathode is given by Lampert and Mark [19] to be:

$$J_n(0) = \frac{[|e|E(0)]^2}{(4\pi)^2 h\phi}\left[1 + \frac{4\pi^2 m^*(kT)^2\phi}{3h^2|e|[E(0)]^2}\right]\exp\left[\frac{-4(2m^*|e|)^{\frac{1}{2}}\phi^{\frac{3}{2}}}{3hE(0)}\right] \tag{6.4}$$

where m^* is the electron effective mass, h is Planck's constant, and ϕ the barrier height.

A simultaneous analytical solution to these equations is not possible, but by dividing the device into elements along the field direction, Poisson's equation and the

current relationships can be solved iteratively to obtain a self consistent result [7,8]. Figure 6.5 shows the predicted *IV* characteristic obtained using materials parameters for bulk ZnS, assuming a barrier height of 0.5 eV [20] and a ZnS:Mn layer thickness of 1.5 μm. CCNDR is predicted, but only at a current density of 10^8 Am^{-2}, which is much greater than that used in practical DCTFEL devices ($\leq 10^4$ Am^{-2}) [7]. The calculated curve shown in figure 6.5 was obtained using the single crystal values for electron and hole mobilities (10^{-2} and 10^{-4} $m^2s^{-1}V^{-1}$ respectively), but given the polycrystalline nature of the ZnS employed in devices the carrier mobilities are likely to be very much lower in practice. Furthermore, since carrier mobility is expected to decrease under high fields [21] the literature values are likely to be very much greater than those arising under typical operating conditions. Reducing the value of electron mobility was found to have very little effect on the calculated *IV* characteristic, because the resulting increase in electron concentration was compensated by a corresponding change in the hole concentration. However, a reduction in the hole mobility was found to have a pronounced effect on the calculated *IV* characteristics since greater charge accumulation was then predicted at the cathode, causing a significant reduction in the barrier width. Figure 6.6 shows the predicted *IV* characteristic for different hole mobilities in the range 1×10^{-5} to 1×10^{-4} $m^2s^{-1}V^{-1}$. By using a mobility which is 2–3 orders of magnitude lower than the single crystal value, CCNDR is predicted at a voltage and current density consistent with experimental observations [7].

6.3.2 Experimental current–voltage characteristics

The *IV* characteristics of the single crystal DCTFEL devices were recorded under continuous drive using a ramped current source. A typical *IV* curve is shown in figure 6.7, together with a curve obtained from a conventional powder display of the type shown in figure 2.25. The *IV* characteristics of powder devices are dominated by components other than the phosphor layer [22], but the use of low resistivity ZnSe as the injecting layer in the epitaxial structure implies that the *IV* characteristic is likely to be more representative of the behaviour of the active device components.

The results of the dielectric breakdown theory discussed above apply to the active ZnS:Mn layer, but in a real device there are many other influences on the overall characteristic such as the electrode impedance, and thus it is not possible to observe a negative slope in the external *IV* characteristic. As a result of CCNDR, the total current flowing in a DCEL device may be composed of two components. Firstly, there is a uniform "background" current which increases in magnitude with the externally applied voltage, following the lower branch of the *IV* curve. Secondly, at higher current densities, the localised filamentary current component becomes more significant, and the voltage across the ZnS:Mn may decrease as the current density increases. Although filamentary conduction involves a reduction in the voltage across the ZnS:Mn, this is

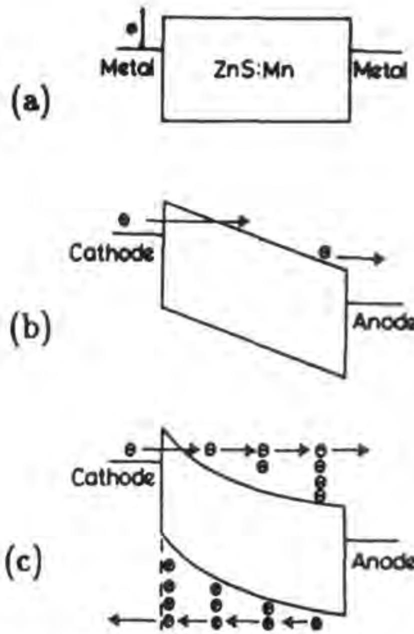

Figure 6.4 The idealised energy band diagram of a DCEL device: (a) at sero bias, (b) with moderate bias, (c) with a localised region of high electric field at the cathode.

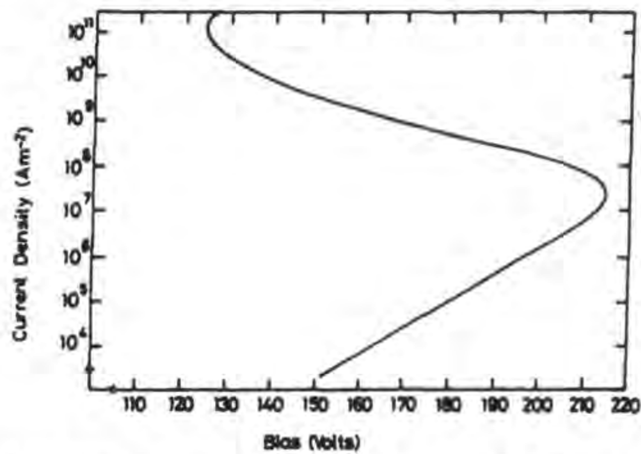

Figure 6.5 Calculated *IV* characteristic for a DCEL panel 1.5 μm thick with a barrier height ϕ=0.5 eV (ref. [8]).

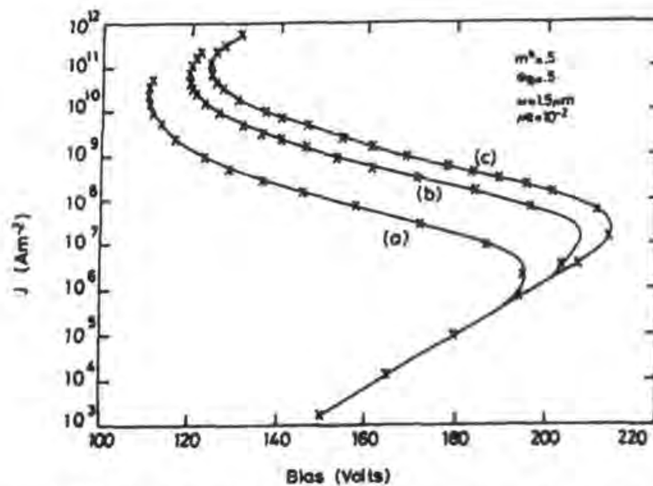

Figure 6.6 Calculated *IV* characteristics for hole mobilities of (a) 1×10^{-5}, (b) 5×10^{-5}, (c) 1×10^{-4} $m^2s^{-1}V^{-1}$ (ref. [8]).

not accompanied by a corresponding fall in the external voltage since an increased voltage is developed across the local (internal) load resistance. Thus the *externally* measured *IV* curve is expected to include a vertical region, corresponding to an increase in the filamentary component of the total current without a decrease in the externally measured voltage. The vertical region in the measured *IV* characteristic of epitaxial DCTFEL devices (figure 6.7) was found to correlate with a dramatic change in their breakdown behaviour, indicative of a large increase in the filamentary component of the current (section 6.5).

6.3.3 Electroluminescent spectrum

The EL emission spectra of epitaxial DCTFEL devices were recorded using the system described in section 3.3.1. Figures 6.8a and b show respectively typical spectra recorded from an epitaxial DCTFEL structure and a conventional powder device, both of which were driven using 100 V pulses of duration 10 μs with a 1% duty cycle. Both devices exhibited the characteristic Mn^{2+} luminescence peaking at 585 nm [1] (section 2.2.5). Since the spectra obtained from epitaxial DCTFEL structures were identical to those of traditional powder devices a more detailed study was not undertaken. As with the MIS devices discussed in section 5.5.3, the *spatial* distribution of EL was of more immediate importance in the present investigation of dielectric breakdown and EL in ZnS:Mn.

6.3.4 Spatial distribution of electroluminescence

Before considering the spatial distribution of EL in epitaxial DCTFEL devices it is worth summarising some earlier results in this thesis, which have indicated that the structural and electrical characteristics of epitaxial ZnS/ZnSe structures are spatially highly uniform. In particular, RHEED investigations have demonstrated the excellent structural quality of the II–VI layers deposited by MOCVD, and XTEM studies have shown that the defect structure of the layers is independent of their thickness. An EBIC study of both MS and MIS epitaxial devices illustrated the significant improvement in the electrical uniformity of II–VI compound devices afforded by the use of epitaxial I–layers, and this result was confirmed by the greatly improved spatial distribution of EL in epitaxial MIS devices.

Figure 6.9 shows photographs of the spatial distribution of EL in epitaxial DCTFEL devices with different thicknesses of ZnS:Mn. The devices were driven using 100 V pulses of duration 10 μs with a 1% duty cycle in order to simulate typical operating conditions (in matrix addressed displays). Under these conditions operation was sufficiently stable (section 6.5) to enable time exposures of the EL to be made. The non–uniform spatial distribution of EL, despite the high degree of structural perfection of the epitaxial structures, indicates that filamentary conduction was occurring in the

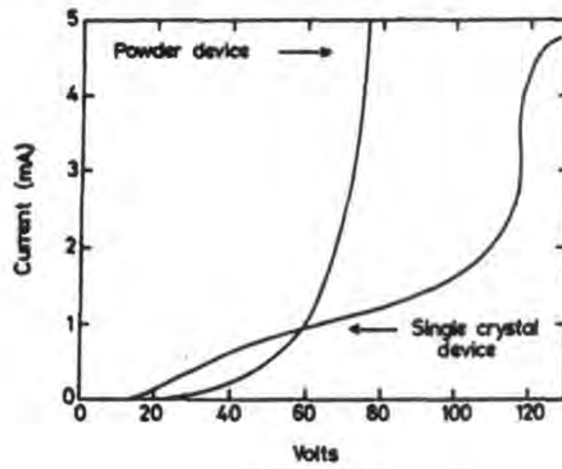

Figure 6.7 The *IV* characteristics of powder and single crystal ZnS:Mn DCEL devices.

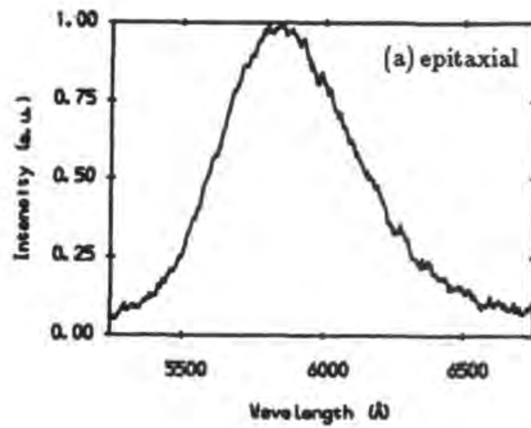

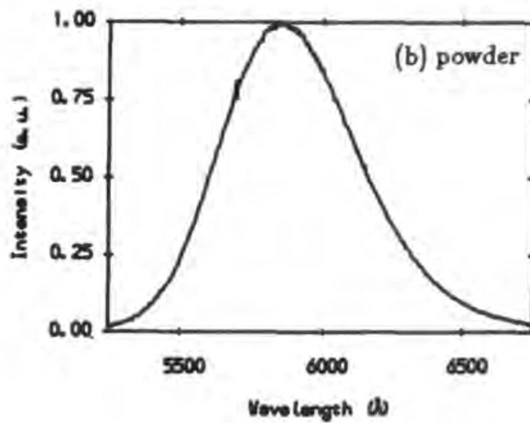

Figure 6.8 Electroluminescent spectra recorded from (a) epitaxial, and (b) powder type DCEL devices.

ZnS:Mn in accordance with the dielectric breakdown theory of DCEL. In contrast, a very similar structure incorporating an *un–doped* ZnS layer in a Au/ZnS/ZnSe MIS LED (section 5.3), was characterised by a highly uniform spatial distribution of EL (figure 5.17). Both devices were of comparable structural perfection, and both were operated un–encapsulated in the same ambient. Single crystal epitaxial material is less likely to be susceptible to ambient effects such as humidity (which can increase the LDB rate in sputtered devices [6]), due to the absence of grain boundaries *etc.* One possible explanation of the results shown in figure 6.9 might be clustering of manganese during MOCVD growth. However, secondary ion mass spectrometry has shown that the radial distribution of manganese is uniform to within the limit defined by the 60 μm diameter area over which the secondary ions were collected [16]. It is thus reasonable to interpret filamentary conduction in epitaxial DCTFEL devices in terms of the physical mechanism of carrier injection.

It is clear from figure 6.9 that the spatial distribution of EL varies with the thickness (t) of the ZnS:Mn layer, ranging from uniform emission with t = 1.27 μm (figure 6.9a), to entirely filamentary with t = 0.35 μm (figure 6.9c), and showing mixed behaviour with intermediate thicknesses (figure 6.9b). The tendency towards decreased filamentary conduction with greater ZnS:Mn layer thickness appears at first sight to be anomalous, since an increase in the device thickness would be expected to lead to an increase in the total hole population (through impact ionisation), resulting in a more pronounced CCNDR effect. However, all the devices shown in figure 6.9 were driven at the same voltage. Dielectric breakdown theory predicts a shift in the "S" shaped *IV* characteristic to higher voltages as the device thickness is increased [8], thus with thicker ZnS:Mn layers CCNDR (and by implication filamentary conduction) is expected to occur at higher applied voltages. The reduction in filamentary conduction with increasing thickness of ZnS:Mn (for constant voltage drive) is consistent with this prediction.

6.4 Time dependent behaviour of DCEL devices

The dielectric breakdown theory of DCEL discussed in section 6.3.1 predicts that, under steady state conditions, CCNDR is expected to occur at a voltage and current density consistent with experimental observations of filamentary conduction. However, since any practical display is operated under pulsed, matrix addressed conditions, there clearly exists a need for a dynamic model which describes the injection and luminescence behaviour of DCEL devices with respect to time. In this section a time dependent model of injection in DCEL devices is discussed. Experimental transients recorded from an epitaxial DCTFEL device are used to test the theory, and comparisons are made with the transient behaviour of powder and sputtered thin film structures.

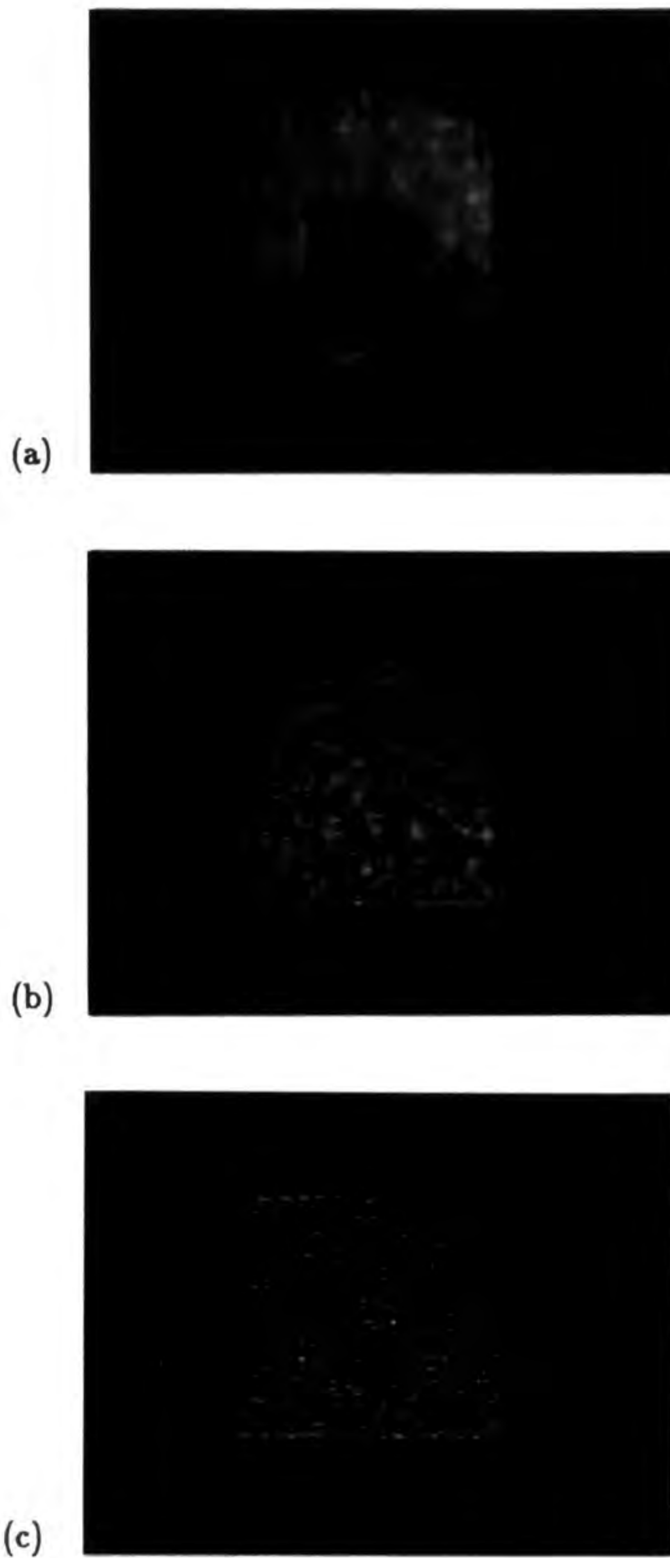

Figure 6.9 The spatial distribution of EL in epitaxial DCTFEL devices with ZnS:Mn layers of thickness (a) 1.27 μm, (b) 0.88 μm, and (c) 0.35 μm.

6.4.1 The time dependent model of DCEL [1]

In modelling the time dependent behaviour of DCEL devices it is necessary to consider the temporal characteristics of the external circuit, and their effect on the device response. Typically the circuit will contain resistive and capacitive elements, and the output voltage V_T at time t after the start of a voltage pulse V_0 is given by:

$$V_T = V_0 \left(1 - e^{-\frac{t}{t_0}}\right) \tag{6.5}$$

where the time constant t_0 is of the order 1 μs. Figure 6.10 shows a typical operational circuit, for which the supply and device voltages can be found using Kirchoff's law:

$$V_T = J(t)RA + V_D \tag{6.6}$$

where R is the load resistance, $J(t)$ is the current density at time t, A is the device cross section, and V_D the voltage across the device. The total current $J(t)$ is made up of electron J_n and hole J_p components, and a displacement (charging) current, which are functions of time t and distance x from the cathode:

$$J(t) = J_n(x,t) + J_p(x,t) + \epsilon\epsilon_0 \frac{\partial E(x,t)}{\partial t} \tag{6.7a}$$

$$= \frac{1}{RA}\left[V(t) - V_D(t)\right] \tag{6.7b}$$

In this time dependent analysis the electron and hole concentrations are considered separately because of the influence of the displacement current:

$$\frac{\partial J_n(x,t)}{\partial x} = |e|\frac{\partial n(x,t)}{\partial t} + \alpha(E(x,t))\ J_n(x,t) \tag{6.8a}$$

$$\frac{\partial J_p(x,t)}{\partial x} = -|e|\frac{\partial p(x,t)}{\partial t} - \alpha(E(x,t))\ J_n(x,t) \tag{6.8b}$$

Equation 6.8 is equivalent to the steady state relationship given by equation 6.3, with an additional time derivative term corresponding to the displacement current. Carrier mobilities are assumed to be governed by drift, and hence are defined by:

$$J_n(x,t) = |e|\ \mu_n n(x,t) E(x,t) \tag{6.9a}$$

$$J_p(x,t) = |e|\ \mu_p p(x,t) E(x,t) \tag{6.9b}$$

The spatial field distribution is given by Poisson's equation:

$$\frac{\partial E(x,t)}{\partial t} = \frac{|e|}{\epsilon\epsilon_0}\left(p(x,t) - n(x,t)\right) \tag{6.10}$$

[1] Model developed by R.E. Jones of this department [23].

Electron injection is limited by tunnelling through a triangular barrier into the conduction band. The time dependent form of equation 6.4 defines this current to be:

$$J_n(0,t+\Delta t) = \frac{[|e|E(0,t+\Delta t)]^2}{(4\pi)^2 h\phi}\left[1+\frac{4\pi^2 m^*(kT)^2\phi}{3h^2|e|[E(0,t+\Delta t)]^2}\right]\exp\left[\frac{-4(2m^*|e|)^{\frac{1}{2}}\phi^{\frac{3}{2}}}{3hE(0,t+\Delta t)}\right] \tag{6.11}$$

Using a finite difference approach and assuming a complete solution at time t, equations 6.5 and 6.7 can be used to calculate the field at time $t+\Delta t$. With this information, equations 6.8, 6.9 and 6.10 can be solved numerically for the boundary conditions given by equation 6.11.

The EL mechanism is one of impact excitation of manganese centres, with light emission on subsequent relaxation. With an excitation cross section σ and a decay constant τ_0 the number of excited manganese centres, and proportionally the EL intensity, is defined by:

$$\frac{\partial \mathrm{Mn}_{ex}(x,t)}{\partial t} = [\mathrm{Mn} - \mathrm{Mn}_{ex}(x,t)\sigma\mu_e\ |F(x,t)|\ n(x,t)] - \frac{\mathrm{Mn}_{ex}}{\tau_0} \tag{6.12}$$

where Mn is the total concentration of manganese centres.

Figure 6.11 shows theoretical voltage and current transients derived for an external voltage supply of 200 V, with a load resistance of 1 kΩ and a device cross sectional area of 1 mm^2 [23]. The voltage across the device is predicted to increase rapidly as the steady state is approached. The current transient shows the initial displacement current which falls as the voltage stabilises, and the injection current which tends towards a steady state value. The solid line in figure 6.11 shows the result of an analytical solution for the displacement current, which was calculated assuming zero carrier injection. Good agreement between the two results for lower values of t indicates that the numerical solution is accurate.

6.4.2 Experimental electrical and luminescent transient behaviour

Electroluminescent rise transients were recorded using an EMI type 9781R photomultiplier tube and a Gould model 1425 digital storage oscilloscope (DSO), with an overall system time constant of approximately 250 ns. Voltage waveforms were measured directly across the device, while current transients were recorded by monitoring the voltage developed across a 10 Ω resistor connected in series with the device. The power supply used for these measurements, shown in figure 6.12, was designed to provide a pulsed voltage source with well defined characteristics. In effect, the circuit simply short circuits the load until the MOSFET is turned off by an external signal, when the device begins to charge through a 2 kΩ load resistance.

Figure 6.13 shows typical luminescence, current and voltage transients [24] recorded from an epitaxial DCTFEL device with an (external) supply of 120 V. The voltage and

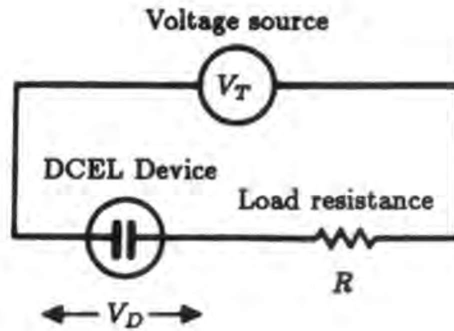

Figure 6.10 Schematic diagram of the external circuit used in the pulsed constant voltage operation of DCEL devices.

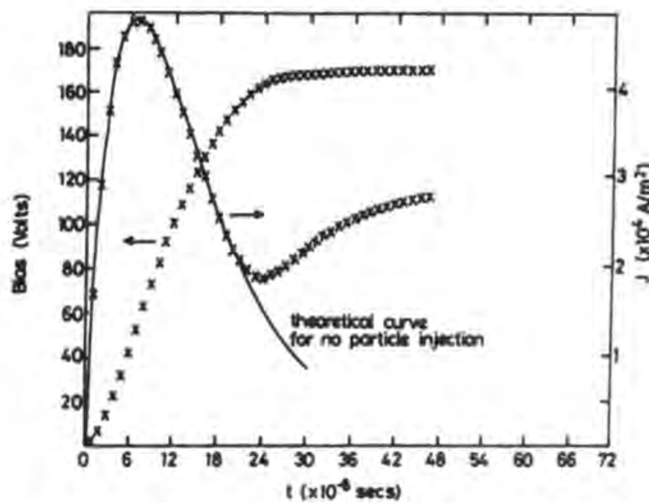

Figure 6.11 Calculated current and voltage transients for a DCEL device driven using 200 V pulses with a load resistance of 1 kΩ (ref. [23]).

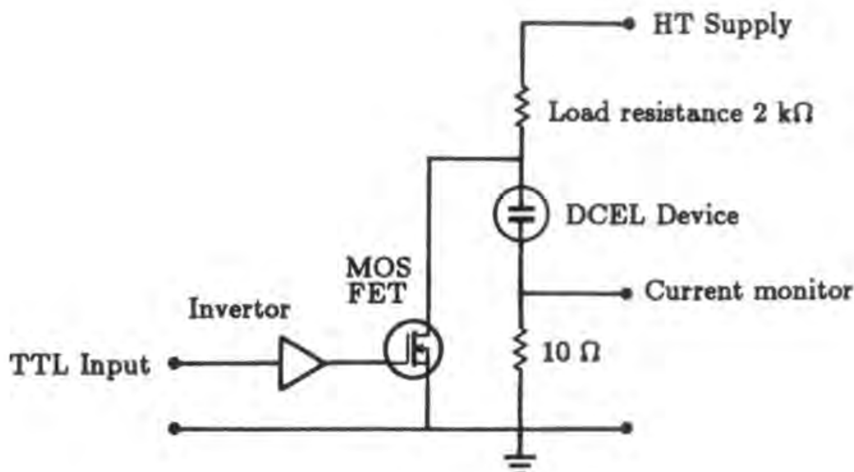

Figure 6.12 Simplified schematic diagram of the high voltage pulse generator used in the operation of DCEL devices.

current transients are of the same form as the theoretical transients discussed in section 6.4.1. The main feature of the luminescence transient is that the onset of EL is delayed by approximately 1 μs from the start of the voltage pulse. The devices used for these measurements had a ZnS:Mn layer ~0.8 μm thick, and would thus be expected to show mixed uniform and filamentary components of current and luminescence (section 6.3.4). All the transients contain spikes at random time intervals, probably corresponding to LDB events which occur as a result of filamentary conduction. Individual LDB events resulted in a momentary increase in the current and luminescence levels, with a corresponding decrease in the voltage across the device. The LDB spikes do not appear to occur simultaneously on the transients simply because the DSO was operated in an interleaved sampling mode. Very similar transients were recorded from both powder and sputtered DCEL devices, and for comparison a set of transients from a powder device are shown in figure 6.14. The most notable feature of these transients is the absence of breakdown spikes, thus demonstrating the effectiveness of the current control layer of the powder structure in minimising LDB. Otherwise, the close similarity in the transient response of powder and epitaxial DCEL devices indicates that the epitaxial DCTFEL structure is a good electrical analogue of more commercially orientated displays.

In order to compare the measured transient response of the epitaxial DCTFEL devices with the predictions of the time dependent model discussed in section 6.4.1, values for the various physical parameters which influenced the injection characteristics of the device were required. Some of these parameters were easily measured, including for example the area and thickness of the device, and the characteristics of the power supply. However, experimental values for other parameters were not available, and the literature values for single crystal material were used (figure 6.15) [23]. Figure 6.15 illustrates the excellent quantitative agreement found between the experimental and theoretical transients, and shows that the time delay between the beginning of the voltage pulse and the onset of EL was accurately predicted by the model.

Unfortunately, the short operational lifetime of the epitaxial DCTFEL devices (section 6.5) precluded a detailed study of their behaviour under a range of operating conditions. However, the time delay before the onset of EL (and by implication current avalanching) was studied in greater detail using powder type DCEL displays. Initially the powder devices were driven with a pulsed voltage source. A representative series of luminescence, current and voltage transients, recorded with 50 μs voltage pulses of 50 V and 100 V, are shown in figures 6.16a and b respectively. With 50 V pulses avalanching occurred at a voltage of 48 V, when the positive displacement (charging) current decayed to a steady dissipative value. In figure 6.16b the drive was 100 V but no light emission was detected when the voltage transient crossed 48 V, and when avalanching occurred near the end of the displacement current transient the voltage across the device was

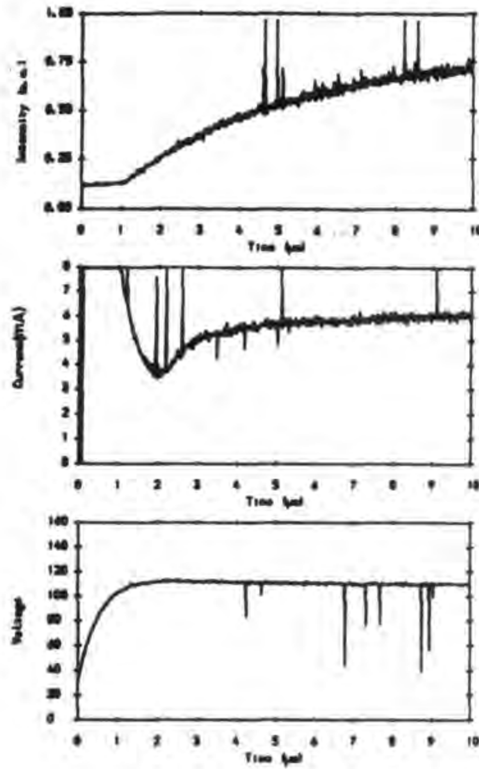

Figure 6.13 Luminescence, current and voltage transients recorded from an epitaxial DCT-FEL device under constant voltage operation with 120 V pulses.

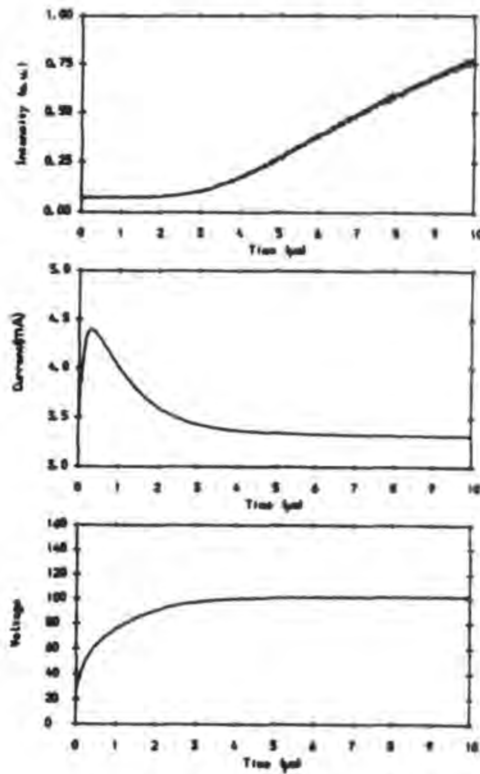

Figure 6.14 Luminescence, current and voltage transients recorded from a powder type DCEL cell under constant voltage operation with 100 V pulses.

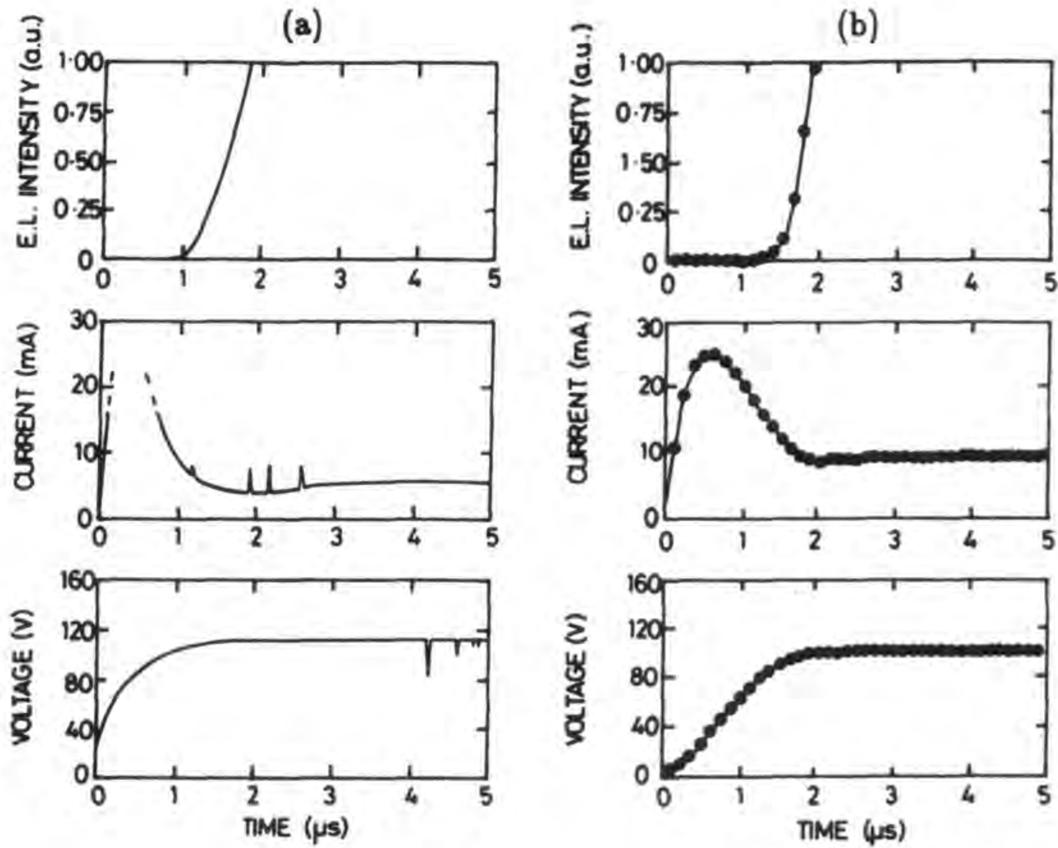

Figure 6.15 Theoretical and experimental luminescence, current and voltage transients: (a) transients recorded from an epitaxial DCTFEL device with thickness = 0.88 μm, load resistance = 2 kΩ, area = 4 mm^2, supply voltage = 120 V, supply rise time = 0.5 μs. (b) calculated transients with barrier height ϕ = 0.55 eV, thickness = 0.88 μm, electron and hole mobilities of $\mu_e = 10^{-2}$ and $\mu_h = 10^{-4}$ $m^2s^{-1}V^{-1}$ respectively, effective mass ratio=0.5, load resistance = 2 kΩ, area = 4 mm^2, external voltage = 120 V, supply time constant = 0.5 μs, time step = 0.125 μs, maximum time = 5 μs, read out time step = 0.125 μs.

88 V. Similar results were obtained for voltage pulses in the range 50–150 V, and in each case avalanching occurred towards the end of the displacement current transient. Numerical integration under the current transient up to the time when luminescence was first detected indicated that the onset of avalanching was associated with a constant level of charge injection ($q = \int i \, dt$), while the voltage transients showed that there was no simple correlation between avalanching and the external electric field measured across the device.

The pulsed voltage drive used in these experiments was chosen to simulate the drive conditions used in commercial applications. However, in order to verify the charging effects described above, more controlled conditions were required and the measurements were repeated using a pulsed current source. Figure 6.17 shows a simplified schematic diagram of the voltage controlled current source, which incorporated a sense resistor in series with the DCEL device, and a feedback arrangement which maintained the voltage across this resistor at the same level as an external control voltage. Figure 6.16c shows luminescence, current and voltage transients respectively from a powder device driven with 300 μs pulses of 0.5, 1.0, 2.0, 4.0 and 8.0 mA (the luminescence transients are displaced vertically for clarity). Clearly, under these drive conditions the charge on the device was determined simply by the current–time product, and this relationship was reflected in the luminescence transients, where the time delay before the onset of avalanching was inversely proportional to the magnitude of the current pulse. The vertical markers in figure 6.16c show the time intervals between the start of the current pulse and the onset of luminescence for each of the five current levels. In each case the current–time product corresponded to a charge of 82.5 nC, and this was found to remain constant over a wider current range of 0.15 to 8.0 mA (the limits being set by the apparatus). The voltage transients in figure 6.16c show that the effect was not simply due to the external field reaching some critical value. Voltages measured across the device at the onset of avalanching were 52, 56 and 63 V for current pulses of 0.15, 0.5 and 8.0 mA respectively. Under steady state conditions the threshold for luminescence was 42 V. Very similar results have since been obtained in a study of sputtered DCTFEL devices [25].

The observations discussed here clearly demonstrate that the initiation of current avalanching in DCEL devices is not related to the "average" electric field determined from the external voltage. Furthermore, the fact that different external voltages were measured for constant levels of charge shows that the device was not behaving as a simple capacitor. The implication is that carrier injection occurred prior to avalanching, and that the injected carriers formed a space charge in the region of the electrode. Avalanching could then occur when the localised field enhancement due to these carriers caused a reduction in the barrier width sufficient for the "positive feedback" mechanism (section 6.3.1) to operate.

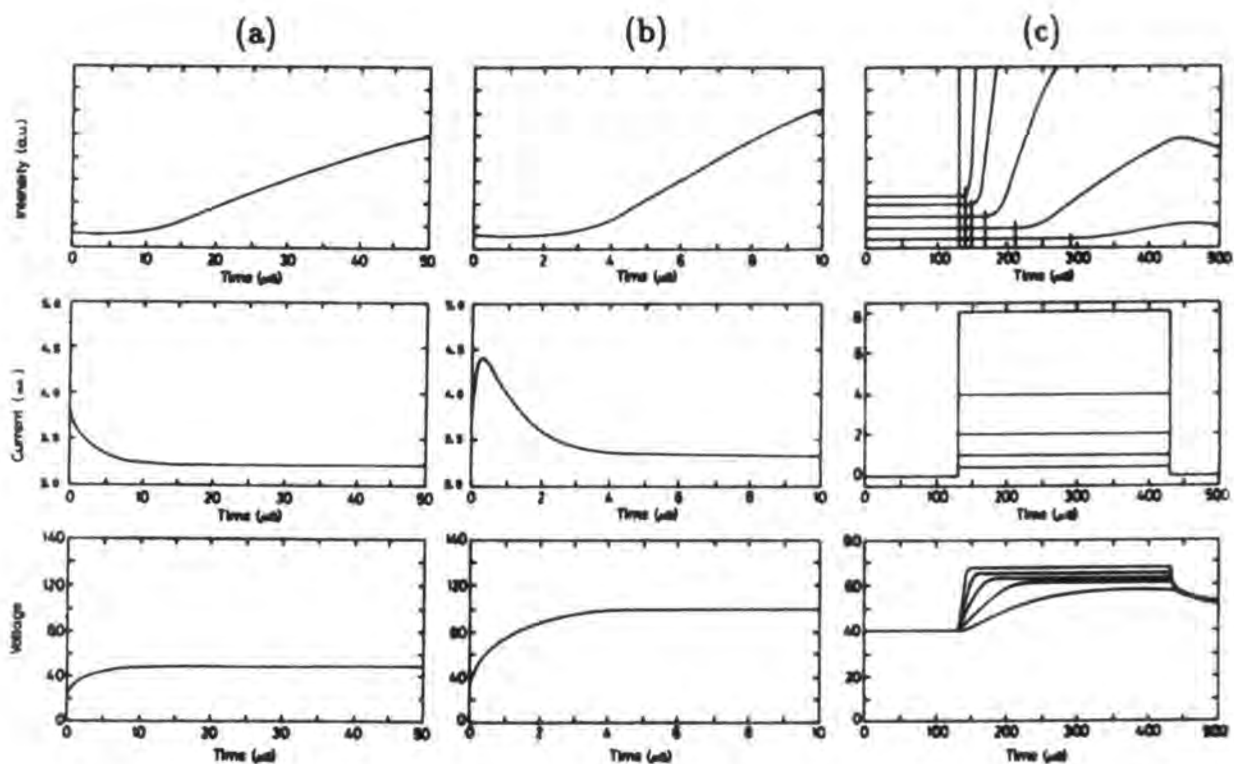

Figure 6.16 Luminescence, current and voltage transients recorded from a powder type DCEL device: (a) and (b) constant voltage operation with 50 V and 100 V pulses respectively, (c) constant current operation with pulses of 0.5, 1.0, 2.0, 4.0, and 8.0 mA (luminescence transients are displaced vertically for clarity and vertical markers indicate the onset of luminescence).

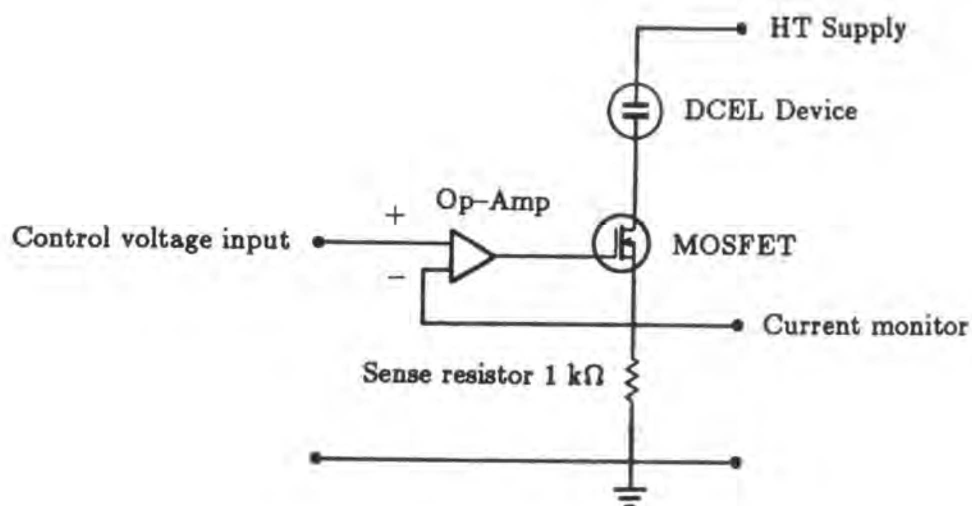

Figure 6.17 Simplified schematic diagram of the voltage controlled current source used in the pulsed constant current operation of DCEL devices.

Although the results shown in figure 6.13 are typical of those recorded from several epitaxial ZnS:Mn DCTFEL structures, slightly different EL transients were observed in devices with thinner ZnS:Mn layers. Figure 6.18 shows sets of transients recorded from an epitaxial DCTFEL device with a ZnS:Mn layer approximately 0.3 μm thick. These are of the same form as those discussed previously apart from an initial instantaneous EL emission (the rise–time is comparable with the system response of 250 ns), which saturates and then remains approximately constant until the onset of the main EL emission. Figure 6.18b shows that this instantaneous emission persists at operating voltages below the threshold for the main EL transient. Unfortunately, the EL intensity from these devices was insufficient to record a time resolved spectrum, and it was not possible to assign the initial emission to a particular electronic transition. It has previously been demonstrated that under operation by short drive pulses, the dominant manganese excitation mechanism involves excitation of alternative centres which subsequently transfer energy to the manganese ions [26]. The initial EL emission observed in figure 6.18 may correspond to this excitation mechanism, which saturates with longer pulse lengths [26]. Alternatively, energetic electrons entering the gold electrode from the ZnS:Mn may excite electrons below the metal Fermi level, as discussed in section 3.1, forming holes which could migrate through the ZnS:Mn and recombine radiatively with electrons in the ZnSe. Given sufficiently pure ZnSe, it would be possible to distinguish between the yellow Mn^{2+} emission associated with the former mechanism and the blue emission of the latter by analysing their EL spectra and decay time constants.

6.5 Device maintenance

The EL emission intensity of commercial DCEL powder displays decreases as a function of time, even under constant voltage operation with a low duty cycle. Three principal failure modes have been identified [22], which can occur singly or in combination, and are associated with:

(1) Further "forming" during operation, resulting in the *IV* characteristic of the device being displaced to higher voltages.
(2) Local load line instability, associated with an increase in the resistance of the current control layer.
(3) The development of parallel current leakage paths.

Notwithstanding these complex and interdependent failure mechanisms, good quality powder panels have a lifetime to half brightness of approximately 3000 hours when operated using 10 μs $\frac{1}{2}$% duty cycle pulses of 120 V [22]. The failure modes of the more recently developed copper–free sputtered DCTFEL devices are less well characterised,

although the major failure mechanism appears to be associated with the occurrence of LDB. Individual LDB events leave behind craters [6], and the electrode area is gradually consumed by the process, with a corresponding decrease in the intensity of EL emission.

The epitaxial DCTFEL structures used in the present study were not intended to compete with existing devices in commercial applications where the operational lifetime is of considerable importance. However, an investigation of the lifetime and degradation mechanisms of the epitaxial devices was undertaken, with the intention of distinguishing breakdown phenomena which are a result of the carrier injection mechanism from those which can be attributed to materials artefacts.

6.5.1 Operational device lifetime

Intensity–time characteristics of the epitaxial devices were recorded during operation with 10 μs pulses of 100 V with a 1% duty cycle, the drive conditions corresponding to those used for the other investigations described in this chapter. The EL intensity was recorded using a photomultiplier tube and a Y–t recorder. Figure 6.19 shows a typical intensity–time plot for a device with a ZnS:Mn layer ~0.8 μm thick, which had a total operational lifetime of approximately 9 hours (the longest measured lifetime was approximately 20 hours). A ZnS:Mn layer thickness of ~0.8 μm appeared to be the optimum in terms of device lifetime. Devices with thicker layers suffered destruction of large areas of the electrodes within a few minutes, while devices with thinner ZnS:Mn layers were more prone to open circuit failures as a result of damage caused by current filaments concentrated at the edge of the electrode (section 6.5.2). The intensity–time plot shown in figure 6.19 illustrates a recurrent rise and fall in the EL intensity, which was typical of many devices. Similar behaviour could be observed using an optical microscope, when it became apparent that the effect was associated with filamentary conduction. Periodically, there was an increase in the EL intensity from an isolated area of the electrode, while the uniform background emission became less intense, resulting in an overall decrease in the EL intensity. The bright region of the electrode subsequently burnt out, and the background emission increased in intensity again. However, the overall intensity was reduced from its previous level as a result of the reduced electrode area. The cycle was repeated continuously, resulting in a gradual reduction of the active device area.

6.5.2 Localised destructive breakdown

The frequency of LDB events in epitaxial ZnS:Mn DCTFEL devices was found to vary considerably with the operating conditions. However, below the turning point in the *IV* characteristic (section 6.3.2) the breakdowns were localised and the ensuing damage remained largely consistent. Figures 6.20a and b show respectively low and high magnification SEM micrographs of the damage caused by typical LDB events. In general

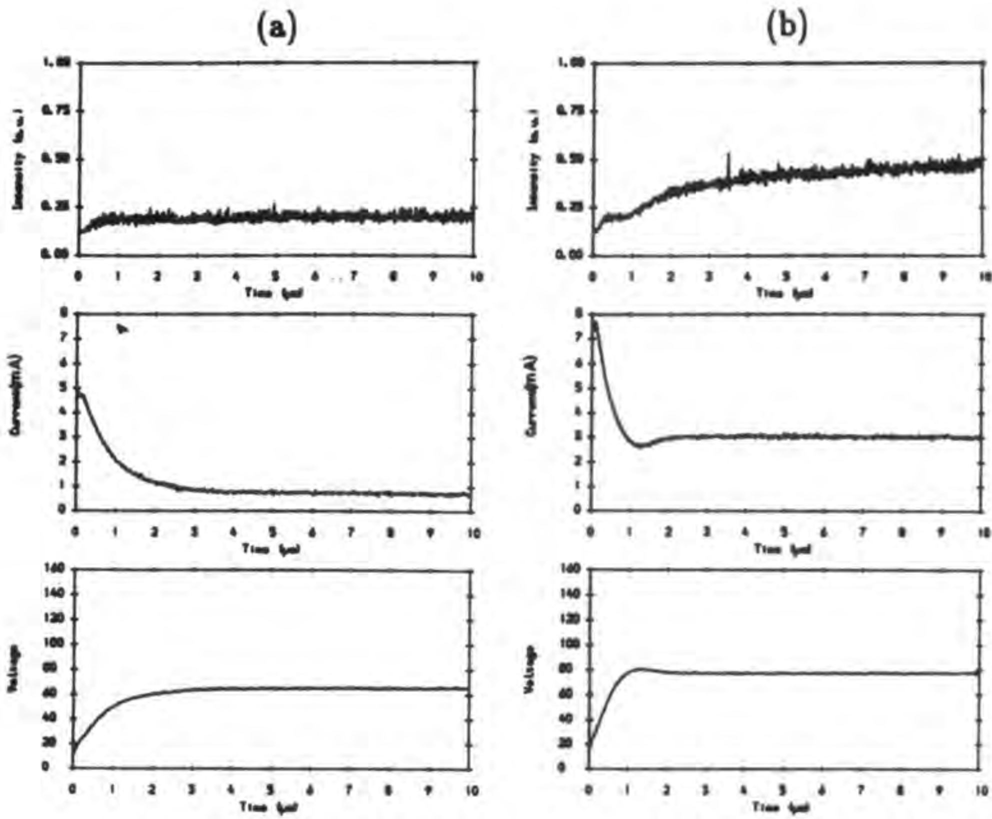

Figure 6.18 Luminescence, current and voltage transients, recorded from an epitaxial DCTFEL device with a ZnS:Mn layer ~0.3 μm thick, showing an initial instantaneous EL emission at voltages (a) below, and (b) above, the voltage threshold for the main EL transient.

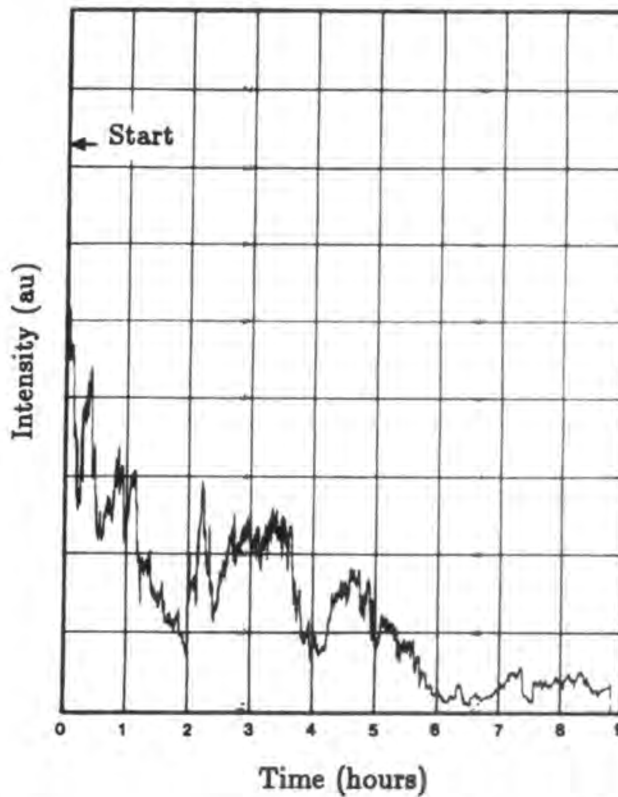

Figure 6.19 Typical intensity–time plot for an epitaxial DCTFEL device, with a ZnS:Mn layer ~0.8 μm thick, during operation with 10 μs pulses of 100 V with a 1% duty cycle.

the heat generated by the high current filament was sufficient to vapourise the top electrode, thereby electrically isolating the affected area before further damage could be caused. It is notable that LDB events appear to occur in clusters, surrounded by an area of damaged material. This may be a result of localised heating which would enhance carrier injection locally, encouraging the formation of additional filaments in the heated region. Figure 6.20c shows a micrograph of similar localised breakdown damage in a sputtered DCTFEL device [27]. In some sputtered devices, similar breakdown events have been associated with previously visible film defects, although these amounted to only a small fraction of the total. In general, it has not been possible to explain the occurrence of LDB in sputtered devices in terms of materials artefacts [6], and this observation lends further support to the dielectric breakdown theory of instability in DCTFEL devices.

During operation of both epitaxial and sputtered devices, most samples exhibited enhanced brightness along the edge of the negatively biased (aluminium or cadmium stannate respectively) electrode. This effect has previously been attributed to an easy current path, where the ZnS:Mn was deposited over the stepped edge of the transparent conductor in sputtered devices [6]. However, since the electrodes of epitaxial structures were deposited after growth of the II–VI layers there is no reason to suspect that either the structure or the composition of these devices should differ at the electrode edges. Enhanced luminescence was accompanied by an increased incidence of LDB along the (–ve) electrode edge, and figures 6.21a and b show the resulting electrode damage at the electrode edges in epitaxial and sputtered devices respectively. An unexpected result was the observation of an area immediately adjacent to the electrode edge with a comparatively low incidence of LDB, particularly in the epitaxial devices (figure 6.21a). Increased LDB at the electrode edge was responsible for the ultimate failure of a large proportion of devices, particularly epitaxial structures with relatively thin ($\leq$0.8 μm) ZnS:Mn layers, where localised damage resulted in electrical isolation of the active electrode area, as shown in figure 6.21c.

6.5.3 Current filament mobility

As the operating voltage of DCTFEL devices was increased there was a corresponding rise in the LDB rate of both sputtered and epitaxial structures, although the nature of the damage remained consistent. However, at voltages greater than the turning point in the *IV* characteristic (section 6.3.2) there was a dramatic change in the breakdown behaviour of the epitaxial devices as the current density increased rapidly over a narrow voltage range, indicative of an increase in the filamentary component of the total current. Under these conditions the current filaments became mobile and migrated over the electrode area causing rapid destruction of the device. Figure 6.22a shows a time exposure of the motion of the bright yellow EL spots over a time period of

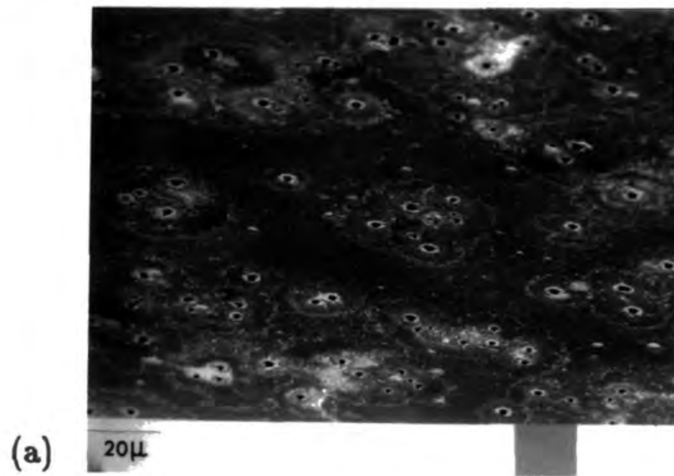

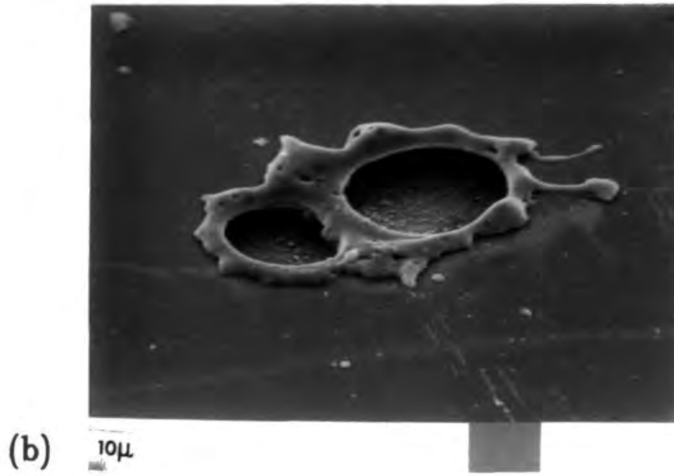

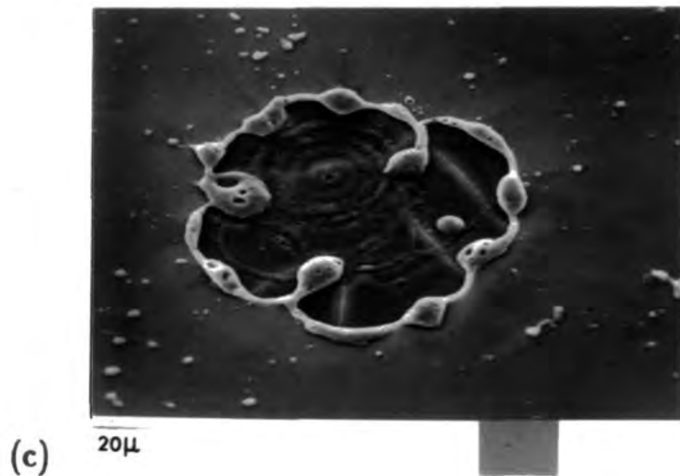

Figure 6.20 SE micrographs showing the damage caused by LDB in: (a) and (b) epitaxial ZnS:Mn/ZnSe, and (c) sputtered ZnS:Mn DCTFEL structures.

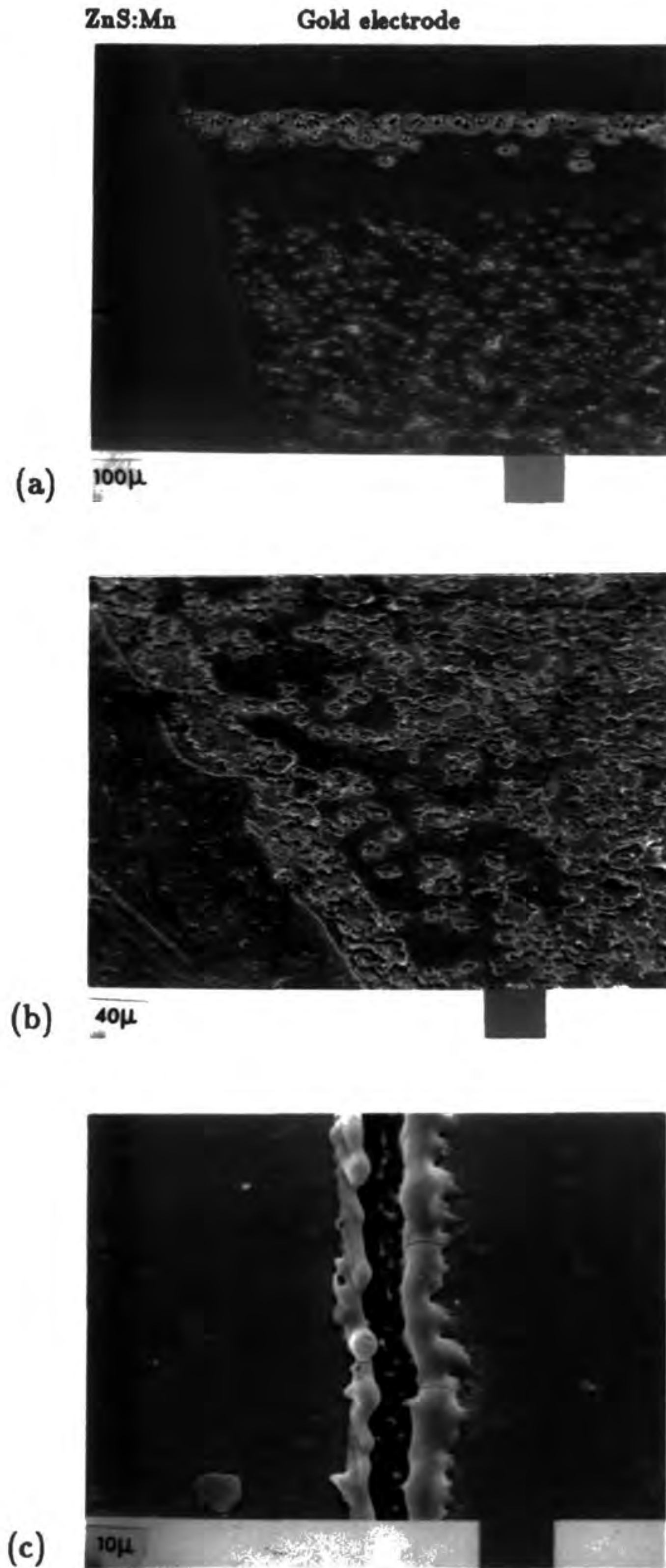

Figure 6.21 SE micrographs showing the higher concentration of LDB along pixel edges in: (a) epitaxial and (b) sputtered DCTFEL structures. (c) electrical isolation of the active electrode area in an epitaxial device as a result of LDB at the pixel edge.

30 seconds. The SEM micrograph shown in figure 6.22b illustrates the damage caused by the current filaments, and the random nature of their motion. At higher magnification (6.22c), it appears that the damage has been caused by filaments jumping from one position to the next. Mobile regions of enhanced brightness have occasionally been observed in sputtered devices, although these did not appear to cause any irreversible changes [6]. Destructive current filament migration was not observed in the sputtered structures, and this was the only major difference in the breakdown behaviour of single crystal and polycrystalline DCTFEL devices. It is possible that the columnar polycrystalline structure of the sputtered devices [27] may be beneficial in restricting the mobility of current filaments by effectively breaking up the current flow through the ZnS:Mn into discrete paths.

6.6 Summary

Discussion in this chapter has centered on the application of an epitaxial ZnS/ZnSe structure to a study of high field EL in ZnS:Mn. By doping ZnS with manganese during MOCVD growth it was possible to fabricate an epitaxial DCTFEL device with a well defined microstructure. The steady state and transient behaviour of this device was shown to be consistent with the predictions of a dielectric breakdown model of instability and luminescence, under both steady state and dynamic conditions. Filamentary conduction and localised destructive breakdown in the absence of geometric artefacts provided further experimental evidence for this model, and indicated that similar phenomena in more commercially orientated devices were a result of the carrier injection mechanism rather than materials defects. The major difference in the breakdown characteristics of the epitaxial and sputtered devices was the occurrence of mobile destructive current filaments in the former, indicating that the columnar microstructure of sputtered devices may be an important factor in preventing destructive breakdown in commercial displays.

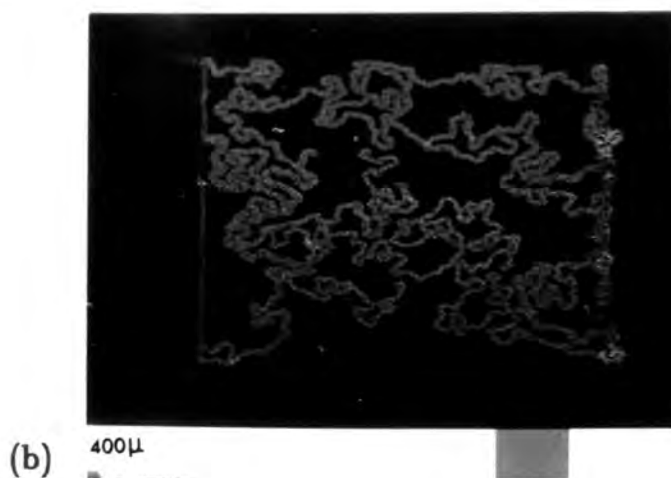

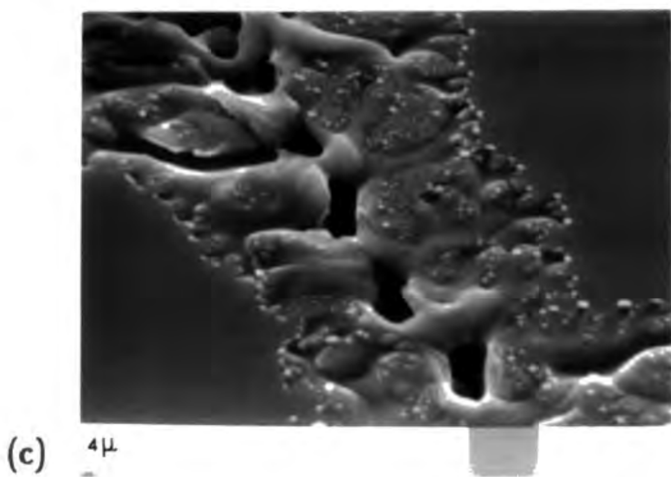

Figure 6.22 Current filament mobility in epitaxial DCTFEL devices: (a) 30 second time exposure showing the motion of Mn yellow EL spots, (b) and (c) SE micrographs showing damage caused by mobile filaments to the active electrode area.

CHAPTER SEVEN

SUMMARY AND CONCLUSIONS

The aim of the research reported in this thesis was to develop an epitaxial device structure which would allow the investigation of EL in single crystal thin film ZnS and ZnSe. The two main types of EL device studied were an MIS diode incorporating a ZnS I–layer, and a high field EL panel based on ZnS:Mn. Both types of device had previously been the subject of extensive experimental investigations, but in each case there was some question as to the influence of materials and geometrical artefacts on the device performance. The use of an epitaxial structure in the present study allowed the characteristics of MIS devices and high field EL panels to be investigated in the absence of such artefacts.

An initial investigation of Au/ZnS/ZnSe MIS structures fabricated using bulk grown ZnSe showed that their EL emission spectra were dominated by impurities, the most likely source of which was contamination from silica and other furnace components during crystal growth and subsequent processing. For this reason the application of the low temperature MOCVD growth technique to the production of II–VI compound devices was investigated. ZnS and ZnSe were grown epitaxially onto (100) orientated GaAs substrates using the reaction between dimethyl zinc and the hydrides H_2S and H_2Se. X–ray diffraction and RHEED confirmed that the structures were epitaxial and of excellent crystallinity, although a cross sectional TEM study revealed the presence of microtwins in the ZnS and ZnSe.

Several different MS and MIS structures were fabricated using the MOCVD grown material. A simple MS device, comprising indium and gold contacts to the as–grown ZnSe, allowed a rapid assessment of the EL properties of the material to be made. However, the device was inefficient, and it was only possible to observe EL around the edges of the gold contact. Although a ZnS I–layer could be deposited over the ZnSe during the same growth run, it was then impossible to make ohmic contacts directly to the ZnSe. Furthermore, *CV* measurements showed that an undesirable electronic barrier was formed at the ZnSe/GaAs interface, and since the substrate was opaque to visible radiation it was not possible to observe the EL emission directly. For these reasons an alternative MIS structure was developed, where chemical removal of the GaAs substrate allowed ohmic contacts to be made directly to the ZnSe, in a configuration which enabled the EL emission to be observed over the entire electrode area. In these devices the ZnS, which was the first layer to be deposited on the GaAs substrate, also acted as a chemi–stop, allowing subsequent chemical removal of the GaAs.

Damage to the ZnS, especially in devices with very thin I-layers, was minimised by using a sequential etching process involving III–V compound chemi-stop layers, which were deposited by MOCVD onto the GaAs substrate prior to growth of the II–VI layers.

A comparative study of MIS devices incorporating epitaxial and polycrystalline ZnS I-layers clearly demonstrated the structural and electrical superiority of the epitaxial ZnS grown by MOCVD. RHEED showed that the epitaxial I-layers were of extremely high structural perfection with a very flat and uniform surface, while the evaporated layers were polycrystalline in nature and showed only slight evidence of a preferred orientation. EBIC studies demonstrated the improvement in electrical uniformity afforded by the use of an epitaxial device structure. The structural integrity and uniformity of the epitaxial layers deposited by MOCVD was manifested in an extremely uniform spatial distribution of EL.

The inherent uniformity of current distribution and EL in the epitaxial II–VI compound device structure was exploited in a study of high field EL panels based on ZnS:Mn. Although several variants of this device are already commercially available, non-uniformity of current distribution and subsequent localised breakdown have been significant obstacles in the development of an all-thin-film sputtered EL panel. By doping ZnS with manganese during MOCVD growth it was possible to adapt the epitaxial ZnS/ZnSe structure to produce an analogue of the commercial DCTFEL device. The spatial distribution of EL in epitaxial DCTFEL devices was non-uniform, consistent with a recently developed dielectric breakdown model of instability, which predicts the occurrence of CCNDR and filamentary conduction. The EL emission included both uniform and filamentary components, and the relative intensity of each was found to depend on the thickness of the ZnS:Mn layer, in accordance with the CCNDR model. Luminescence, current and voltage transients recorded from epitaxial DCTFEL devices were of the same form as transients recorded from both sputtered and powder structures, and were consistent with a time dependent model of DCEL. A delay in the onset of EL after the start of the applied voltage pulse was also in accordance with this model. The delay may represent the time required for the minority carrier population in the region of the cathode to reach a critical concentration, at which point the resulting localised enhancement in the internal electric field becomes sufficient to initiate non-destructive dielectric breakdown.

The major degradation mechanism in both epitaxial and sputtered DCTFEL devices was LDB, which resulted in the gradual destruction of the active device area, and a corresponding decrease in light output. Epitaxial devices with a ZnS:Mn layer $\sim$0.8 μm thick, which exhibited mixed uniform and filamentary conduction, were least susceptible to localised breakdown, and it is possible that this optimum operating condition provided just sufficient local internal field enhancement for efficient carrier injection. Devices with thicker ZnS:Mn layers were prone to loss of large areas of the electrodes

through non–self–healing breakdown, whereas devices with thinner layers, in which conduction was entirely filamentary, were more susceptible to damage by LDB.

The work described here has successfully demonstrated the potential of the epitaxial ZnS/ZnSe structure in a study of both MIS and DCTFEL devices, and extension of the research may be of further benefit, especially in an investigation of DCEL. It should be possible to develop a more accurate single crystal analogue of the commercial devices by replacing the ZnSe layer with a transparent conducting oxide, such as ZnO, which could be deposited by MOCVD. With a more sensitive transient analysis system the effect of carrier injection prior to EL emission could be investigated in greater detail, and relatively minor changes to the time dependent model would allow the effect of carrier injection on the internal field prior to luminescence to be determined. Since CCNDR and filamentary conduction are not directly related to the presence of materials or geometrical artefacts, the single crystal DCTFEL devices may provide a useful model with which to investigate the efficiency of various types of control layer in preventing LDB. Further experimental investigation and theoretical modelling of the epitaxial devices should provide a more complete picture of the injection and breakdown mechanisms associated with DCTFEL.

REFERENCES

Chapter Two

1. M.L. Cohen and T.K. Bergstresser, Phys. Rev. **141** 789 (1966).
2. J.R. Chelikowsky and M.L. Cohen, Phys. Rev. B **14** 556 (1976).
3. P.J. Wright and B. Cockayne, J. Crystal Growth **59** 148 (1982).
4. H. Hartmann, R. Mach and B. Selle, in "Current topics in materials science", Vol. 9, ed. Kaldis, pub. North–Holland (1982).
5. S. Shionoya, J. Luminescence **1,2** 17 (1970).
6. D.G. Thomas and J.J. Hopfield, Phys. Rev. **116** 573 (1959).
7. D.G. Thomas and J.J. Hopfield, Phys. Rev. **128** 2135 (1962).
8. J.S. Prener and F.E. Williams, J. Electrochem. Soc. **103** 342 (1956).
9. E.F. Apple and F.E. Williams, J. Electrochem. Soc. **106** 224 (1959).
10. J.J. Hopfield, D.G. Thomas and M. Gershenzon, Phys. Rev. Letters **10** 162 (1963).
11. P.J. Dean and J.L. Merz, Phys. Rev. **178** 1310 (1969).
12. D.G. Thomas, J.J. Hopfield and W.M. Augustyniak, Phys. Rev. **140** A202 (1965).
13. R.N. Bhargava, R.J. Seymour, B.J. Fitzpatrick and S.P. Herko, Phys. Rev. B **20** 2407 (1979).
14. K. Colbow, Phys. Rev. **141** 742 (1966).
15. L.S. Pedrotti and D.C. Reynolds, Phys. Rev. **120** 1664 (1960).
16. K. Ikeda, K. Uchida and Y. Hamakawa, J. Phys. Chem. Solids **34** 1985 (1973).
17. H. Yamaguchi and A. Yamamoto, Jap. J. Appl. Phys. **16** 77 (1977).
18. K. Era, S. Shionoya and Y. Washizawa, J. Phys. Chem. Solids **29** 1827 (1968).
19. E. Gutsche and O. Goede, J. Luminescence **1,2** 200 (1970).
20. J.J. Davis, J. Crystal Growth **72** 317 (1985).
21. A.E. Thomas, G.J. Russell and J. Woods, J. Phys. C **17** 6219 (1984).
22. K. Urabe and S. Shionoya, J. Phys. Soc. Japan **24** 543 (1968).
23. M. Yamaguchi and T. Shigematsu, Jap. J. Appl. Phys. **17** 335 (1978).
24. J.L. Patel, J.J. Davies and J.E. Nicholls, J. Phys. C **14** 5545 (1981).
25. R.S. Title, in "Physics and chemistry of II–VI compounds", ed. Aven and Prener, pub. North Holland, p. 267 (1967).
26. J. Kirton, in "Handbook on semiconductors", Vol. 4, ed. C. Hilsum, pub. North–Holland, p. 671 (1981).
27. D.S. Mc.Clure, J. Chem. Phys. **39** 2850 (1963).
28. W. Busse, H.E. Gumlich, B. Meissner and D. Theis, J. Luminescence **12,13** 693 (1976).

29. W. Busse, H.E. Gumlich, A. Geoffroy and R. Parrot, Phys. Stat. Sol. b **93** 591 (1979).
30. P.M. Alt, Proc. SID **25** 123 (1984).
31. F.A. Kröger and H.J.G. Mayer, Physica **20** 1149 (1954).
32. E.W. Williams and R. Hall, in "Luminescence and the LED", pub. Pergamon, p. 25 (1978).
33. P.T. Landsberg and M.J. Adams, J. Luminescence **7** 3 (1973).
34. J.I. Pankove, in "Topics in applied physics", Vol. 17, "Electroluminescence", pub. Springer Verlag p. 6 (1977).
35. Y.S. Park and B.K. Shin, *ibid.* p. 133.
36. M. Aven and H.H. Woodbury, Appl. Phys. Lett. **1** 53 (1962).
37. M. Aven and R.E. Halsted, Phys. Rev. **137** A228 (1964).
38. G. Jones and J. Woods, J. Phys. D **9** 799 (1976).
39. G. Neumark, Phys. Rev. B **26** 2250 (1982).
40. J. Bowley, P. Blanconnier, A. Herman, P.G.P. Henon and J.P. Noblanc, J. Appl. Phys. **46** 3549 (1975).
41. A.E. Thomas, J. Woods and Z.V. Hauptman, J. Phys. D **16** 1123 (1983).
42. A.E. Thomas, G.J. Russell and J. Woods, J. Phys. C **17** 6219 (1984).
43. G. Mandel, Phys. Rev. **134** A1073 (1964).
44. P.J. Dean, H. Venghaus, J.C. Pfister, B. Schaub and J. Marine, J. Luminescence **16** 363 (1978).
45. J.L. Merz, K. Nassau and J.W. Shiever, Phys. Rev. B **8** 1444 (1973).
46. G.F. Neumark and S.P. Herko, J. Crystal Growth **59** 189 (1982).
47. Y.S. Park, P.M. Hemenger and C.M. Chung, Appl. Phys. Lett. **18** 45 (1971).
48. B.J. Fitzpatrick, C.J. Werkhoven, T.F. Mc.Gee, P.M. Harnack, S.P. Herko, R.N. Bhargava and P.J. Dean, IEEE Trans. **ED28** 440 (1981).
49. W. Stutius, Appl. Phys. Lett. **40** 246 (1982).
50. Z.L. Wu, J.L. Merz, C.J. Werkhoven, B.J. Fitzpatrick and R.N. Bhargava, Appl. Phys. Lett. **40** 345 (1982).
51. R.N. Bhargava, J. Crystal Growth **59** 15 (1982).
52. K. Kosai, B.J. Fitzpatrick, H.G. Grimmeiss, R.N. Bhargava and G.F. Neumark, Appl. Phys. Lett. **35** 194 (1979).
53. R.J. Robinson and Z.K. Kun, Appl. Phys. Lett. **27** 74 (1975).
54. J. Nishizawa, K.Itoh, Y. Okuno and F. Sakuri, J. Appl. Phys. **57** 2210 (1985).
55. E.H. Rhoderic, in "Metal-semiconductor contacts", pub. Oxford University Press (1980).
56. N.F. Mott, Proc. Cambridge Phil. Soc. **34** 568 (1938).
57. W. Schottky and E. Spenke, Wiss. Verott Siemens–Werken **118** 225 (1939).
58. D.L. Scharfetter, Sol. St. Electon. **8** 299 (1965).

59. R. Mach, H. Treptow and W. Ludwig, Phys. Stat. Sol. a **25** 567 (1974).
60. R. Mach, J. Bochkov, B. Selle and A.N. Georgobiani, Phys. Stat. Sol. a **53** 263 (1979).
61. R.C. Jaklevic, D.K. Donald, J. Lambe and W.C. Vassell, Appl. Phys. Lett. **2** 7 (1963).
62. H.C. Card and E.H. Rhoderick, Sol. St. Electron. **16** 365 (1973).
63. A.G. Fischer, in "Luminescence of inorganic solids", pub. Academic Press p. 573 (1966).
64. J. Woods, Displays **2** 251 (1981).
65. A.W. Livingstone, K. Turvey and J.W. Allen, Sol. St. Electron. **16** 351 (1973).
66. H. Watanabe, T. Chikamura and M. Wada, Jap. J. Appl. Phys. **13** 357 (1974).
67. A.G. Fischer, Phys. Lett. **12** 313 (1964).
68. A.A. Bergh and P.J. Dean, in "Light-emitting diodes", pub. Clarendon Press (1976).
69. H. Ohnishi and Y. Hamakawa, Jap. J. Appl. Phys. **17** 1225 (1978).
70. H. Fujiyasu and K. Mochizuki, J. Appl. Phys. **57** 2960 (1985).
71. N.T. Gordon, M.D. Ryall and J.W. Allen, Appl. Phys. Lett. **35** 691 (1979).
72. C. Lawther and K.V. Anand, Phys. Stat. Sol. a **44** 313 (1977).
73. N.A. Vlasenko and A.M. Yaremko, Soviet Phys. Optics and Spectroscopy **18** 467 (1965).
74. A. Vecht, J. Crystal Growth **59** 81 (1982).
75. G. Destriau, J. Chim. Phys. **33** 587 (1936).
76. T. Inoguchi, M. Takeda, Y. Kakihara, Y. Nakata and M. Yoshida, SID Digest **84** (1974).
77. A. Vecht, N.J. Werring, R. Ellis and P.J.F. Smith, J. Phys. D **2** 953 (1969).
78. J. Kirton, in "Handbook on semiconductors", Vol. 4, ed. C. Hilsum, pub. North–Holland, p. 685 (1981).
79. A.F. Cattell, B. Cockayne, K. Dexter, J. Kirton and P.J. Wright, IEEE Trans. **ED30** 471 (1983).
80. J.M. Blackmore, A.F. Cattell, K.F. Dexter, J.Kirton and P. Lloyd, J. Appl. Phys. **61** 714 (1987).

Chapter Three

1. A. G. Fischer and H. I. Moss, J. Appl. Phys. **34** 2112 (1963).
2. R. C. Jaklevik, D. K. Donald, J. Lambe and W. C. Vassell, Appl. Phys. Lett. **2** 7 (1963).
3. M. Yamaguchi and A. Yamamoto, Jap. J. Appl. Phys. **16** 77 (1977).
4. C. Lawther and J. Woods, Phys. Stat. Sol. a **44** 693 (1977).

5. C. Lawther and J. Woods, Phys. Stat. Sol. a **50** 491 (1978).
6. M.T. Fowler, M. C. Petty, G. G. Roberts, P. J. Wright and B. Cockayne, J. Mol. Electronics **1** 93 (1985).
7. A. W. Livingstone, K. Turvey and J. W. Allen, Sol. State. Electron. **16** 351 (1963).
8. H. Watanabe, T. Chikamura and M. Wada, Jap. J. Appl. Phys. **13** 357 (1974).
9. C. Lawther, S. Fujita and T. Takagi, Jap. J. Appl. Phys. **19** 939 (1980).
10. A. G. Fischer, Phys. Rev. Lett. **12** 313 (1964).
11. C. Lawther and J. Woods, J. Luminescence **18–19** 724 (1979).
12. R. E. Jones, Ph.D. Thesis. University of Durham (1986).
13. C. Lawther and K.V. Anand, phys. stat. sol. (a) **44** 313 (1977).
14. B. Ray, in: "II–VI compounds", pub. Pergamon (1969).
15. H. Katayama, S. Oda and H. Kukimoto, Appl. Phys. Lett. **27** 697 (1975).
16. A. E. Thomas, J. Woods and Z. V. Hauptman, J. Phys. D **16** 1123 (1983).
17. M. M. Labes, P. Love and L. F. Nichols, Chemical Reviews **79** 1 (1971).
18. G. J. Russell and J. Woods, J. Cryst. Growth **46** 323 (1979).
19. M. Aven and H. Woodbury, Appl. Phys. Lett. **1** 53 (1962).
20. S. S. Devlin, in: "Physics and chemistry of II–VI compounds", Eds. M. Aven and J. S. Prener, pub. North–Holland p. 604 (1966).
21. A. E. Thomas, G. J. Russell and J. Woods, J. Cryst. Growth **63** 265 (1983).
22. A. E. Thomas, G. J. Russell and J. Woods, J. Phys. C **17** 6219 (1984).
23. G. Jones and J. Woods, J. Luminescence **9** 389 (1974).
24. A. P. C. Jones, A. W. Brinkman and J. Woods, J. Phys. E **19** 1066 (1986).
25. P. J. Dean and J. L. Merz, Phys. Rev. **178** 1310 (1969).
26. R. N. Bhargava, R. J. Seymour, B. J. Fitzpatrick and S. P. Herko, Phys. Rev. B **20** 2407 (1979).
27. R. H. Fowler, Phys. Rev. **38** 45 (1931).
28. C. R. Crowell, W. G. Spitzer, L. E. Howarth and E. E. LaBate, Phys. Rev. **127** 2006 (1962).
29. H. G. Grimmeis, Proc. Conf. MS contacts, Inst. Phys. **22** 3 (1974).
30. M. E. Özsan and J. Woods, Solid State Electron. **18** 519 (1975).
31. A. M. Cowley, J. Appl. Phys. **37** 3024 (1966).
32. W. Schottky and E. Spenke, Wiss. Veoff. Siemens–Werken **18** 225 (1939).
33. H. A. Bethe, MIT Rad. Lab. Report **43** 12 (1942).
34. E.H. Rhoderick, J. Phys. D **5** 1920 (1972).
35. B. J. Fitzpatrick, R. N. Bhargava, S. P. Herko and P. M. Harnack, J. Electrochem. Soc. **126** 341 (1979).
36. S. Fujita, H. Mimoto and T. Noguchi, J. Appl. Phys. **50** 1079 (1979).

37. B. Cockayne, P.J. Wright, G.W. Blackmore, J.O. Williams and T.L. Ng, J. Mat. Sci. 19 3726 (1984).
38. A. M. Goodman, J. Appl. Phys. 34 329 (1963).
39. S. J. Fonash, J. Appl. Phys. 54 1966 (1983).

Chapter Four

1. J.R. Cutter, G.J. Russell and J. Woods, J. Cryst. Growth 32 179 (1976).
2. G.J. Russell and J. Woods, J. Cryst. Growth 47 647 (1979).
3. B. Cockayne and P.J. Wright, J. Cryst. Growth 68 223 (1984).
4. H.M. Manasevit and W.I. Simpson, J. Electrochem. Soc. 118 644 (1971).
5. W. Stutius, Appl. Phys. Lett. 33 656 (1978).
6. P. Blanconnier, M. Cerdet, P. Henoc and A.M. Jean Louis, Thin Solid Films 55 375 (1978).
7. S.J. Bass and P.E. Oliver, Inst. Phys. Conf. Ser. 33b 1 (1977).
8. W. Stutius, J. Cryst. Growth 59 1 (1982).
9. P.J. Wright and B. Cockayne, J. Cryst. Growth 59 148 (1982).
10. P.J. Wright, R.J.M. Griffiths and B. Cockayne, J. Cryst. Growth 66 26 (1984).
11. B. Cockayne, P.J. Wright, G.W. Blackmore, J.O. Williams and T.L. Ng, J. Mat. Sci. 19 3726 (1984).
12. J.O. Williams, T.L. Ng, A.C. Wright, B. Cockayne and P.J. Wright, J. Cryst. Growth 68 237 (1984).
13. W. Stutius, J. Appl. Phys. 53 284 (1982).
14. W. Stutius, Appl. Phys. Lett. 40 246 (1982).
15. J.B. Mullin, S.J.C. Irvine, J. Geiss and A. Royle, J. Cryst. Growth 72 1 (1985).
16. S. Fujita, T. Yoda, Y. Matsuda and A. Sasaki, J. Cryst. Growth 71 169 (1985).
17. T. Yao, M. Ogura, S. Matsuoka and T. Morishita, Appl. Phys. Lett. 43 499 (1983).
18. S. Fujita, Y. Matsuda and A. Sasaki, J. Cryst. Growth 68 231 (1984).
19. S. Fujita, Y. Matsuda and A. Sasaki, Jap. J. Appl. Phys. 23 L360 (1984).
20. D.R. Wight, P.J. Wright and B. Cockayne, Electron. Lett. 18 593 (1982).
21. A.F. Cattell, B. Cockayne, K. Dexter, J. Kirton and P.J. Wright, IEEE Trans. ED 30 471 (1983).
22. S. Fujita, T. Yoda and A. Sasaki, J. Cryst. Growth 72 27 (1985).
23. P.J. Dean, phys. stat. sol. (a) 81 625 (1984).
24. W. Stutius, J. Electron. Mater. 10 95 (1981).
25. P.D. Brown, A.P.C. Jones, G.J. Russell, J. Woods, B. Cockayne and P.J. Wright, Proc. MSM 5 Conf. Oxford 1987.
26. W. Stutius and F.A. Ponce, J. Appl. Phys. 58 1548 (1985).

27. F.A. Ponce, W. Stutius and J.G. Werthen, Thin Solid Films **104** 133 (1983).
28. J.O. Williams, E.S. Crawford, J.L. Jenkins, T.L. Ng, A.M. Patterson, M.D. Scott, B. Cockayne and P.J. Wright, J. Mat. Sci. **3** 189 (1984).
29. J.O. Williams and A.C. Wright, Phil. Mag. A **55** 99 (1987).
30. B. Greenberg, W.K. Zwicker and I. Cadoff, Thin Solid Films **141** 89 (1986).
31. N.G. Chew and A.G. Cullis, Inst. Phys. Conf. Ser. **78** 143 (1985).
32. P.D. Brown, private communication: F.A. Ponce.
33. P.B. Hirsch, Phil. Mag. B **52** 759 (1985).
34. S.D. Hersee, E. Barbier and R. Blondeau, J. Cryst. Growth **77** 310 (1986).
35. D.P. Kennedy, P.C. Murley and W. Klienfelder, IBM J. Res. Develop. 399 (1968).
36. W.C. Johnson and P. Panousis, IEEE Trans. ED **18** 1979 (1971).

Chapter Five

1. A.P.C. Jones, A.W. Brinkman, G.J. Russell, J.Woods, P.J. Wright and B. Cockayne, Semicond. Sci. Technol. **1** 41 (1986).
2. G.A. Antypas and J. Edgecumbe, Appl. Phys. Lett **26** 371 (1975).
3. H. Watanabe, T. Chickamura and M. Wada, Japan. J. Appl. Phys. **13** 357 (1974).
4. A.P.C. Jones, P.J. Wright, A.W. Brinkman, G.J. Russell, J. Woods and B. Cockayne, IEEE Trans ED **34** 937 (1987).
5. H. Hemmat and M. Weinstien, J. Electrochem. Soc. **114** 851 (1967).
6. P.J. Dean, phys. stat. sol. (a) **81** 625 (1984).
7. D.W. Langer, R.N. Euwema, K. Era and T. Koda, Phys. Rev. B **2** 4005 (1970).
8. S.D. Brotherton, T.G. Read, D.R. Lamb and A.F.W. Willoughby, Solid State Electron. **16** 1367 (1973).
9. B. Cockayne, P.J. Wright, G.W. Blackmore, J.O. Williams and T.L. Ng, J. Mat. Sci. **19** 3726 (1984).
10. I. Suemune, K. Ohmi, T. Kanda, K. Yukutake, Y. Kan and M. Yamanishi, Japan. J. Appl. Phys. **25** L827 (1986).
11. S.J. Fonash, J. Appl. Phys. **54** 1966 (1983).
12. W. Czaja and J.R. Patel, J. Appl. Phys. **36** 1476 (1965).
13. T.E. Seidel, S.E. Haszko and D.M. Maher, J. Appl. Phys. **48** 5038 (1977).
14. G.J. Russell, M.J. Robertson, B. Vincent and J. Woods, J. Mat. Sci. **15** 939 (1980).
15. G.J. Russell, M.J. Robertson and J. Woods, phys. stat. sol. (a) **57** 253 (1980).
16. X. Fan, J. Zhang, Z. Zhang, S. Wang, A. Lu, W. Li, J. Jiang and Y. Sun, J. Luminescence **31/32** 957 (1984).
17. Y.S. Park and C.R. Geesner, Appl. Phys. Lett. **21** 567 (1972).

Chapter Six

1. S. Shionoya in: "Luminescence of Inorganic Solids", Ed. P. Goldberg, Chap. 4, Academic Press (1966).
2. W.G. Freer, Proc. Second European Solid State Devices Conf., Institute of Physics, p.224 (1972).
3. J. Kirton in: "Handbook on Semiconductors", Vol. 4, Ed. C. Hilsum, pub. North Holland, p. 683 (1981).
4. P. Goldberg and J.W. Nickerson, J. Appl. Phys. **34** 1601 (1963).
5. T. Takagi, I. Yamada, A. Sasaki and T. Ishibashi, IEEE Trans. ED **20** 1110 (1973).
6. J.M. Blackmore, A.F. Cattell, K.F. Dexter, J. Kirton and P. Lloyd, J. Appl. Phys. **61** 714 (1987).
7. A.F. Cattell, J.C. Inkson and J. Kirton, J. Appl. Phys. **61** 722 (1987).
8. R.E. Jones, Ph.D. Thesis, Chap. 7, University of Durham (1986).
9. J. Kirton, Proc. European Display Research Conf., p. 144 (1981).
10. A.F. Cattell, B. Cockayne, K. Dexter, J. Kirton and P.J. Wright, IEEE Trans. ED **30** 471 (1983).
11. C.J. Alder, A.F. Fray, C. Hilsum and P. Lloyd, Displays **1** 191 (1980).
12. K. Okamoto, S. Tanaka, H. Kobayashi and H. Sasakura, IEEE Trans. ED **25** 1170 (1978).
13. T. Doi, H. Ohnshi, K. Leyasu and Y. Hamakaura, J. Appl. Phys. **51** 4555 (1980).
14. T. Mishima, W. Quan–kun, and K. Takashi, J. Appl. Phys. **52** 5797 (1981).
15. A.P.C. Jones, A.W. Brinkman, G.J. Russell, J. Woods, P.J. Wright and B. Cockayne, Semicond. Sci. Technol. (in press).
16. P.J. Wright, B. Cockayne, A.F. Cattell, P.J. Dean and A.D. Pitt, J. Cryst. Growth **59** 155 (1982).
17. N. Mino, M. Kobayashi, M. Konagai and T. Takahashi Jap. J. Appl. Phys. **24** L383 (1985).
18. B.K. Ridley, Proc. Phys. Soc. **82** 954 (1963).
19. M.A. Lampert and P. Mark in: "Current Injection in Solids", Academic Press (1970).
20. R.E. Jones, private communication: A.F. Cattell.
21. D. Mukhopadhyay and D.P. Bhattacharya, J. Phys. Chem. Solids **45** 393 (1984).
22. C.J. Alder, A.F. Cattell, K.F. Dexter, M.Dixon, J. Kirton and M.S. Skolnick, IEEE Trans. ED **28** 680 (1981).
23. R.E. Jones, Ph.D. Thesis, Chap. 8, University of Durham (1986).
24. A.P.C. Jones, R.E. Jones, A.W. Brinkman, D.Y. Watts, J. Woods and D.J. Robins, Proc. Third Int. Conf. on II–VI Compounds, Monterey, California (J. Cryst. Growth, in press).

25. D.Y. Watts, private communication.

26. E. Chimezak and J.W. Allen, J. Phys. D. 18 951 (1985).

27. A.P.C. Jones, D.Y. Watts, A.W. Brinkman, G.J. Russel and J. Woods, Proc. Third Int. Conf. on II–VI Compounds, Monterey, California (J. Cryst. Growth, in press).